University of Alberta

Synthesis of Tungsten Trioxide Thin Films for Gas Detection

by

Andrew John Murray

A thesis submitted to the Faculty of Graduate Studies and Research
in partial fulfillment of the requirements for the degree of

Master of Science
in
Micro-Electro-Mechanical Systems (MEMS) and Nanosystems

Electrical and Computer Engineering

Spring 2010
Edmonton, Alberta

Examining Committee

Dr. Stephane Evoy, Electrical and Computer Engineering

Dr. Michael Brett, Electrical and Computer Engineering

Dr. Ken Cadien, Chemical and Materials Engineering

Abstract

The ability to detect and quantify presence and concentration of unknown gasses is sought for applications ranging from environmental monitoring to medical analysis. Metal oxide based chemical sensing technology currently exists but the ability to provide a compositional gas breakdown reliably within a short time frame is not readily available. A very small sensor that can differentially identify the type and concentration of a gas is required. Novel methods of creating low cost and easily tuned one and two-dimensional gas sensing elements are explored. Tungsten trioxide has been thoroughly documented as an electrochromic coating, but highly sensitive WO_3 elements with beam and nanowire structures have yet to be explored. Research of WO_3 as a gas sensor encompasses three major components: A suitable sensing chamber with accurate analyte gas flow control and temperature control, a reliable method for WO_3 deposition, and a high yield fabrication process. This thesis explores all three of these technologies. Chapter two starts with a summary of existing tungsten trioxide fabrication methods. An overview of WO_3 processing follows. A comprehensive setup was designed and created to test the gas sensing response of a series of metal oxide based resistive elements through conductimetric analysis. Chapter three provides an in depth account of gas sensor test chamber design and testing. Critical test chamber aspects such as temperature control, precise gas flow control, highly efficient analyte gas switching and ease of use are presented. Chapter four outlines WO_3 electrodeposition and the fabrication of beam structures for testing, while chapter five explores the templated electrodeposition of WO_3 segments intercalated between gold nanowire segments. Finally, chapter six provides a summary of the research presented in this thesis as well as future directions and options available for further exploration of WO_3 gas sensing elements.

Acknowledgements

Firstly, I thank my supervisor, Dr. Stephane Evoy, who gave our project vision and encouraged high quality work in an exciting and stimulating field. You helped guide and focus my energy throughout the years and I feel privileged to have worked with you. A special thanks to my committee members, Dr. Michael Brett and Dr. Ken Cadien, for the time and effort you put into reviewing my thesis, for sitting on my committee, and for the many words of encouragement you provided. Also, Eric Finley, the support, insight, and assistance you provided during the design intensive portions of my project were immeasurably helpful.

I dedicate this thesis to my parents, Ilse and Andrew Murray who supported me though every step of this adventure. Your love, kind words, and gentle encouragement comforted me during the challenges and helped me realize and enjoy the successes. My brother and sister, Daan and Lize, who were always there to suffer alongside, offer words of questionable wisdom, and procrastinate over the phone.

Finally, I'd like to thank the many friends and lab mates that helped shape me as a person and fill these years with absolutely incredible memories. Colin, Erik, Lee, Luc, Nem, Nick, Chris Holt, Steve, Aruna, Nathan, Mohsen, Ali, Babak, Branden, Saunders and all the others: You shared the highest highs throughout all the years. Mandy, Joc, Kendra, Cata: You provided immeasurable and ceaseless love, laughs, and support. Also, Kurt Morrison, thank you for the many years of work hard, play hard influence you had on my life. You were always there with a cold beverage to help me put life in perspective.

Sincerely,

Andrew J Murray

November, 2009

Table of Contents

List of Figures

1 Introduction

Sensitivity, Selectivity, and Stability - The ”3S” criteria are the driving force behind gas sensor research. A compact, effective, sensitive and energy efficient means for obtaining compositional breakdown of gases has been sought for many years. Comprehensive chemical sensors can be directly applied to environmental monitoring for control and workplace health and safety. Semiconducting gas sensors can also be employed in work environments as portable gas detections units, protecting individuals from exposure to hazardous chemicals such as hydrogen sulphide. Low concentration emissions monitoring of industrial plants, agricultural lots and motor vehicles could be made possible by the continuous functionality and stability of semiconducting sensors in severe working conditions. Uncomplicated fabrication and testing methods for low cost effective gas sensors are being explored.

1.1 Motivation for Chemical Sensing

Conductimetric metal oxide gas sensor technology seeks to accurately analyze a unknown mixture of gases and instantly provide an accurate compositional breakdown. Such sensors can be used for efficient environmental monitoring [4], medical diagnostics [5] as well as hazardous chemical [6] and explosives monitoring [7].

A recent shift in environmental policy and pollution control relies on atmospheric sensing to determine pollutant levels but there there is a lack in cost effective methods to monitor industrial and commercial pollution. Gas sensors that provide an accurate chemical breakdown and can be employed in high temperature environments, such as vehicle exhaust pipes and industrial smoke stacks, would allow effective monitoring and aide in establishing standards to which polluting industries can be held accountable.

Figure 1.1: GW Gas Alert Micro 5 portable gas detection system. Reprinted with permission [1].

Commercially available gas sensors offer a wide variety of detection capabilities. Portable sensors are often relied upon in hazardous workplace environments such as chemical processing, mining and oilfield exploration. Units such as the Gas Alert Micro 5 seen in Figure1.1, by Honeywell International, have been developed to detect a wide variety of chemicals including H_2S, CO, O_2, SO_2, PH_3, NH_3, NO_2, HCN, Cl_2, ClO_2, O_3, and combustibles. This particular model can monitor up to 5 different chemicals

simultaneously and provides audible safety alarm setting for maximum recommended time weighted average (TWA) and short term exposure limit (STEL) levels. Metal oxide sensors such as the Gas Alert Micro 5 have been effectively applied to large industrial scenarios where power consumption and sensor size is not a problem. These sensors are however not sufficiently flexible to accommodate a market is for small, cost effective, and long lasting gas detection units. Additional sensors must be produced that will deliver a highly accurate chemical breakdown of all the gases in its immediate location. These sensors would suit applications ranging from oil exploration and mining to vehicle emissions monitoring and medical monitoring. Properly integrated semiconductor gas sensors offer the ability to concentrate a variety of sensing materials on a very low surface area microchip. Research into applicable sensing materials and sensor configurations is currently underway. The following chapters present an analysis of tungsten trioxide fabrication techniques for the realization of one and two dimensional sensing structures.

1.2 Semiconductor Based Gas Sensors

More rigorous industrial standards used in conventional integrated circuite (IC) processing have resulted in efficient and cost effective large scale production techniques such as optical lithography, physical vapor deposition, and chemical etching. Creating a highly integrated chemical sensor on a single silicon die may not have been feasible some years ago but strict processing standards and a global focus on nanoscale processing has created a large and varied fabrication infrastructure. Nanofabrication facilities are now capable of supporting research and development into the deposition and patterning of many different sensing materials with relative ease. A reduction in fabrication dependant critical dimension limitations has opened up the possibility to create a sensing chip containing multiple complementary sensors.

Variables Reviewed

Eranna *et al.* [2] offers a comprehensive review of metal oxides used in gas detection. They provide a clear indication of which metal oxide sensors can be employed to sense a number of gases. It is also apparent that the combination of multiple sensing materials

Sensing behavior of different metal oxides to various gaseous species

	Metal oxides																			
Gas	Al	Bi	Cd	Ce	Cr	Co	Cu	Ga	In	Fe	Mn	Mo	Ni	Nb	Ta	Sn	Ti	W	Zn	Zr	Mx
Acetone ($CH_3{\cdot}CO{\cdot}CH_3$)			X							X				X		X			X		
Acetaldehyde (CH_3CHO)																X					
Ammonia (NH_3)					X	X		X	X			X	X	X		X	X	X	X		X
Arsine (AsH_3)																X					
Automobile exhaust gases								X								X					X
Benzene (C_6H_6)																X					
Butane (C_4H_{10})	X							X	X	X						X			X		
Butanol									X					X		X			X		
Carbon dioxide (CO_2)	X	X	X	X	X	X	X			X			X			X	X		X	X	X
Carbon monoxide (CO)		X				X	X	X	X	X		X	X	X		X	X	X	X	X	X
Chlorine (Cl)									X							X					
Dimethyl disulfide																X			X		
Dimethylamine (DMA)									X					X		X	X	X	X		
Ethane (C_2H_6)																			X		
Ethanol (C_2H_5OH)	X			X			X	X	X	X		X		X		X	X	X	X	X	X
Humidity (H_2O)	X									X	X				X	X		X	X		X
Hydrocarbons (HC)																X				X	X
Hydrogen (H_2)	X	X	X	X	X		X		X	X			X			X	X	X	X		X
Hydrogen sulfide (H_2S)				X			X									X		X	X		X
Inflammable Gases																X					
Liq Petroleum Gas (LPG)								X		X						X			X		X
Methane (CH_4)					X	X		X		X			X			X	X		X		X
Methanol (CH_3OH)	X			X												X	X				
Methyl mercaptan (CH_3SH)																X					
NO, NO_2, NO_x					X	X		X	X	X		X	X			X	X	X	X	X	X
Oxygen (O_2)	X	X	X	X	X	X	X	X		X		X	X			X	X	X	X	X	X
o-xylene																X					
Ozone (O_3)									X	X		X				X	X	X	X		X
Petrol/Gasoline																X		X	X		
Phosphine (PH_3)																X					
Propane (C_3H_8)						X		X	X	X						X			X		
Propanol (C_3H_7OH)									X					X		X	X		X		
Smoke		X														X					
Sulfur dioxide (SO_2)													X			X					X
Trimethylamine (TMA)									X					X		X	X	X	X		

Figure 1.2: Table summarizing solid state gas sensing research. Reprinted with permission [2].

can be used to generate complex chemical compositional analysis. The authors compile previously published data collected from a large range of metal oxide gas sensors and compares their selectivity to specific gases at specific temperatures. They also review the knowledge and technology available for making a metal oxide based gas fingerprinting system. Developing gas fingerprinting analysis involves comparing the relative changes in resistance of materials when they are subject to specific analyte gases. The data presented in Figure 1.2 is indicative of the potential to analyze data from a select range of metal oxide sensors in order to determine the presence and concentration of specific gases. Semiconductor oxides such as tantalum pentoxide (Ta_2O_5) and manganese dioxide (MnO_2) can be specifically employed to monitor system humidity while materials such as tin dioxide (SnO_2) has been shown to be one of the few metals that can be used to detect phosphene.

Early investigation into the dependance of MO_x gas sensor sensitivity on crystallite size showed a significant increase in sensitivity as crystallite size (D) dropped to less than twice the depth (L) of the surface charge region (SCR) [8]. Three predominant techniques have been developed in order to decrease crystallite size in metal oxide thin films. Colloidal thin film sensors with a particle diameter of $D < 2L$ can be developed and deposited through a combination of solution based synthesis and screen printing. Continuous and pore free sensing materials with a thickness less that L can be applied between electrodes and monitored for changes in resistance. Finally, one dimensional metal oxide nanowires, provide a substantial increase in the surface area to volume ratio. This has a substantial effect on sensor sensitivity.

Reliable gas sensing requires fine control of variables such as sensor surface temperature and sensor stability. Many metal oxide materials have been studied for their ability to exhibit increased long term reliability and stability in high temperature environments.

Detection mechanism of Metal Oxide Sensors

The basic functionality of n-type metal oxide gas sensing results from changes in concentration of easily ionizable oxygen vacancies (V_o). The charge carrier density near the surface of the oxide varies from that of the bulk material. Variations in the levels of trace

gaseous elements, such as carbon monoxide (CO), hydrogen sulphide (H_2S), and nitrogen oxide (NO_x) will drive reduction and oxidation reactions. Electron insertion and depletion due to these surface reactions changes the electrical properties of the surface layer. This skin depth is dictated by the Debye length (L_D) which is a measure of distance through a material where charge imbalances have an effect. It is desirable to construct nanowire sensors with a radius approximately equal to or less than the Debye length of that material. This would result in a sensing segment that can undergo complete resistive transformation that depends on the reactions occurring at its surface. This thickness criteria ensures a high sensitivity and is a predominant reason for extensive research in 1-Dimensional and porous 2-Dimensional gas sensors configurations.

1.3 Common Sensor Configurations

One and two dimensional structures have been explored for gas sensing due to their high surface area to volume ratio. A summary of benefits and detriments of common sensor structures is presented below.

1.3.1 Two Dimensional Structures

Techniques pertaining to thin film patterning have been well established in the microelectronics. Specific advances in microfabrication have played major roles in decreasing sensor power consumption and footprint while increasing reliability. Silicon based microhotplates provide a base with highly accurate temperature control on which micro and nanopatterned chemical sensors can be constructed. Reliable deposition methods, multilayer pattern alignment and established material etches makes the development of thin film based sensors a relatively straightforward endeavor. Gas detection becomes increasingly sensitive at smaller dimensions due to more reliable local temperature control, higher control over local morphology and porosity. Perhaps the greatest benefit of smaller dimension gas sensors is the substantial increase in surface area to volume ratio of the sensing material. Sensors have been created with sensing films less than 0.5 μm thick. As such, sensors are less dependant on sensing time delay caused by slow gas diffusion kinetics through the film. Two predominant thin film morphologies and

their relative benefits pertaining to fabrication and gas sensing are discussed below.

Particle Based Thin Films

Screen printing has been a reliable method used to produce WO_3 thick film sensors [9, 10]. The reaction time required to produce a viable change in conductance of the film upon exposure to NO_x is on the order of several minutes. The thickness of the particle based thick films also causes restriction in the ability for gases to diffuse into the film. This results in a low sensitivity of about 1 to 3 at low ppm concentrations. While the production of these thick films is straightforward, their utility as functional gas sensors is relatively low.

Continuous Thin Film

The production of continuous MO_x thin films such as WO_3 through sputtering [11], pulsed laser deposition [12], electrodeposition and evaporation led to increased sensitivity and decreased reaction times. Continuous thin film gas sensors have shown high sensitivities to gases such as NO_x at temperatures below $300\,^{\circ}\mathrm{C}$ [13]. An increase in sensitivity and substantial decrease in detection time is obtainable when films are grown via PVD or CVD [14–16].

1.3.2 One Dimensional Structures

One dimensional gas sensing elements are desirable due to their increased surface area to volume ratio as well as their smaller size. Much research focus has been placed on the production and attachment of these wires in a repeatable and reliable manner. Many groups have succeeded at demonstrating viability of these elements as gas sensors in a laboratory setting, but a void in nanowire based commercial sensor market exists.

Nanowires and Nanobelts

Metal oxide nanowires can be fabricated through a variety of methods including chemical synthesis, electrodeposition and physical deposition [17]. The use of nanowire mats has shown increased gas sensitivity over nanoparticle thin films [18], however, reliable gas detection with single nanowires and nanobelts offers the greatest sensitivity. The

production and analysis of metal oxide doped vanadium oxide nanobelts by Liu *et al.* demonstrates how minor modifications to such sensing structures can enable fingerprinting of analyte gases through conductimetric sensing [19].

Initially gas detection using nanowires or nanobelts required complicated patterning procedures to connect to the ends of the sensing element. Minor orientation variations cause the length of resistive metal oxide nanowire between electrodes to vary considerably. Until recently these fabrication difficulties restricted the use of nanowire sensors from mass production. A solution has been found with dielectrophoresis. Dielectrophoresis enables the site specific placement of nanowires from a solution between two conducting electrodes. A non-uniform alternating current electric field is used to orient nanowires between two electrodes. Once a wire attaches to both electrodes a conduction path is created. This shorts out the localized capacitively driven field [20–22]. Sequential dielectrophoretic attachment enables an array of complementary MO_x nanowires to be attached in a desired configuration. This attachment method is a significant step forward in the quest for a low power, low footprint and highly sensitive electronic gas sensor.

1.4 Tungsten Trioxide

Tungsten trioxide has shown promise as a gas sensor for NO_x [12, 18, 23], CO [4] and H_2S [2]. Each of these gases have been detected at low ppm concentration using simple resistance based measurements across WO_3 thin films. Low concentration gas sensing is required for sensitive and selective chemical measurements suitable for practical applications. A variety of practical WO_3 synthesis methods including electrodeposition [24], thermal reactive evaopration [4, 23], chemical vapor deposition and sol gel dispersion offers substantial flexibility during gas sensor fabrication. These fabrication methods have produced both nanoparticle thin films as well as one dimensional nanowires [18]. Reyes *et al.* have investigated methods to increase utility of WO_3 thin film sensors [4]. They have demonstrated that tungsten trioxide sensors exhibit a temperature dependant peak in analyte gas sensitivity. Maximum analyte sensitivity for low concentration H_2S (10 ppm), CO (100 ppm) and NO_2 (5 ppm) were shown to occur at 375K, 525K and 700K, respectively.

2
Literature Review

Successful gas sensor fabrication relies on achieving a balance between backwards compatible fabrication steps, high process yield, and low process complexity. Fabrication techniques initially developed for integrated circuit design can be altered to allow deposition of a specific material while maintaining process compatible patterning. This chapter outlines well established process and characterization methods involved. The specifics surrounding metal oxide sensor fabrication will be discussed further in subsequent chapters.

2.1 Gas Sensing Platforms

A number of gas sensing platforms exist. Each platform has specific strengths which can be suited for specific applications. Technological advances in sensor fabrication and signal analysis have substantially advanced gas detection over the last decade. Optical gas detection methods benefit from smaller optics with few defects. Gravimetric gas analysis has benefited greatly from advances in gas selective polymer coatings, while metal oxide conductimetric gas sensing relies on recently developed low power surface temperature control methods and structures. A review of several common gas detection methods is presented below.

2.1.1 Optical Gas Sensors

Optical measurement techniques such as surface plasmon resonance (SPR) and laser absorbance spectroscopy enables instantaneous detection of analyte gases. Currently optical sensing suffers from a relatively large footprint and high power consumption. The ever increasing use of diode laser sources, waveguides and microfabricated optical sensors is rapidly advancing room temperature analyte gas detection.

Surface Plasmon Resonance

SPR functions through measuring changes in the refractive index at the plane interface of two materials with dielectric constants of opposite sign, such as a dielectric and a metal [25]. A surface plasma wave is described as a TM-polarized wave with a propagation constant(β) described by:

$$\beta = k\sqrt{\frac{\varepsilon_m n_s^2}{\varepsilon_m + n_s^2}}, \tag{2.1}$$

where k is the free space wave number, ε_m refers to the dielectric constant of the metal ($\varepsilon_m = \varepsilon_{mr} + i\varepsilon_{mi}$) and n_s is the refractive index of the dielectric [26].

Excitation of SPR can be measured by analyzing the wavelength modulation, phase modulation [27], intensity modulation [25], or angle modulation [28] of the reflected light [29]. SPR based chemical sensors can be achieved by monitoring changes in the

optical properties of a transducing material due to conditions at the interaction between optical radiation and surface plasmons.

Obreja *et al.* have produced micro scale prism coupled SPR sensors using polymer prisms of PDMS, epoxy resin and PMMA in a Kretschmann configuration [25].

It was found that SPR compatible metal nanoparticles could be impregnated into gas selective polymer thin films. The combination allows for an increased range of detectable analyte gases as well as enhanced sensor selectivity. El-Basaty *et al.* also used the prism coupled Kretschmann configuration for NO_2 sensing [28]. This was accomplished through the addition of a cobaltphthalocyanine (Co-Pc) layer on a thin silver film. The phthalocyanine layer undergoes charge transfer reactions with adsorbed electron acceptor gases such as NO_2. The measured detection time was several seconds while the calculated detection limit of the Co-Pc layer was about 0.07 ppm. Manera *et al.* have shown that nobel metal particulate doping of titanium dioxide (TiO_2) thin films enables SPR monitoring of methanol detection. The interaction of methanol with TiO_2 doped with gold nanoparticles showed instantly measurable changes in the real component of the refractive index [30].

Infrared (IR) Spectroscopy:

Absorbtion spectroscopy is achieved by monitoring the transmitted (V_t) and incident (V_o) light intensities of lasers traveling through an optical cavity and have been shown to produce sub parts per billion (ppb) level detection [31]. Laser absorbtion can be explained by the Beer-Lambert equations [32]:

$$\frac{V_t}{V_0} = exp(-k_v L), \tag{2.2}$$

where k_v is the spectral absorbtion coefficient and L is the path length. k_v is defined by:

$$k_v = PS(T)(v_0)\Phi(\nu - \nu_0), \tag{2.3}$$

where P is the partial pressure of the absorbing species, $S(T)$ is the line strength, T is the temperature in degrees Kelvin, Φ is the line shape function which is centered at the gas absorption frequency ν_0 [32].

Equations 2.2 and 2.3 show that gas identification relies on the wavelength of the

laser being close to that of a point on the absorbtion spectra of an analyte gas. A large variety of optical sources exist allowing the choice between broadband (multi-wavelength) and narrow band (monochromatic) IR-sensors. Broadband IR sources, such as quantum cascade lasers (QCL), enable the simultaneous detection of several analyte species via spectroscopic analysis while monochromatic sources allow for higher sensitivity target analysis [33].

Trace levels of NO and CO_2 were measured via mid-infrared spectroscopy by McCurdy *et al.* as a method for monitoring human respiratory disorders [31]. They show that ppb concentrations of NO gas can be detected in less than 1 second. CO and H_20 were measured by Yao *et al.* using a single diode laser source tunable to both 6667 cm^{-1}(1.5 μm) and 6369 cm^{-1}(1.57 μm) [34]. A tunable laser centered at 970 cm^{-1} (10.3 μm) was used by Manne *et al.* in a multipass configuration to measure environmental gases across a $\sim 1.74cm^{-1}$ (5747 μm) spectral window. H_2O and CO_2 have spectral lines within this window which were matched to spectra stored in the HITRAN [35] database. The database was then used to identify the remaining signal components. NH_3 and C_2H_4 were identified. This open cell multi-pass setup was able to identify and produce a spectral fingerprint for these gases at concentrations of $\sim 3ppb$ and $\sim 5ppb$, respectively [36].

Fiber-optics rely on the internal propagation of light though total internal reflection [33]. Novel optical chemical sensors have been produced by flowing analyte gases though hollow core infrared waveguide (HCW) fiber-optic wires. The combination of HCWs and QCLs offers a gas analysis method with a detection time on the order of a few seconds and a minimum detection level in the low ppb range [37, 38]. In contrast to open path and multipass systems, HCW has a detection volume of a few mililiters [37] which drastically reduces the footprint and increases the portability of optical gas analyzers.

2.1.2 Gravimetric Gas Sensors

Gravimetric gas sensors such as quartz crystal microbalances (QCM) and surface acoustic wave (SAW) sensors have commonly leveraged the analyte selectivity exhibited by polymers to detect volatile organic compounds. These sensors are easily manufactured, occupy a small foot print and operate at room temperature. Their basic functionality centers

around an adsorbed or absorbed analyte mass induced resonance frequency shift from the fundamental mode. This shift can be measured with simple electronic circuitry.

QCM

A piezoelectric quartz crystal microbalance (QCM) is very sensitive to changes in mass. A piezoelectric material can be distorted through the application of a differential voltage across the crystal. A change in the surface bound mass on QCM can be measured by a shift in its resonant frequency. This shift can be described by the Sauerbrey equation [39]:

$$\Delta f = \frac{-2f_o^2 m_f}{A\sqrt{\mu_q \rho_q},} \tag{2.4}$$

where Δf is the change in resonant frequency, f_o is the fundamental mode resonant frequency of the QCM, m_f is the change in mass loading of the resonator surface, A is the piezoelectric active area, ρ_q is the density of the quartz and μ_q is the shear modulus. The QCM can be covered with a analyte selective polymer to facilitate gas detection. Gas diffusion into the surface coating changes the volume of the polymer which induces a frequency shift in the QCM [29]. Gas sensing using various polymer coated QCMs have predominantly been used to target volatile organic compounds [40]. Although it has been shown that sensor sensitivity can be increased by operating the QCM at higher resonant modes [40], detection time is limited by analyte diffusion into the surface polymer.

SAW

The use of surface acoustic wave (SAW) sensors have been shown to provide higher measurement resolution due to their higher operating frequency [41]. A surface acoustic wave can be generated on the surface of a piezoelectric material by applying a high frequency AC differential voltage between two micropatterned electrodes on the piezoelectric crystal surface. The resulting induced mechanical vibrations travel across the piezoelectric material surface and can be monitored by a similar set of interdigitated electrodes.

Analyte detection and sensitivity is governed by a thin polymer surface coating, similar to the QCM. Sorption of the analyte gas induces a frequency shift (Δf_v) described by [29]:

$$\Delta f_v = \frac{\Delta f_p c_v K_p}{\rho_p}, \tag{2.5}$$

where f_p is the frequency shift due to the surface polymer, c_v is the vapor concentration, K_p is the partition coefficient and ρ_p is the density of the polymer membrane used.

SAW sensors have been shown to detect many inorganic and organic gases such as NO_2, H_2, H_2S, SO_2 and CH_4, C_6H_6, C_2H_5OH, respectively [29]. Sadek *et al.* have shown enhanced sensitivity to H_2 gas by the chemical polymerization of WO_3 [42]. Additionally, the porous nanofibril polyaniline/WO_3 structure significantly decreased sensor response time by substantially increasing the surface area to volume ratio of the film.

2.1.3 Capacitive Gas Sensors

Organic polymer films can be applied between two electrodes to form a capacitive structure. Capacitive sensors function by comparing the capacitance value during two steady state scenarios. Capacitance can generally be described by the equation:

$$C = \frac{\epsilon A}{d}, \tag{2.6}$$

where ϵ is the dielectric constant, A is the surface area of each of the two plates, and d is the distance between the two plates [43]. Initial capacitance measurements are obtained in an analyte free environment. Both the dielectric constant and the volume of the polymer changes when an analyte gas is introduced into the system and absorbed into the polymer thin film [29]. Oikonomou *et al.* describe a 2-hydroxy ethyl methacrylate(PHEMA)-$BaTiO_3$ nanocomposite based chemocapacitive sensor which was used to monitor relative humidity [44]. The combination of high dielectric constant material such as $BaTiO_3$ with a polymer that exhibits high levels of swelling upon exposure to humidity provides an excellent example of the augmented effect that polymer impregnation provides. Capacitive sensors have a small footprint, use low power, and have been shown to exhibit high sensitivity, however, their dependance on analyte diffusion through the polymer greatly limits detection time and sensitivity.

2.1.4 Conductimetric Gas Sensors

Conductimetric sensing functions by measuring the change in sensor resistance due to the presence of an analyte gas. Conduction models are rooted in Ohm's Law ($V = IR$), but factors such as temperature, nanocrystallite size, sensor thickness, gas concentration and film thickness must also be taken into account to accurately analyze chemical reactions [45].

Metal oxide gas sensors seek to provide a reliable system for gas fingerprinting that is compact and portable, low cost, consumes low amounts of power, reliable, sensitive and accurate. It has been determined that the simultaneous monitoring of various MO_x micro and nanostructures would enable the realization of exactly such a system [2]. The sensor would not require a large footprint due to long optical path lengths [31, 36] and nor the complex optics required for optical sensing. The sensors would also not require complex frequency sensing circuitry required for gravimetric and capacitive gas detection [44]. Most importantly, MO_x sensors can be easily fabricated onto reliable thermally stable microhotplates with which temperature can be accurately controlled. This increases the selectivity for analyte gases while reducing the need for frequent calibrations due to thermal drift [46].

Figure 2.1 shows the fabrication components required of a temperature controlled microhotplate gas sensor. Each component of this microhotplate can be easily fabricated through common techniques such as optical lithography, sputtering and anisotropic silicon wet etching. Examples of such hotplates can be found in literature [14, 23], and have primarily been used to enable thin film sensor layouts. Although this configuration limits each microhotplate to support only one material, sensor fabrication techniques, including dielectrophoresis [21] and photolithography, have been developed to create a dense array of various one and two-dimensional sensors on one hotplate. Integration of several microhotplates enables the simultaneous use of various gas detecting materials at their respective optimal operating temperatures.

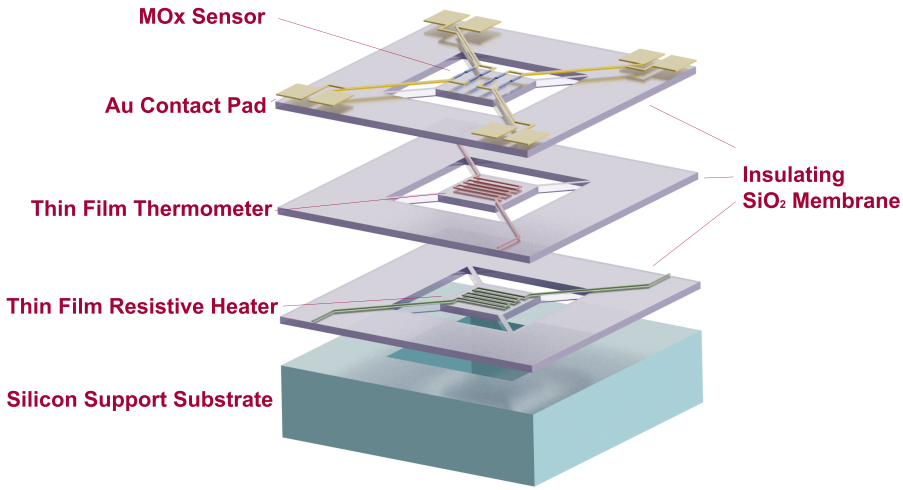

Figure 2.1: Figure describing the layout of a suspended microhotplate sensor.

2.2 Conduction Model

Two major categories of gas sensing conduction models exist. Geometric factors such as porosity and material thickness prohibits chemical access to a given proportion of the sensing material. Considering that sensor conduction is based on surface chemical reactions, wires or released beams with a maximum material thickness d, and Debye length x_0, will undergo the greatest gas dependant conduction changes when $d/2 < x_0$. Surface reactions induce charge transfer between the bulk material and its surface in order to establish thermal equilibrium. This results in a non-neutral region in the bulk known as the surface space charge region, shown in Figure 2.2 [3]. Although x_0 is shown as an abrupt change to complete carrier depletion, this is only true within a few Debye lengths of the surface.

The conditions of charge neutrality define the constant balance between a surface chemical reaction and the reactionary effect within a material. The net surface charge on a semiconducting material is balanced by an opposing charge depletion in the SCR. In a wide band gap n-type semiconductor such as tin oxide (SnO_2) and tungsten trioxide (WO_3) the SCR depth (x_0) is dependant on the Debye lengths of the material, which is in turn temperature dependant. This is illustrated by the equations:

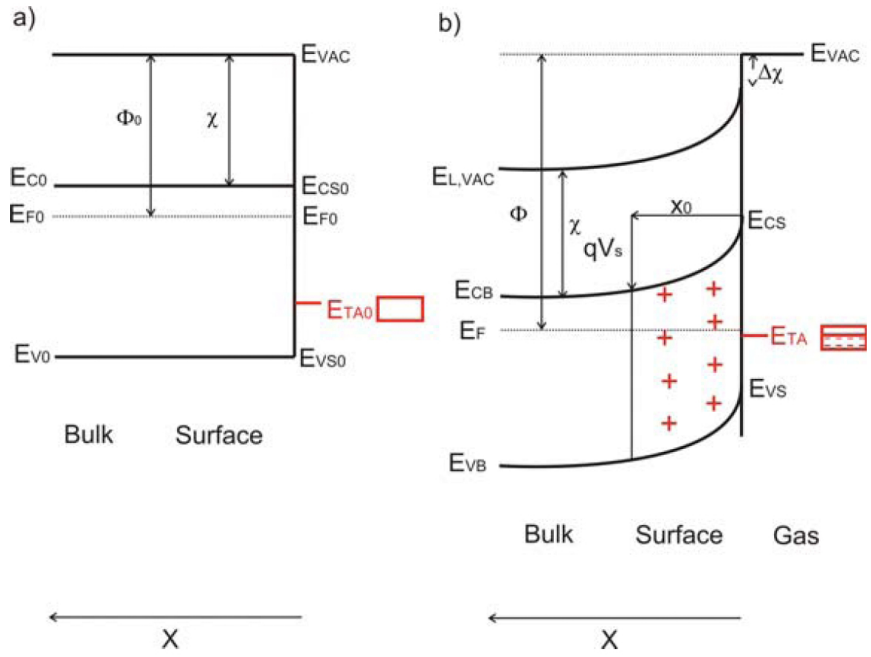

Figure 2.2: Band model of an n-type semiconductor showing formation of the SCR (a) before and (b) after surface oxygen adsorption. Reprinted with permission [3].

$$x_0 = L_D \sqrt{\frac{2V_s q}{kT}} \tag{2.7}$$

and

$$L_D = \sqrt{\frac{\varepsilon kT}{q^2 N_d}}, \tag{2.8}$$

where V_s is the surface/bulk potential barrier, q is the absolute value of the electron charge, k is the Bolzmann constant, T is the absolute temperature, ε is the dielectric permittivity of the semiconductor and N_d refers to the density of surface donor dopants.

Oxygen Vacancies

Oxygen desorption from a metal oxide surface will occur even under moderate annealing in an inert atmosphere, a reducing atmosphere or under vacuum. The deposition process leaves behind oxygen vacancies which results in a filled (donor) intragap state lying just below the conduction band [47]. Creation of these states reduces thermal energy required to ionize a large portion of electrons in an insulating metal oxide, effectively turning the

material into an n-type semiconductor.

Oxygen vacancy formation on tungsten trioxide can be observed in Equation 2.9 [48]

$$W_nO_{3n} \rightarrow W_nO_{3n-1}V + \frac{1}{2}O_2. \tag{2.9}$$

The corresponding energy of vacancy formation is given by

$$E_f = E(W_nO_{3n-1}V) + E(\frac{1}{2}O_2) - E(W_nO_{3n}), \tag{2.10}$$

where E is the corresponding energy of each state and n is the number of tungsten atoms in a given super cell [48].

Oxygen Adsorption and Desorption

Initial gas adsorption onto a surface proceeds in two steps: physisorption and chemisorption. Dipole interactions and weak van der Waals forces initially drive physisorption. The Lennard-Jones model shows that sufficient thermal energy in the system drives chemisorption [3]. Molecular O_2 will dissociate into two surface ions upon initial exposure to oxygen. These ions achieve a lower energy state. Equilibrium state ionsorbed oxygen coverage (θ) has been described by Kolmakov *et al.* through the following relations [47]:

$$\frac{\beta}{2}O^2_{(g)} + \alpha \cdot e^- + N_s \rightleftharpoons O^{-\alpha}_{\beta S} \tag{2.11}$$

$$k_{ads} \cdot N_s \cdot n \cdot p^{\frac{\beta}{2}}_{O_2} = k_{des} \cdot \theta. \tag{2.12}$$

In Equation 2.11 $O^{-\alpha}_{(\beta S)}$ refers to the general form of ionsorbed oxygen, N_s is the concentration of oxygen vacancy sites and *n* is the concentration of free electrons. α and β accounts for the charge and temperature dependant shifts in the molecular and atomic oxygen nature. O^-_2 dominates below 500K and O^- dominates at higher temperatures. $k_{ads/des}$ refers to the temperature dependant adsorption/desorption rate constants, while $p^{\frac{\beta}{2}}_{O_2}$ is the oxygen partial pressure in the system.

Equations relating the change in wire conductivity to the above described oxidation reactions for a wire structure with $d/2 < x_0$ can be explained as follows [47]:

$$\Delta G = \frac{\pi R^2 q \mu \Delta n}{L} \tag{2.13}$$

where

$$\Delta n = \frac{2N_s\theta}{R}, \tag{2.14}$$

R is wire radius and L its length, q is electron charge, μ and n are electron mobility and concentration, respectively.

Gas Detection Reactions

There are three categories of chemical reactions that will impact semiconductor conductimetric gas sensing. Reducing gases, such as CO, will react with the ionosorbed oxygen species, releasing electrons into the sensing material, which restores electrons to the depletion layer.

$$CO_{(g)} + O^-_{(s)} \rightarrow CO_{2(g)} + e^- \tag{2.15}$$

In a similar manner, oxidizing gases, such as NO_x will further increase the surface resistance of MO_x sensors by reacting with the remaining surface oxygen vacancies. Reactions with NO_2, N_2O and NO are described below:

NO_2**:**

$$NO_{2(g)} + V_o \rightarrow (V_o - O_{ads}) + NO_{(g)} \tag{2.16}$$

$$2(V_o - O_{ads}) \rightarrow 2V_{o(s)} + O_{2(g)} \tag{2.17}$$

N_2O**:**

$$N_2O_{(g)} + V_o \rightarrow (V_o - O_{ads}) + N_{2(g)} \tag{2.18}$$

NO**:**

$$NO_{(g)} + V_o \rightarrow (V_o - O_{ads}) + \frac{1}{2}N_{2(g)} \tag{2.19}$$

.

The third category relates to gases that react not with adsorbed surface species, but chemically modifies the MO_x sensor itself. WO_3 has been shown to act like an n-type semiconductor [49]. The reaction of H_2S with WO_3 to form tungsten sulphide decreases sensor resistance and can be described by the following chemical equation [4]:

$$3WO_{3(s)} + 7H_2S_{(g)} \leftrightarrow 3WS_{2(s)} + SO_{2(g)} + 7H_2O \tag{2.20}$$

2.3 Metal Oxide Fabrication Methods

A major focus of this project is the micro and nanomachining of tungsten trioxide. WO_3 has been under investigation for many years for its electrochromic and gas sensing properties. It has been shown that WO_3 nanoparticles can be produced through a variety of methods including combustion synthesis [50], electrochemical synthesis and sol gel synthesis. Highly porous WO_3 films have been formed by drying nanoparticle suspensions over a sensing platform. Amorphous WO_3 thin films have been formed from a peroxytungstate precursor though electrochemical means [51–55]. Tungsten trioxide nanowires have also been formed through PVD, CVD, sol gel synthesis and electrochemical means.

Although many of these metal oxide production methods are well studied, this project focussed on two major project goals that have previously been unexplored. The top down fabrication of amorphous WO_3 suspended beams allows for large scale two point sensor elements to be accurately aligned and integrated with prefabricated circuitry. In addition, the creation of very high surface area to volume ratio pseudo one dimensional gas sensing elements via templated electrodeposition was investigated.

2.3.1 Electrodeposition

Electrodeposition is a process through which current is used to drive a reduction oxidation (RedOx) reaction in a solution to coat a desired material on an electrode. A general equation describing basic RedOx reactions shows that electrons can be supplied to convert a species to a reduced form.

$$Ox^{z^+} + ze^- \xrightarrow{electrode} Red \tag{2.21}$$

Generally speaking, a positively charged anode and a negatively charged cathode will create a potential imbalance in a solution

Current flow through an electroplating cell can be simplistically described through Ohm's Law:

$$V = IR, \tag{2.22}$$

where V is the voltage dropped across the cell, I is a measure of the flow of charge through the cell, and R is the combined resistance of various resistive components in the cell. Electroplating cells can be established in two different configurations: Galvanostatic and Potentiostatic.

Galvanostatic deposition maintains a constant cell current. This allows the relative electrode potential to drift and drive the reactions necessary to maintain a set charge flow through the cell. Constant current deposition is used primarily to control the deposition rate and can be used to tune the stress and thickness of the final deposit. Precautions must be taken to ensure that solution reactant depletion will not occur during the deposition process. If the desired ions are depleted from the solution the voltage will rise to accommodate the next energetically favorable reaction which could result in the deposition of a second material. In an aqueous solution this can also often result in unwanted surface contamination of the deposit or electrolysis of H_2O. A simple two electrode configuration is all that is needed for such deposition.

Potentiostatic deposition is used to precisely control the potential of the working electrode (WE) relative to the potential of the solution. This setup is much like that of a galvanostatic cell, but a reference electrode is placed in proximity to the WE.

2.3.2 Templated Electrodeposition

Fabrication of highly ordered uniform pores in aluminum oxide has been well documented [56, 57]. Solution based metal and metal oxide deposition onto a conductive electrode

combined with the insulating nature of aluminum oxide lends itself well to template assisted nanowire growth.

Although reported research has been directed predominantly at porous anodic alumina and track etched polycarbonate templates, silicon micropores have also been developed by Matthias *et al* [58] and Muller *et al.* [59]. Matthias et al. reports the creation of modulated Au microwires in a hydrofluoric acid etched template. This emphasizes the versatility of novel etching techniques to provide highly tuneable dimensions in electroplated materials.

2.3.3 Electroless deposition

The electroless deposition of tungsten trioxide has been used to generate porous metal oxide thin films [60, 61]. Electroless deposition varies from traditional electrodeposition in that it does not require an external power supply to drive the deposition reaction. A reducing agent in the solution is used to drive deposition onto the electrode. In contrast to equation 2.21 electroless plating can be described by the reaction:

$$MOx^{z+}_{solution} + Red_{solution} \xrightarrow{catalytic\ surface} MOx_{lattice} + Ox_{solution}. \tag{2.23}$$

2.3.4 Solution Phase Synthesis

Several research groups have explored the use of solution phase synthesis to either grow nanowires [17] or produce colloidal based metal oxide thin films.

Colloidal films are often produced by the spontaneous precipitation of metal oxide crystals from a solution. Drops of suspended nanoparticles can be accurately printed onto interdigitated electrodes for sensing. While organic binders hold the suspension together, sintering is required to link the particles into a continuous film. The thick films formed by this method tend to exhibit slow and relatively insensitive gas sensing properties.

2.3.5 Physical Vapor Deposition

Physical vapor deposition can generally be divided into three categories: sputtering, evaporation, and pulsed laser deposition.

Sputter deposition of WO_3 thin films has long been investigated for gas detection

[11, 62]. The thin films produced through sputtering are generally smooth and continuous. Sputter deposition is often used to combat the large discontinuous cracks formed during screen printed thick films [13].

The reactive physical vapor deposition of WO_x nanowires resulted in the high density growth of $W_{20}O_{58}$ nanowires on a silicon substrate by Chen *et al* [63], while Reyes *et al* produced nanocrystalline thin films though a similar method [4].

Pulsed laser deposition of metal oxide thin films for gas detection has been used due to its ability to deposit high quality complex films. Pressed powder target pellets are pulsed-laser ablated under vacuum. The vapor travels across a vacuum chamber and deposits on a substrate. The addition of film dopants is possible due to the use of powder pressed pellets as a material source. Zaho *et al* used this method to investigate the effects of aluminium and titanium doping in nanocrystalline WO_3 thin films on NO_x detection [12].

2.3.6 Chemical Vapor Deposition

Chemical vapor deposition occurs when gas phase reactants undergo temperature dependant chemical transformation. Precursor gas decomposition results in the deposition of a desired material. The remaining gas phase reactants are pumped from the system to facilitate continued deposition. Advances in microhotplate technology have enabled localized controlled growth of metal oxide thin films to complete the fabrication of resistive sensing elements [14, 16]. Microhotplate temperature can be controlled with built in resistive elements and is usually maintained between $350\,^{\circ}\mathrm{C}$ and $500\,^{\circ}\mathrm{C}$, depending on the precursor gas and process parameters [15].

The primary benefit of metal oxide CVD over related chemical sensor fabrication techniques is that deposition is temperature dependant and can be precisely locally controlled. This enables the creation of an array of sensing elements on which select oxides can be deposited on specific elements.

2.4 Metal Thin Film Fabrication Techniques

Established patterning techniques involving sputtering, optical lithography and wet chemical etching provide a set of techniques that can be used to create structures and

patterns required in conductimetric metal oxide gas sensors. Much of the the information presented here is processing developed in the University of Alberta Nanofab.

2.4.1 Sputter Deposition

Sputtering involves the atomic deposition of materials in a vacuum environment [64]. Layers are successively deposited, with the surface layer deposited last.

A three gun system allows one to sputter up to three successive materials. For example, an adhesion layer can first be sputtered so that successive films will adhere to the substrate. A thick seed layer on which electrical deposition will occur can then be sputtered on to the adhesion layer. This is followed by sputtering a final capping layer which will eventually be patterned into chemically inert electrical traces.

Sputtering at 300 W with a 7 mTorr chamber pressure, regulated with argon flow, is an in-house standard for virtually all standard sputtered metals. This does not apply to the more expensive platinum and gold, which are commonly sputtered at the same pressure but at a lower power of 75 W.

Only about 5 to 10 nanometers of chromium (Cr) is necessary for an adhesion layer. Its thickness, however, must support sufficient current flow to drive WO_3 electrodeposition. Chromium thin films develop relatively high amounts of stress when they are sputtered and a suitable initial seed layer thickness should be as thin as is practical.

Substrates are placed into the sputter chamber which is then evacuated to a base pressure between 10^-6 Torr to 10^-7 Torr range. This is done to remove most of the gaseous molecules from the chamber in order to avoid contaminating the sputtered film. A pure argon flow is introduced to the chamber and the chamber pressure is brought up to 7 mTorr. A 300 W plasma is established over the Cr source, however a shutter remains in place to prevent sputtering onto the substrate until the possibly contaminated and oxidized top layer of the Cr has been sputtered away. The is generally referred to as "burning in the target". At this power and pressure, Cr sputters at about 6 nm/min, therefore after the sputter shutter was opened, the power supply was left on for only 60 seconds. To limit deposition rate of an expensive material that is only generally applied in sub 100nm layers, Au is sputtered at 75 W. At 7 mTorr this translates into approximately a 10 nm/min deposition rate.

2.4.2 Optical Lithography

The University of Albert Nanofabrication facility has developed a standard photolithography process for Shipley 504 positive resist. With this process it is possible to create a 1.2 μm thick resist pattern with a minimum feature size of approximately 1 μm. Lithography is comprised of 5 sub-steps. To generate a pattern one must apply the resist, bake the resist, allow it to rehydrate, expose the pattern, then develop and clean the final pattern. This process will be referred to extensively throughout the rest of the thesis.

Spinning and Baking:

A Solitec Spinner is used to spin the substrate at preset speeds which will spread photoresist evenly across the substrate. After spinning the photoresist still contains solvent that needs to be removed before continuing with alignment and exposure. Driving the solvents from HPR 504 by baking at $115\,^{\circ}\mathrm{C}$ for 90 seconds before patterning cures the resist and causes it to harden. This ensures thin features with an aspect ration greater than 1:1 retain their form while reducing the amount of resist that adheres to, and contaminates, the mask. It has been reported that photolysis occurs when DQN positive resists such as HPR 504 is exposed. Exposure parameters depend on the presence of H_2O in the resist [64]. For consistent accurate results it is recommended to cool the substrate and allow the resist to rehydrate for approximately 15 minutes after baking.

Exposure:

Wafer patterning is often aligned with the crystal plane of the silicon substrate for two reasons. The first is that select silicon etching techniques such as potassium hydroxide etch preferentially along silicon planes and can be used for select anisotropic etch processes. The second reason is to allow the simultaneous manufacturing of multiple patterns on each substrate. At the end of processing the wafer must be divided into individual squares, also known as die.

Prior to exposure, the substrate is placed on the alignment chuck of the contact mode mask aligner and raised until it is within 2 mm of the mask. A built in CCD alignment system is used to align the flat of the wafer with the mask pattern. A leveling system is

engaged while bringing the substrate into initial contact with the mask. Contact vacuum is then used to maintain tight contact between the wafer and the mask.

Consistent photolithography can be attained by placing the surface of the wafer as close to the lithography mask as possible. This will reduce diffraction effects that can expose photoresist located underneath the outer edges of the chromium mask pattern. Generally minimum feature size can be related to gap distance by

$$W_min \approx \sqrt{k\lambda g}, \tag{2.24}$$

where *k* is a resist dependant constant, λ is the light wavelength, and *g* is the distance between the opaque metal layer on the mask and the substrate surface [64]. The resist dependant constant is generally close to 1. Close contact is generally achieved through contact vacuum pressing the wafer chuck into the mask. This causes *g* to be reduced to a distance on the same order as resist thickness. One notable disadvantage of establishing vacuum contact is the tendency for photoresist on and particulate on the substrate to adhere to the mask. Such contamination will create optical abberations during the optical lithography of subsequently processed substrates. These defects will translate directly into pattern abnormalities.

Optimal exposure parameters can be controlled to produce submicron features in a 1.2 μm thick film of HPR 504. Underexposure of the resist results in a low selectivity during developing, while overexposing of the pattern can result in some features being washed out as well as artifacts such as notching of convex pattern corners. The resist parameters dictate an excellent reaction response when exposed to light at wavelengths of 405 nm and 365 nm. A critical dose of light is also needed to ensure that chemical solubility will occur throughout the entire depth of the resist. Optimal exposure time was determined to be 1.9 seconds. After exposure the contact vacuum is turned off and the wafer is slowly lowered.

Photoresist Developing:

Shipley Microposit 354 developer is specifically designed to remove exposed areas of HPR 504 resist. Exposed areas are selectively dissolved by the developer and washed away. Only areas that were not previously exposed remained covered by resist. Fresh 354 developer

develop the above processed resist in 17 seconds.

2.4.3 Wet Chemical Etching

Wet chemistry plays a crucial role in microfabrication. Although the isotropic nature of wet etching is often a determent, the wide variety of metal etches that exist today allow for excellent etch selectivity. Photo resist masks prevents etchant access to resist covered areas of the substrate. Exposed layers will be removed by submerging a patterned substrate in chemical etchant. Often an etchant can be found with sufficient etch selectivity so that the underlying layer will act as an etch stop and not be affected. Extensive documentation has been developed which can be used to compare the effects of specific etchants on various materials [65, 66].

Electrical traces used to conduct current to the chemically reactive metal oxide thin film sensing elements can be easily fabricated with relatively inert metals. Gold is ideally suited for this task but required an adhesion layer to remain attached to the smooth silicon substrate. Additional process complexity, such as including additional material layers, requires thorough investigation of etchant compatibility. Materials which do not require etching may still be exposed to the etchant and must not undergo adverse reactions. Such compatibility issues are investigated in this section.

A prime example of some etch chemistries that were compatible with the fabrication of WO_3 gas sensors can be illustrated by looking at fabricating a suspended WO_3 beam above an insulating substrate with chemically inert electrical contact points for viable wire bonding. Gold can easily be etched by a commercially available combination of iodine (I_2), potassium iodide (KI) and H_2O. An adhesion layer for the gold is required so that the gold does not delaminate from the SiO_2 surface over time. Generally either titanium (Ti) or chromium (Cr) is used as conductive adhesion layers. Titanium can be etched with hydrofluoric acid, while chromium can be patterned with a commercially available chromium etchant (CR-7).

It has been shown that neither Ti nor Cr are affected by gold etchant and gold is not affected by CR-7 [66]. The process was developed such that the sensing material would be deposited after the gold was patterned, but before the adhesion layer was etched away. This

creates the specific requirement that the etchant for the adhesion layer must be compatible with the sensing metal oxide. The metal oxide etch must also not modify the adhesion layer. It was found that WO_3 could be patterned with sodium hydroxide ($NaOH$), which was compatible with both chromium and titanium [65]. It was subsequently determined that WO_3 was not compatible with titanium etch due to its hydrofluoric acid content but was compatible with CR-7.

Finally, it must be noted that the minimum device critical dimension was on the scale of several micrometers. This allowed for the use of isotropic etchants for thin films. It can be seen that flexibility to vary materials and their respective etchants often requires extensive compatibility analysis, but ultimately allows successful fabrication of devices.

Stiction

One of the main contributors to low device yield during fabrication is collapse due to capillary forces. Microfabricated MEMS are generally only separated from the substrate below them by a few micrometers. During the release process doubly clamped beams are submersed in liquid and are free from the surface. Upon drying of the device, liquid evaporates from between the released beam and the substrate. Large yield losses occur if the evaporating liquid pulls the beam into contact with the substrate. Static friction (stiction) will then hold the beams down. This is one of the largest yield decreasing factors in surface micromachining [64].

The potential energy that can be attributed to surface tension can be described by the following equation:

$$U_{SurfaceTension} = -\int_0^l \int_0^{w(x)} \frac{\gamma_l(cos\theta_1 + cos\theta_2)b}{(d-w)} dw dx \tag{2.25}$$

where l is the beam length, γ_l is the liquid surface tension, θ_1 and θ_2 are the contact angles of the liquid with the two surfaces, b is the beam width, d is the initial distance between the beam and the substrate, and w is the deflection profile of the beam [67]. It is clear that reducing the surface tension of the liquids in contact with the beams immediately prior to substrate drying would decrease device stiction.

Haluzan *et al.* have developed a method by which to approximate the tendency of a

Liquid	Surface Tension ($\frac{mN}{m}$ @20 °C)	Reference
H_2O	71.98	[69]
Acetone	23.02	[69]
2-Propanol	21.74	[70]
n-Pentane	15.49	[71]

Table 2.1: A comparison of surface tension of various solvents at @20 °C

device to fail due to stiction by calculating its elastoplasticity number (N_{EC}) [68]. It has been determined that a doubly clamped beam will not touch the adjacent surface if $N_{EC} > 1$, where

$$N_{EC} = \frac{128}{15}\frac{Ed^2w^3}{\gamma_l cos\theta_c l^4(l+\frac{w}{h})}[1+\frac{2}{7}\frac{\sigma_R l^2}{Ew^2}+\frac{108}{245}\frac{d^2}{w^2}]. \tag{2.26}$$

and E refers to the Young's modulus and σ_R is the residual stress in the film.

Increased yield can be achieved by methodically reducing the surface tension of the solution surrounding a released beam prior to drying. An H_2O post release rinse can be diluted by acetone. This is followed by a transfer into pure acetone, which can then be diluted by a lower γ_l solution. These steps can be repeated until a desired solution surface tension is achieved. Table 2.1 shows the surface tension of various solvents used for beam release (as per discussion in Chapter 4). One can see the drastic effect such stepwise release may have.

An alternative release method developed to avoid stiction is critical point drying [72]. During critical point drying, liquid CO_2 is pumped into a chamber to replace the rinse fluid. The chamber is then subjected to a high pressure that brings the liquid CO_2 to its supercritical point, typically around 35 °C and 1100 psi [73]. At this critical point the interface between liquid and gas does not exist. An environment that negates the effects of surface tension is achieved, thereby circumventing the problems associated with stiction.

Upon experimental implementation of this procedure it was found that the force with which liquid CO_2 is injected into the chamber is enough to destroy the released devices. Supercritical point drying has proved a useful technique to avoid stiction during release but was not suitable for releasing WO_3 beams.

Plasma Etching

Plasma etching is primarily used to aid in cleaning organic photoresist scum from the surface of the substrate after optical photolithography. Reactive ion etching (RIE) can be employed to perform a variety of recipe dependant tasks including organic scum removal and metal etching. RIE combines two complimentary mechanisms in order to achieve a relatively anisotropic etch profile. Increased etch selectivity is achieved by introducing and ionizing an isotropically active chemical species. Etch directionality is achieved through the acceleration of ions (100 - 1000 eV) via a parallel plate electrode configuration [74].

2.5 Thin Film Stress

Intrinsic stress in a thin film can be either in a compressive state (film expansion) or tensile (film compression) state. When deposited on a substrate the residual stress in a film can change the surface curvature of the substrate. By analyzing the change in the bow of the substrate one can extract the stress of the film on its surface. A general equation to determine film stress is:

$$\sigma = \frac{\delta}{t}\frac{Y}{1-\upsilon}\frac{T^2}{3R^2}$$

where δ is the change in wafer deflection at the center of the wafer, *Y* is Young's modulus for the material, υ is Poisson's ratio, *t* is the film thickness, *R* is the radius of the wafer and *T* is the wafer thickness [64].

Hoffman performed a study initially investigating the origin of cracks in decorative chromium films [75]. The study describes very well the effects of sputter pressure on film stress for a variety of transition metals. In several cases it showed that by varying the sputter pressure a change from compressive to tensile stress in the thin film resulted. It was also shown that the point of stress transition occurs at higher relative pressures as atomic mass increases. The conclusion stated that the compressive stress is caused by energetic neutral particle bombardment.

3

Chemical Sensor Testing System

A balance between controlling experimental variables while retaining a viable application must be reached when testing for low concentration chemicals in a carrier gas. Variables such as analyte chemical concentration within the carrier gas, carrier gas composition, and sensor temperature may be controlled for experimental requirements. Being able to accurately record experimental results requires precise monitoring of impurity concentration within the reaction chamber, low signal to noise ratio in recorded analog data, and sufficient flexibility in the testing system to allow for an array of experiments.This project was about developing a novel platform which would be ideally suited to analyze the response of metal oxide gas sensors in a low concentration analyte gas environment. This chapter will describe the design and characterization of the gas testing system as well as additional capabilities that could be used in future tests.

3.1 Introduction

Accurate chemical detection relies on a multi-component system based on individual modules working in synchronization. The design must control factors that affect the chemical reaction such as temperature, gas flow, analyte to carrier gas ratio, and contaminant exclusion. In order to ensure a low probability of device failure the system must be easy to maintain and one should be able to monitor the functionality of each component in the system. There must be an electric circuit in place that can directly measure the electrical conductivity of the sensor as well as a method for recording and analyzing the data of interest. Direct control of gas flow and mixture ratios must be achieved and monitored, while the introduction of trace concentrations of analyte gas to the reaction chamber must be accurately monitored in order to understand the sensor sensitivity and reaction kinetics. Finally, it is beneficial to design a system that can be easily modified to accommodate future experiments.

This testing system was designed to provide a straightforward method of characterizing metal oxide conductivity in the presence of trace amounts of gas. The system is flexible enough to allow the gas canisters to be readily exchanged and an alternate analyte gas to be used instead. Three gas canisters could simultaneously be connected to the system. Ultra pure (99.9999%) nitrogen and oxygen served as carrier gases for the analyte. The analyte gas consisted of 25 ppm trace in an ultra pure nitrogen background. Gas pressure regulators maintained a pressure of 60 psi in the line leading up to the mass flow controllers (MFC). Air present in the line prior to canister connection resulted in line contamination when gas cylinders were initially attached to the system and the 20 ft lines leading to the MFCs were pressurized. A vent valve was installed in each line immediately upstream of the MFCs. This allowed venting of each line to ensure it contained only uncontaminated gas from each canister.

3.2 Gases Under Investigation

Tungsten trioxide gas sensors have been shown to detect a variety of gases including hydrogen sulphide (H_2S) [4], Nitrogen Oxide (NO_x) [62, 76], Hydrogen (H_2) [55], and

Carbon Monoxide (CO).

Hydrogen sulphide is a lethal constituent in sour gas and is an ever present hazard in the oil field industry. While the World Health Organization has set community standards as low as 0.003 ppm [49] the Canadian Health and Safety Code puts the maximum short term exposure limit (STEL) levels at 15 ppm and the time weighted average concentration (TWA) at 10 ppm [77]. While minimum sensory chemical detection occurs at 0.13 ppm, rapid olfactory fatigue sets in at concentration $>$ 100 ppm. A sudden loss of consciousness without premonition, anxiety or cense of struggle sets in at 700 ppm, while a single inhalation above 1000 ppm may be rapidly fatal [78].

Nitrogen oxide is released from combustion exhaust generated by automotive transport and power generation and agricultural fertilization. Kurvits *et al.* report that NO_x is a major contributor and cause of smog [79]. Nordling *et al.* have shown that exposure to traffic pollution appears to influence development of airway disease and sensitization in preschool children [80]. Lindgren *et al.* have conducted a study to show that respiratory problems caused by NO_x pollution have not been limited to children but can be directly related to an increase in prevalence of diagnosis of asthma and chronic bronchitis in adults [81]. Nordling found that the mean environmental NO_x concentration that affected patients were exposed to was $23\mu g/m^3$ while the threshold concentration for NO_x induced illness in the Lindgren study was $19\mu g/m^3$. Considering that at standard temperature and pressure the density of NO_x is $1912g/m^3$, a baseline detection limit for functional NO_x sensors is between 9 and 12 parts per billion.

3.3 General Setup

Only three gases were required for testing (N_2, O_2, and the analyte gas) but four MFCs were used to regulate continuous and accurate gas flow through the testing chamber. Analyte gas was introduced into a gas line, depicted as the rightmost line in Figure 3.1. Analyte gas flow was balanced with nitrogen flow in the leftmost line. This provided an uncontaminated synthetic air supply and ensured that the gas flow rate over the sensor would not vary when switching from clean synthetic air to air containing the desired analyte. An 80%:20% nitrogen to oxygen mixture was used as a carrier gas and was split equally into both the

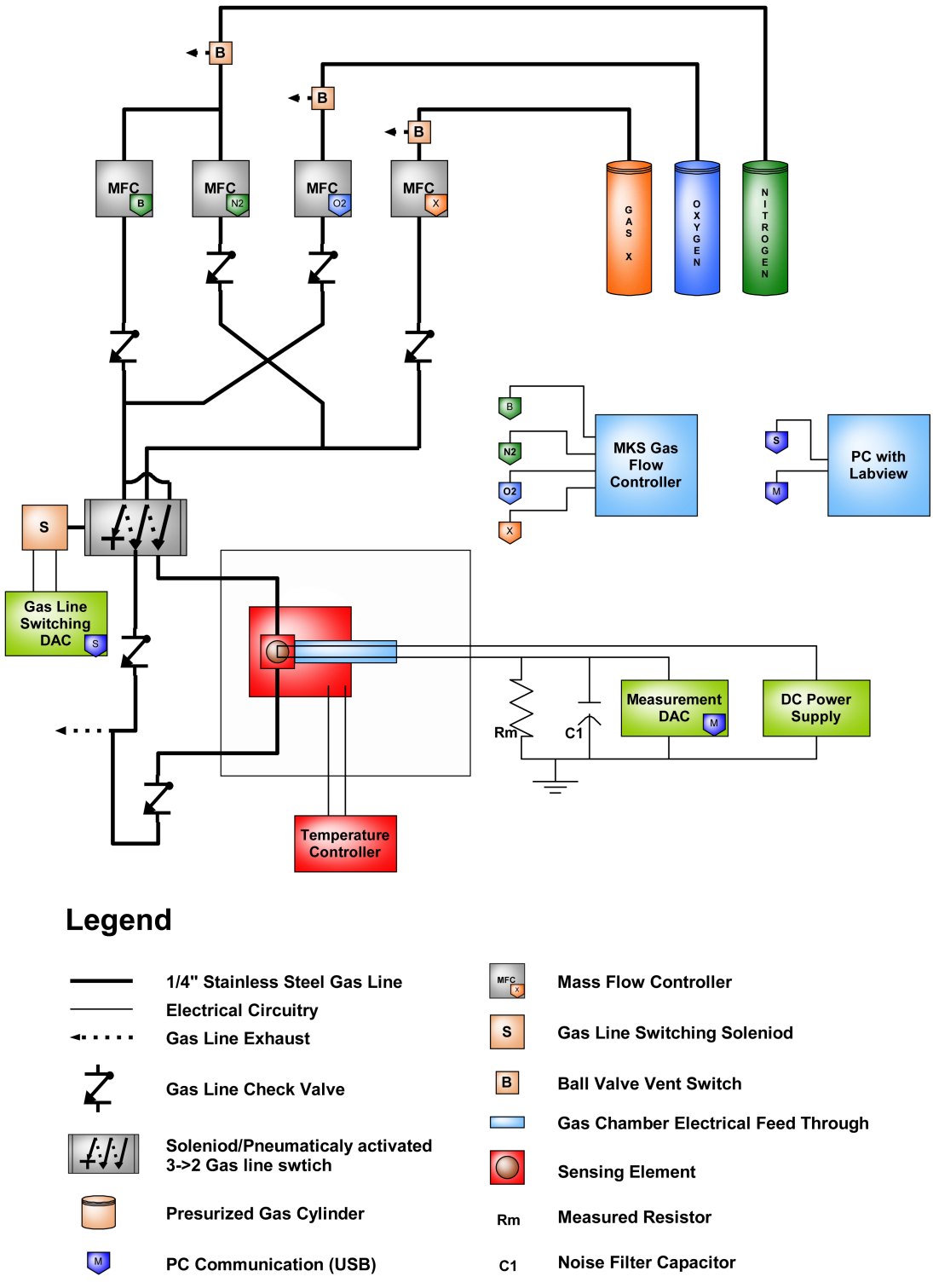

Figure 3.1: Schematic of the gas sensor testing system.

analyte gas line as well as the balance nitrogen line.

A 3:2 gas line switching mechanism was used to control whether the analyte gas mixture or the balance synthetic air mixture would flow into the chamber. The line switch is a pneumatically activated switch, with the switching mechanism activated by air pressure applied to an internal piston which is returned to its original position with a coil spring. A computer controlled solenoid was used to control air pressure to the gas line switch, enabling line switching at predefined intervals. Controlled gas flow rate over the sensor, combined with gas ratio and chamber temperature control, ensured accurate control over experimental variables.

3.4 Reaction Chamber

The reaction chamber is a contained volume where analyte gases are introduced to interact with a metal oxide sensor. Environmental conditions in such a chamber must be precisely regulated to maintain control of reaction variables.

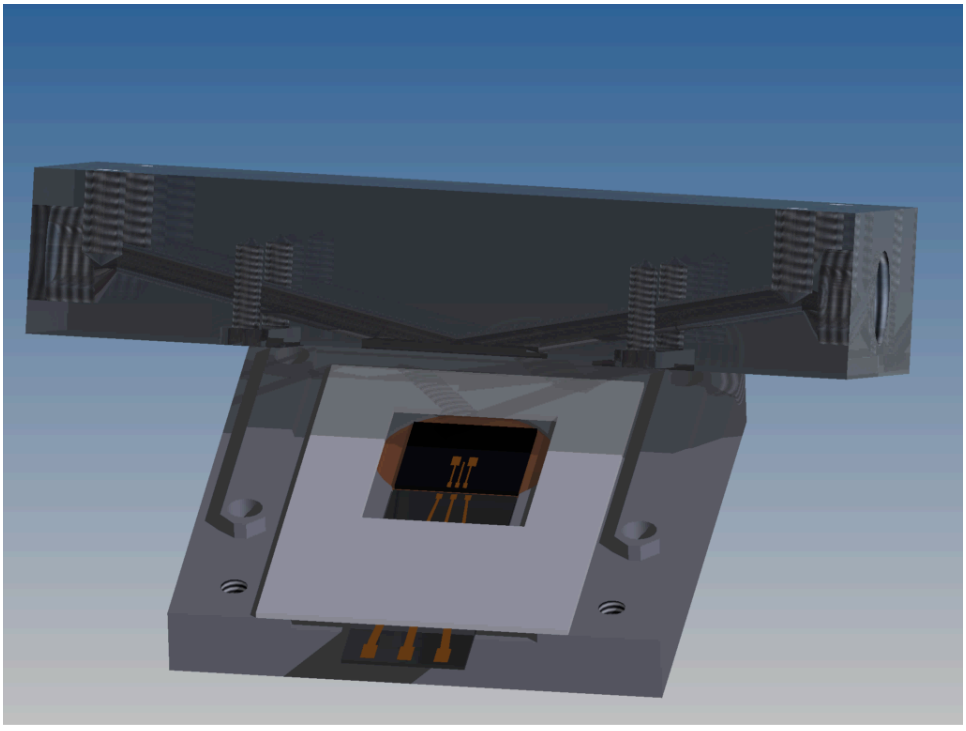

Figure 3.2: A computer generated view of the open reaction chamber. When the chamber is closed gas is contained to the volume immediately surrounding the sensing chip.

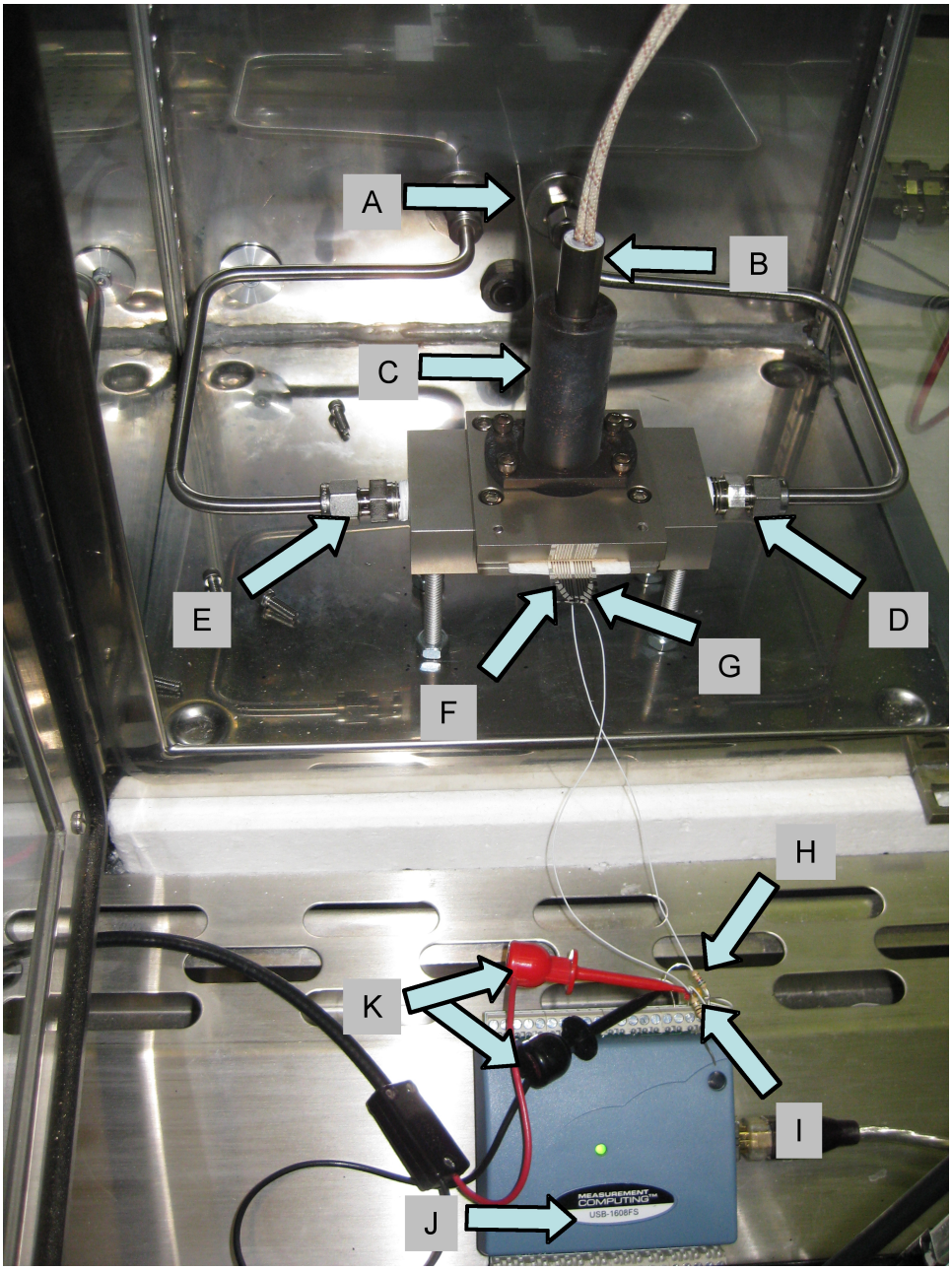

Figure 3.3: An image of the gas testing setup shows the chamber, temperature control mechanism, as well as the electrical feedthrough and measurement setup. Type K thermocouple (A) entering the back of the containment box. This, combined with the heater cartridge (B), forms a closed loop temperature feed back system. The thermocouple inserts into (C) the top of the gas chamber. Gas flows into the chamber via the gas inlet (D) and exhaust is vented to the back of the fume hood via (E). The electrical feedthrough (F) is connected to the sensing chip. $R_{parallel}$ (G) provides a measurable resistance ceiling.The rest of the external circuit is comprised of : $R_{measured}$ (H), C_{Lpf} (I), and the DC power supply (J). The voltage drop across $R_{measured}$ is monitored with the USB 1608FS data acquisition module (K)

Practical applications of gas sensors demand the ability to immediately detect the presence or absence of an analyte gas. A testing system used to monitor chemical sensing must have the capacity to quickly introduce and remove analyte gases from the chamber so that reaction times of the sensor can be assessed. While the actual reaction chamber volume was limited to approximately $1cm^3$, the distance between the gas line switch and the chamber was also minimized to decrease the dead space. This effectively reduced the transition time when introducing or removing a trace gas from the carrier gas flow.

Although minimizing the chamber volume is a critical step towards obtaining reliable and repeatable data, supporting circuitry leading into the chamber was configured in such a way that did not affect the temperature of the chip nor cause gas leaks into the chamber.

Detection setups often require the use of spring loaded contact pins, or wires soldered to the chip to facilitate data collection. When exposed to heat, conventional wire insulation may outgas, contaminating the system. These sources of contamination are eliminated by connecting the sensor to an air-tight electrical feedthrough which provides electrical access into the chamber. A lack of large wires running into and out of the chamber simplifies the chamber layout and results in a more easily operated system.

Within the chamber gas flow is incident on the chip at a 30 degree angle. This ensures that the sensor is immediately exposed to any changes in gas composition. Exhaust gases leaving the chamber are routed to the back of the fume hood via a 1/4 inch stainless steel gas line. Safe venting of the exhaust is a precautionary measure in case of future changes of the process gases even though analyte concentration is minimal and not a health hazard.

A primary function of the copper sample mount is heat conduction from the cylindrical heater cartridge to the sensor chip. This mount was sputtered with a thin film of titanium to prevent copper oxidation which could result in oxide flaking into the chamber. A 1/2 inch hole on the top of the sample mount provides a snug fit for the cylindrical cartridge heater. A 0.063 inch hole provides access for a 12 inch stainless steel sheathed type K thermocouple (Watlow Inc). Temperature was controlled by monitoring the sample mount temperature and adjusting the power driven through the heater with a feedback controller.

Bolts connecting the two halves of the testing chamber can be seen in Figure 3.3. These two parts of the system can be easily separated. This allows quick access to the

chip, feedthrough, and connecting wires. High temperature fabric padding surround the sensing chamber and provides a snug fit between the top and bottom of the chamber, while preventing gases external to the system leaking in. Thermally conductive paste is used to connect the sensor to the heater pad. This paste dries in less than 12 hours and can withstand temperatures up to $1200\,^{\circ}\mathrm{C}$. Chips can easily be removed from the substrate with minimal force and the thermal paste can be cleaned from the sensor with emery paper.

3.4.1 Controlled Variables

Gas Composition

Figure 3.1 depicts the gas canisters used for sensor testing. In order to approximate a real world scenario, analyte gases were tested while mixed with a synthetic air carrier gas flow. The carrier gas consisted of an ultra pure (99.9999%) mixture of 20% oxygen and 80% nitrogen. Initial characterization in a controlled environment is a crucial step in understanding reaction kinetics and gas sensor response characteristics. Analyte testing should eventually move away from ultra pure gases in order for the gas sensor to be viable for real world applications,

The gas delivery and testing system was configured in such a manner that if alternate gases were desired it is merely a matter of changing gas cylinders. Variation in gas concentration during testing is limited. A lower initial analyte concentration could be used if a concentration in the parts per billion range was desired.

Sensor Temperature

As mentioned in Chapter 1, sensitivity of semiconducting chemical sensors is directly related to sensor temperature.

Chip temperature was controlled with a Watlow EZ-Zone ST controller with a hybrid control switch. Power was applied to a 120V, 400W, FireRod heater while a type K thermocouple enabled closed loop control. The proportional-integral-derivative (PID) controller was set to ramp up to the desired temperature at a rate of $10\,^{\circ}\mathrm{C}$ per minute in order to avoid thermal stress affecting the sensor. Set point temperature was maintained within $\pm\,2\,^{\circ}\mathrm{C}$.

3.5 Data Recording

It was previously mentioned that semiconductor based chemical detection can be monitored through conductivity fluctuations in the sensing material as a result of sensor surface Red-Ox reactions. Multi-sensor comparative analysis requires accurate high resolution sensor monitoring. It was found that continuous accurate data collection could be achieved by mitigating the effects of several competing sources of high noise and device failure, as explained further on.

Electronic Signal Monitoring

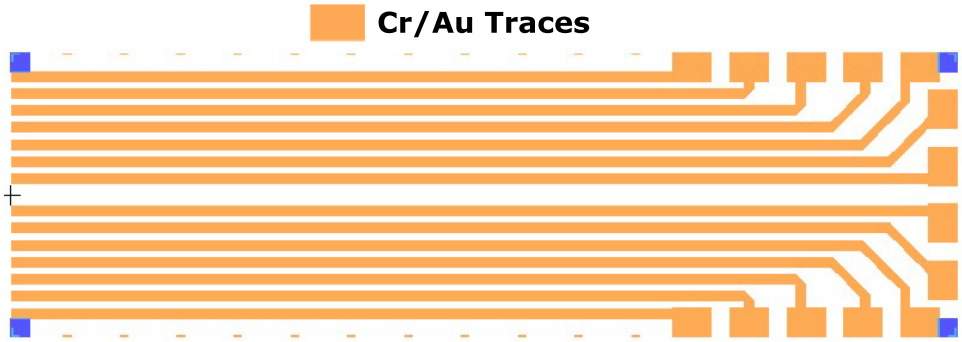

Figure 3.4: Schematic of the electric feedthrough pattern designed to carry electrical signals to and from chip.

Sensing elements were generally of the two electrode configuration. While sensor geometric simplicity offers clear advantages from a manufacturing viewpoint, such a configuration eliminates the possibility to accurately measure changes in electrical conductivity via a four point probe configuration. It was determined that conductivity of the resistive element could most easily be measured by placing a high tolerance external resistor in series with the sensor and then monitoring the voltage drop occurring across the resistor. This configuration allows a low reaction chamber volume, minimal temperature effects on supporting circuitry, low probability of contamination in the reaction chamber as well as the ability to easily vary the resistance of the external resistor to suit the power limitations of the sensor material.

Measurement Circuitry Design

The circuitry surrounding the chip consists of three main sections:

- Electrical Feedthrough
- External Components
- Signal Acquisition Hardware

The electronic feedthrough was designed to provide easy wiring access to the sensing element without compromising chip temperature or increasing chamber contamination. Compatibility and adaptability to various possible chip layouts were also factors during feedthrough fabrication process design.

Feedthrough design addressed the following criteria:

- Chemical Stability: Though expensive, gold was chosen as the primary conductive trace layer because of its combination of inert nature and high conductivity. Limiting chemical reactions to the sensor surface and avoiding chemical reactions involving the supporting electrical circuitry eliminates possible signal distortion due to alternate sources of voltage loss. Portions of the feedthrough may be subject to temperature exceeding $400\,^{\circ}\mathrm{C}$. It is therefore necessary to choose a material that will not be prone to oxidation in such an environment. Gold is also used during wire bonding from the sensor chip to the feedthrough.

- Thermal Isolation: In the interest of creating a feedthrough that remains thermally isolated from the chip, chamber design was such that it ensured the feedthrough did not make physical contact with the heater. A lack of physical contact ensured that the feedthrough could not act as a heat sink for the sensor chip. As seen in the process flow, Borofloat glass was used as a substrate. It maintained electrical isolation between traces as well as acceptable thermal isolation from the external environment. Thermal isolation ensured that external connecting wires were not affected by the heater, which at times remained at $400\,^{\circ}\mathrm{C}$ for extended periods of time.

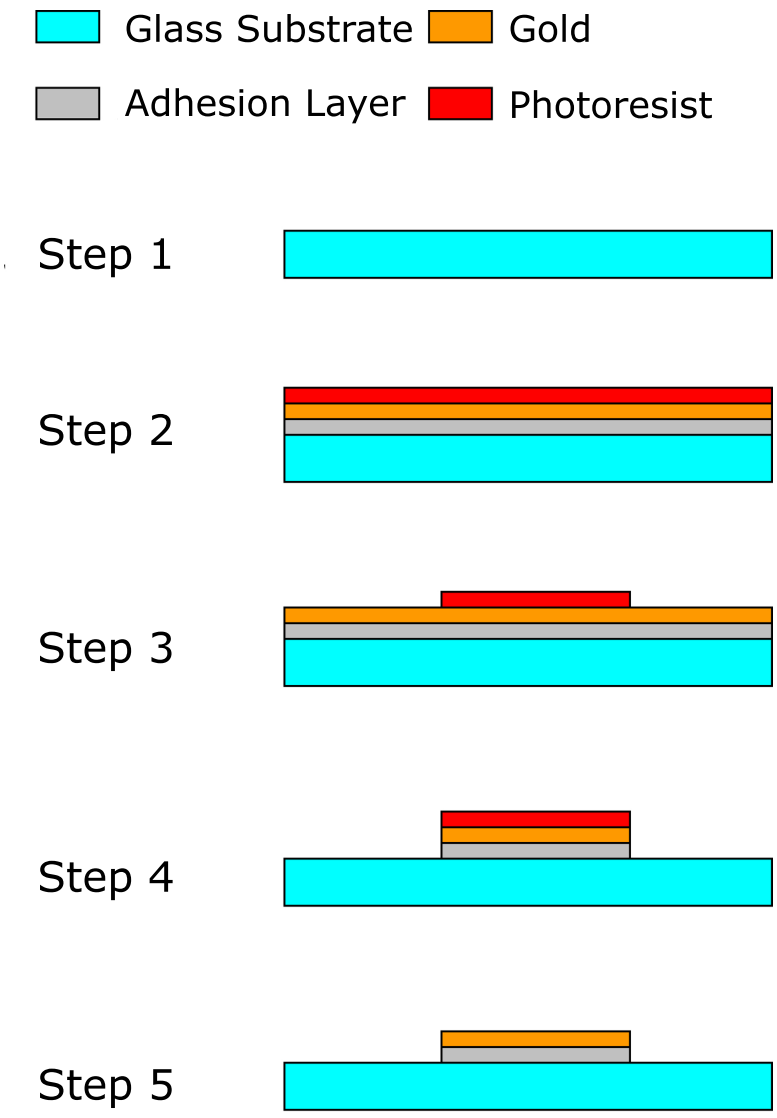

Figure 3.5: This schematic providing an overview of the feedthrough fabrication process flow.

- Functionality: The dimension of the feed-though was such that several trace pairs accessed the chip. Original chip design allowed for up to seven separate sensors to function simultaneously. The large surface area allowed ample room to vary trace widths in order to suit possible future applications. Enlarged bond pads ensured ample area to connect to the feedthrough using either wire bonding, conductive epoxy, or small alligator clamps.

- Wire Bonding: Although electrical connection was made using silver epoxy and gold wire bonding wire, 200 nm thick gold traces ensured that the alternative of wire bonding could be used to provide an easily adaptable manner to connect to bond pads on the sensor chip. Achieving a mechanically stable ohmic contact is easier when gold wire is wire bonded to a gold surface. Wire bonding with gold wire also creates a chemically inert connection. Removing epoxy or solder from the system avoids both impurity introduction due to epoxy and solder flux outgassing as well as changes in conductivity due to chemical reactions with analyte gases.

Low Signal To Noise Ratio

A DC voltage supply was used to provide a continuous DC signal across the series resistor circuit. It was initially noted that the measured signal was subject to large amounts of noise. This was a concern as detailed study of the output signal requires a clean signal, most notably at the instant an impurity is introduced or removed.

Unwanted signal distortion can be caused by power supply current spikes, noise generated from external sources such as lights or wall outlets, as well as ground drift due changes in power draw from equipment connected to a common outlet. Avoiding noise in the signal through the use of a low pass filter allows one to maintain a clean signal that can successfully be analyzed for minor variations in sensor response by removing abberations not attributable to changes in the sensor properties.

Low pass filters are based on the frequency dependant impedance characteristics of capacitors. A simple first order low pass filter can be constructed from a resistor in series with a capacitor, as seen in Figure 3.6. The cut-off frequency, which refers to the frequency at which the input signal is attenuated to -3 db, can be calculated by:

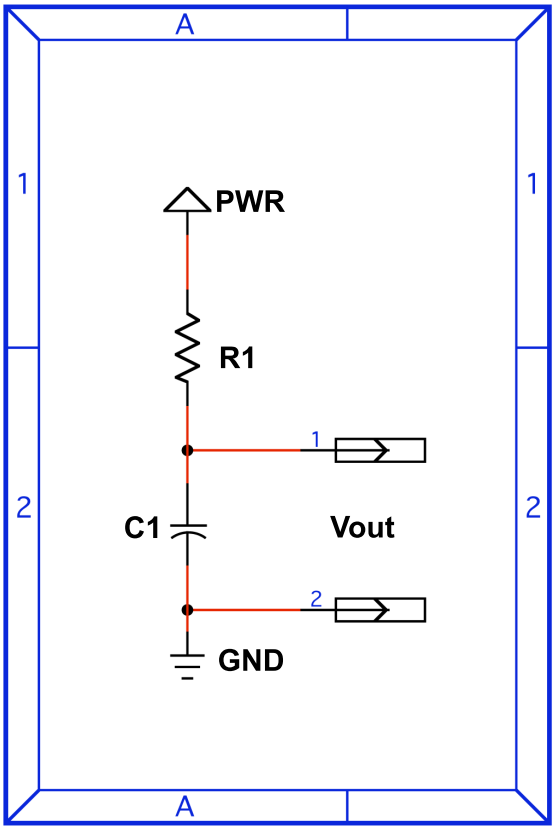

Figure 3.6: Schematic of a first order low pass filter circuit.

$$f_c = \frac{1}{2\pi RC} \tag{3.1}$$

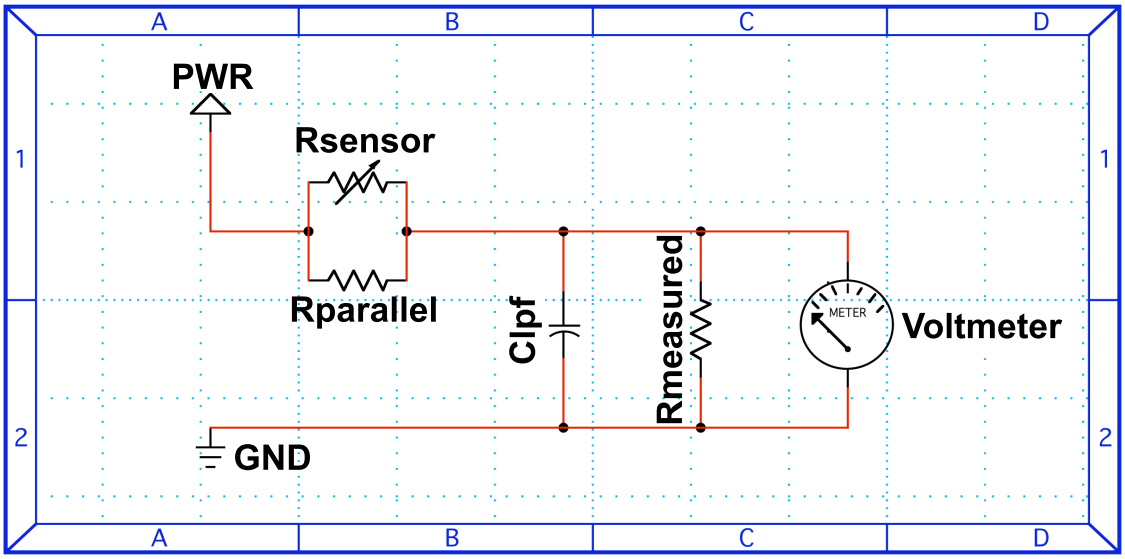

Figure 3.7: Schematic of the output voltage measurement circuit. Proportional voltage drop is recorded across $R_{measured}$ while C_Lpf is in place as a low pass filter.

Figure 3.7 shows the general detection circuit designed for this system. A constant DC voltage was supplied with an external power supply. Metal oxide gas sensors are often designed in a two contact point configuration in order to reduce fabrication complexity. Specialized equipment can be used to measure voltage drop across the sensor element while providing a specified current. A low cost alternative can be found in designing a series resistor circuit. The change in resistivity of the gas sensing element can be determined by measuring the relative voltage drop across a constant known resistance.

Metal oxide thin films often exhibit a large resistance when not subject to a reducing gas. $R_{parallel}$ was placed in parallel with the sensing element to provide a measurable circuit resistance in case the sensor resistance jumped into the tens of $M\Omega$ range. A typical value for the parallel resistor was usually around 9 $M\Omega$. The value of the external resistor was chosen so to provide a measurable proportion of the voltage drop while the sensor was either very insulating in addition to cases when it was quite conductive. This value was experimentally determined to be around 50 $k\Omega$.

Signal noise was found to increase when R_{sensor} was very large. This low signal to noise ratio is due to the high parallel resistance of R_{sensor} and $R_{parallel}$ in series with $R_{measured}$ causing very low current in the circuit. The low pass filter had to be designed such that the cut off frequency would be greater than the sampling rate to ensure accurate data collection while still acting as an effective filter when R_{sensor} became very low. In this case, R_{sensor} and $R_{parallel}$ provide the low pass filter characteristic resistance seen as $R1$ in Figure 3.6, while C_{Lpf} provides the acting capacitance. A suitable capacitor value can be determined by applying Equation (3.1) to the provided detection circuit design. As mentioned before, noise was found to be a problem only when current was low. When the value of R_{sensor} remains above $R_{measured}$, the filter would reduce noise contribution from signals greater than the cut off frequency. However, when the value of R_{sensor} drops below $R_{measured}$, the filter no long provides a low cut off frequency. Calculations to determine capacitor values were based on a 10Hz cutoff frequency and capacitor availability.

The optimal filter capacitor value can be calculated if isolated in the following equation:

$$f_c = \frac{1}{2\pi(R_{sensor}||R_{parallel})C_{Lpf}} \tag{3.2}$$

while the total low pass filter resistance can be calculated by:

$$R_{sensor}||R_{parallel} = \frac{R_{sensor}R_{parallel}}{R_{sensor} + R_{parallel}}. \tag{3.3}$$

.

A value for $R_{parallel}$ was determined experimentally. $R_{parallel}$ was chosen to maximize resolution of $V_{measured}$, where:

- R_{sensor} = 50 $k\Omega$
- $R_{parallel}$ = 9 $M\Omega$
- f_c = 10 Hz

C_{Lpf} was determined by combining Equations 3.2 and 3.3:

$$C_{Lpf} = \frac{1}{2\pi(\frac{R_{sensor}R_{parallel}}{R_{sensor}+R_{parallel}})f_c} = 32uF. \tag{3.4}$$

External Control Hardware and Software

LabVIEW is a National Instruments program designed for measurement and control applications. LabVIEW, in conjunction with two data acquisition modules (DAQ), provides three crucial and coordinated functions: voltage measurement, data acquisition, and gas line switching. Measurement Computing provides downloadable LabVIEW compatible programs for select modules. The combined use of several sample programs and slight modification to enable data recording, resulted in an overarching program which was able to perform the necessary functions.

A USB 1208FS DAQ was obtained from Measurement Computing. Specifications for this module can be obtained at http://www.measurementcomputing.com. This module was selected for its ability to perform both discrete signal sampling up to 10V as well as drive an analog output signal. It was later determined that these tasks could not be performed simultaneously. Higher resolution USB 1608FS DAQ was obtained for the purposes of data acquisition while the aforementioned 1280FS controlled gas line switching.

Prior to data collection a calibrating program (InstaCal) was run to ensure that DAQ baseline voltage levels were accurately determined and recorded. The Labview program could be set to measure the voltage drop across $R_{measured}$ at a 1Hz frequency and to switch the gas lines leading to the detection chamber at predefined intervals. A general approach to timing was to introduce the analyte gas for 5 minutes out of every 15. This allowed enough time to record both the rise and fall characteristics of the signal.

- Voltage Measurement: The USB 1608FS DAQ provides a 16 bit sampling resolution and a continuous sampling rate of up to 50 thousand samples per second. Although the lengthy nature of the tests limited manageable data rate to only 1 sample per second, the 16 bit resolution provided an input measurement accuracy of less than 3 mV.

- Data Recording: A simple LabVIEW function was used every count cycle to access and log the input voltage across up to 8 separate analog inputs.

- Gas Line Switching: Reliable sensor analysis requires precise control over not only the concentrations of gases flowing through the detection chamber but also accurate

knowledge of when gases are introduced and removed from said system. LabVIEW was used to directly control the testing system and coordinate switching with data acquisition.

3.6 LabVIEW Layout

Sequential steps performed by LabVIEW automatically records the voltage drop across resistor $R_{measured}$ while introducing and removing H_2S from the reaction chamber. Gas lines are switched from synthetic air (S.A.) to synthetic air with a trace amount of H_2S present at pre defined intervals, (when $t = t_g$). When the process is completed, the system self terminates and displays the results in graphical format.

Changes in film resistance had to be indirectly measured and recorded by analyzing the voltage drop across an external resistor. LabVIEW and a data acquisition module were used to record the voltage drop across $V_{measured}$ as a function of time. Simple LabVIEW "while" loops and "counter" VIs were provided by measurement computing. The counter was used to track time from test initiation until completion. A data logging tool was added to store $V_{measured}$ values, while an output graph was used to compile and plot the data.

Gas lines were initially manually switched from synthetic atmosphere to an H_2S containing gas flow. This was often somewhat imprecise. An additional DAQ was added to the system to allow for computer controlled gas line switching. A "while" loop allowed for predetermined switching times to be set, resulting in the ability to both control gas flow and measure resulting sensor reactions. Figure 3.8 gives a detailed flow diagram explaining the breakdown of steps in the computer controlled measurement and data acquisition system.

3.7 System testing

A metal oxide gas sensor was provided by Craig Jeffrey and Jim Tunney from the National Research Council of Canada Institute for Chemical Processing and Environmental Technology in order to characterize the gas testing system. The three objectives of characterizing this system were: to ensure analyte gas detection was possible and repeatable, to approximate how quickly analyte gas introduction into the chamber could

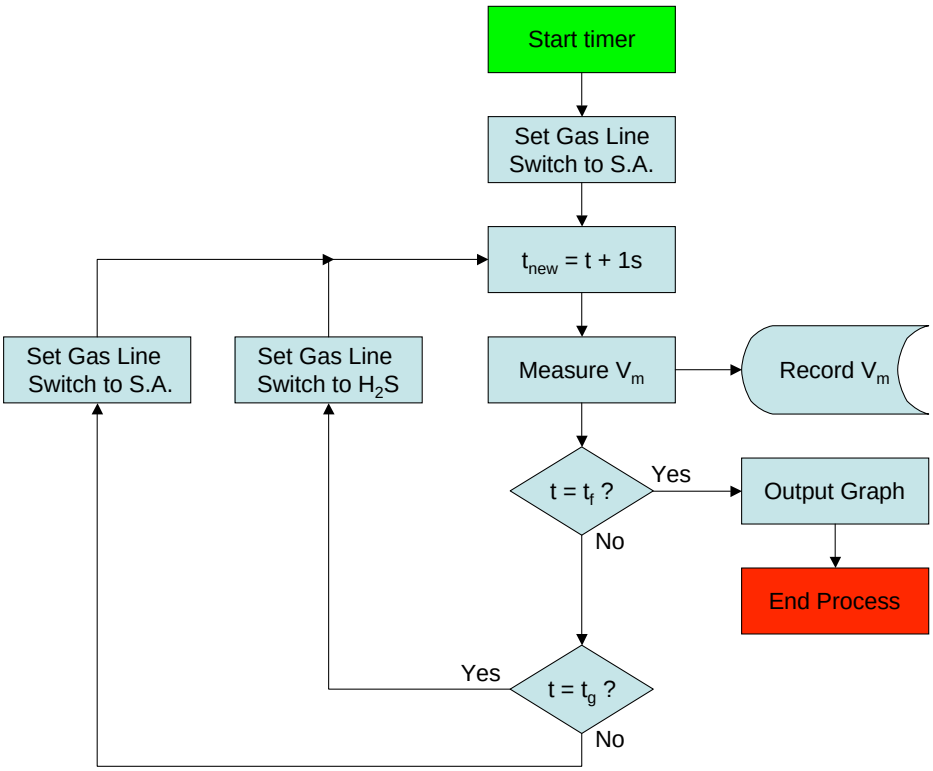

Figure 3.8: LabVIEW automatic measurement process flow.

be detected by a sensor, and to ensure that each subsystem could be controlled in a simple and dependable manner.

3.7.1 Testing Parameters

MFC Flow rate testing was performed using a DryCal DC-2 Flow Calibrator. Measurements were taken at 100%, 10%, and 1% of each MFCs maximum flow capability. Variation from the expected flow rate was taken into account when setting up experiments.

The highest concentration of H_2S available was 23.7 ppm in a pure nitrogen background. In order to obtain a test gas that was 20% O_2 and 80% N_2, the main N_2 carrier line was not used. O_2 was instead supplied to create the desired gas ratio in both the analyte gas line as well as the synthetic air balance line.

After an initial 5 minute stabilization period under a synthetic air flow, analyte gas was

introduced to the chamber for 5 minutes after which the flow would revert to synthetic air for 10 minutes. This cycle was repeated 5 times to monitor reaction stability. A flow rate of 100 sccm was selected and the individual MFC settings were calculated.

H_2S detection was performed at $150\,^{\circ}\mathrm{C}$, $200\,^{\circ}\mathrm{C}$ and $250\,^{\circ}\mathrm{C}$. Prior to each series of tests it was found that the sensor baseline resistance would vary considerably. As sensor temperature was increased, values for $R_{measured}$ were varied to compensate for the sensor resistance decrease.

3.7.2 Results

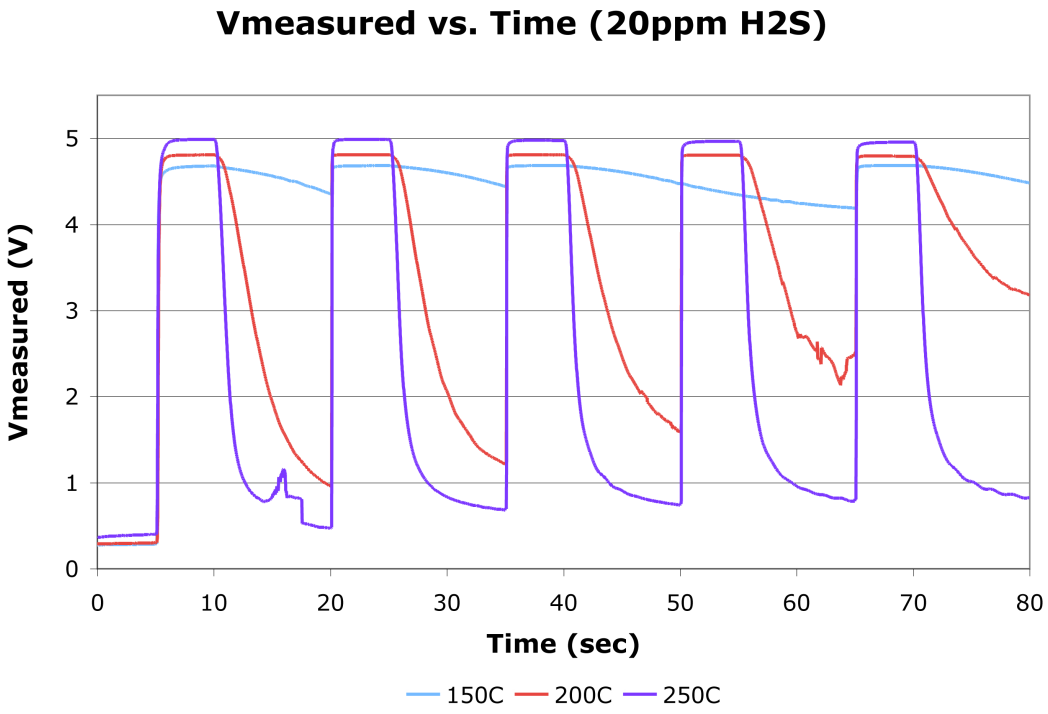

Figure 3.9: Overall graph of $V_{measured}$ vs. time obtained from 20 ppm H_2S at a flow rate of 100 sccm.

Several testing discrepancies occurred during chamber characterization. Despite having connected the negative terminal to ground, DC power supply voltage drifted over time. This drift was occasionally corrected by adjusting its output back to 5 V. Unfortunately this translated into noise seen after the first pulse during the $250\,^{\circ}\mathrm{C}$ test as well as after the fourth H_2S pulse in the $200\,^{\circ}\mathrm{C}$ test. Initial tests at $150\,^{\circ}\mathrm{C}$ did not introduce H_2S to

the chamber for the fourth pulse. The instructions to do so were simply missing from the LabVIEW program. The remaining pulses gave an accurate indication of how long it would take the sensor to revert to its initial state at such a low temperature.

Initial Response Speed

It takes time for the newly introduced gas to travel from the switching mechanism to the detection chamber. Below is a rough approximation of the time it would take after switching lines for the gas to first reach the chip. Several assumptions including negligible line pressure change and laminar flow are made in order to simplify these calculations. Gas velocity is a function of the volumetric flow rate (100 sccm) and the cross sectional gas line diameter (0.3175 cm).

$$v_{gas} = \frac{V}{A} = \frac{V}{\pi r^2} = \frac{100sccm}{\pi(0.3175)^2} = 315\frac{cm}{min} \tag{3.5}$$

This flow rate falls under the laminar flow regime. Approximately 30 cm of gas line runs between the gas line switch and the gas testing chamber. At 315 $\frac{cm}{min}$, the delay between when lines are switched and the new gas first enters the chamber was calculated to be 5.7 seconds.

Figure 3.10 illustrates both initial reaction time after line switching as well as measurement rise time. A marker has been placed at the 5 second point after switching for reference. It is apparent that chemical detection occurs immediately and the measured signal rises several orders of magnitude within 2 seconds after H_2S is introduced to the chamber. Although $V_{measured}$ only registered a small change at $150\,^{\circ}\mathrm{C}$, initial H_2S introduction into the chamber had a profound effect on the signal which can be seen in Figure 3.9.

A maximum tangential slope measurement was taken from the rise times of the first pulse. It was found that the sampling rate of one sample per second did not yield consistent results regarding the maximum slope of the rise time. It was however also found that a detection time of less that 2 seconds remained consistent after several runs.

The time it takes for a sensor to reach a baseline voltage after the analyte gas has been removed from the chamber is an indication of how well the sensor could function in a real

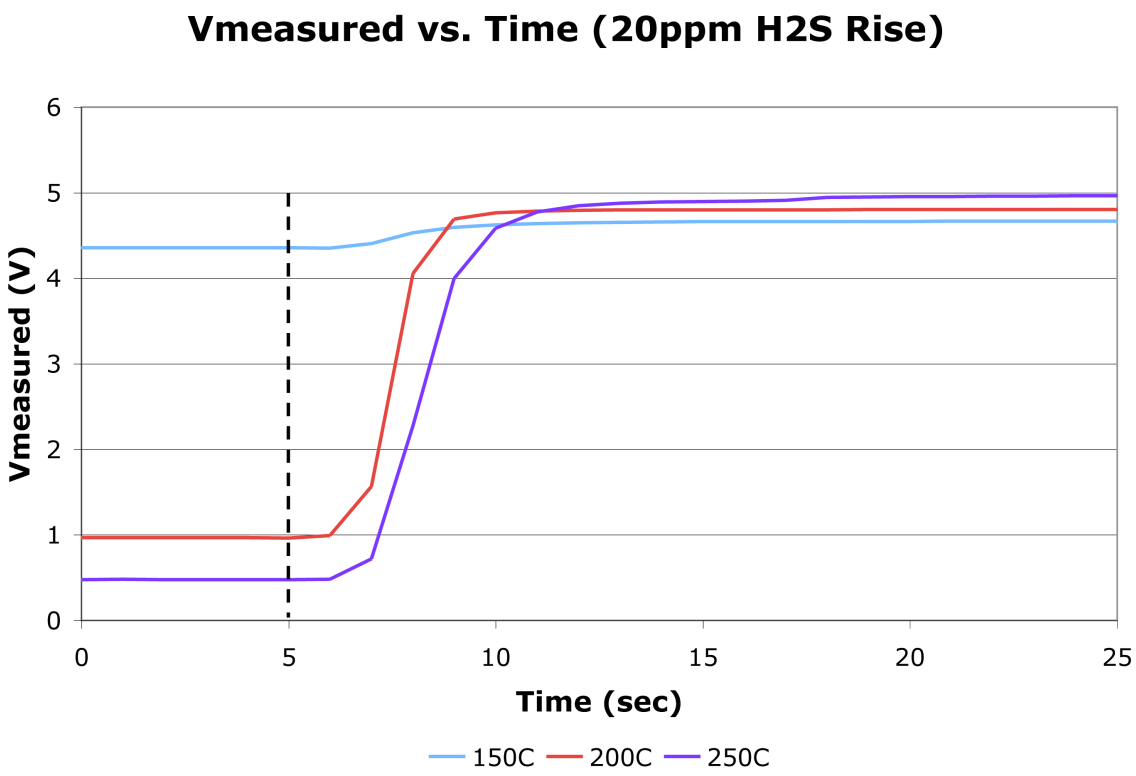

Figure 3.10: Graph of $V_{measured}$ rise time obtained from 20 ppm H_2S at a flow rate of 100 sccm. Data was obtained from the second H_2S pulse introduced into the system during the test shown in Figure 3.9.

world application. Controlling sensor temperature provides a method through which to balance gas adsorption and desorption rates. Figure 3.11 shows the effect that rising sensor temperature can have on its reaction kinetics.

Film R calculations

The following series of equations refer to Figure 3.7 and describes how the sensor resistance was calculated.

The total circuit resistance was first calculated by:

$$R_{s+p} = \frac{R_{sensor} R_{parallel}}{R_{sensor} + R_{parallel}} \tag{3.6}$$

and

$$R_{total} = R_{s+p} + R_{measured}. \tag{3.7}$$

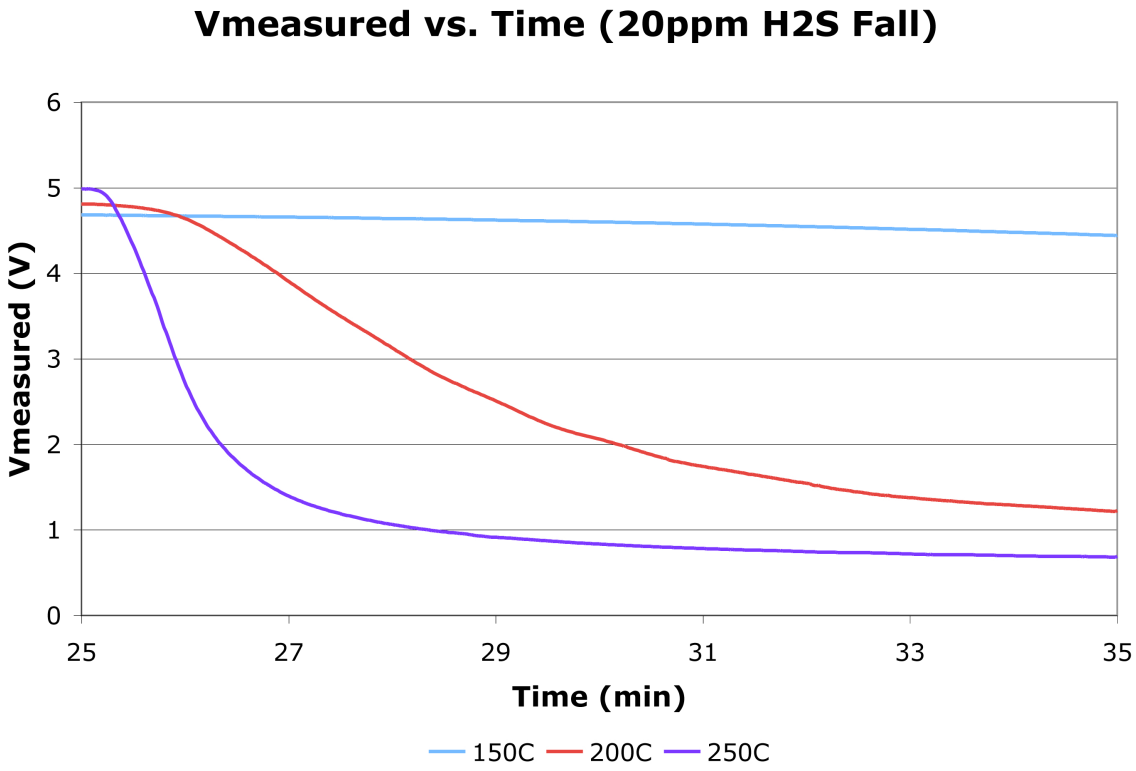

Figure 3.11: Graph of $V_{measured}$ fall time obtained from 20 ppm H_2S at a flow rate of 100 sccm. Data was obtained after the second H_2S pulse shown in Figure 3.9 was removed from the system.

Ohm's law was used to calculate the current through the system:

$$I_{total} = \frac{V_{in}}{R_{total}} = \frac{V_{measured}}{R_{measured}}. \tag{3.8}$$

The voltage drop across the sensor could be determined by modeling the system as a voltage divider circuit:

$$V_{s+p} = V_{total} - V_{measured} \tag{3.9}$$

Finally, R_{sensor} can be calculated using Ohm's law and the current and voltage drop across the sensing element:

$$R_{sensor} = \frac{V_{s+p}}{I_{sensor}} = \frac{V_{s+p}}{I_{total} - \left(\frac{V_{s+p}}{R_{parallel}}\right)} = \frac{(V_{total} - V_{measured})}{\left(\frac{V_{measured}}{R_{measured}}\right) - \left(\frac{V_{total} - V_{measured}}{R_{parallel}}\right)} \tag{3.10}$$

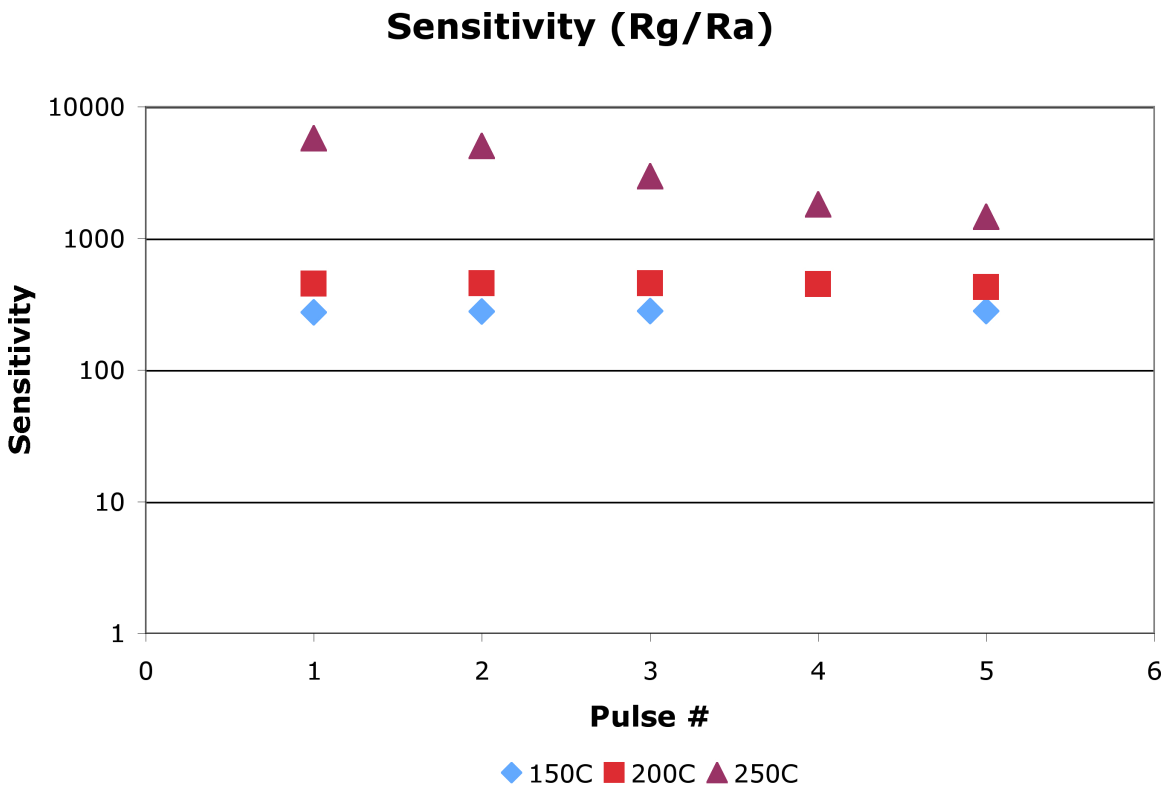

Figure 3.12: Graph of sensor sensitivity as a function of the number of gas pulses through the system.

The sensitivity of a metal oxide gas sensor refers to the change in resistance when the sensor detects an analyte gas versus its baseline resistance when exposed to air. In this case, 20 ppm H_2S in a synthetic air background is the analyte gas while baseline resistance measurements were taken while the sensor was simply exposed to synthetic air. Voltage values used for the calculations were obtained during the H_2S pulse segments. Figure 3.12 uses sensor resistance values given by the application of Equation 3.10. A slight drop in sensitivity is observed over time at $250\,^{\circ}\mathrm{C}$. The signals generated at sensor temperatures of $150\,^{\circ}\mathrm{C}$ and $200\,^{\circ}\mathrm{C}$ remain steady.

3.8 Conclusion

A complete gas sensor testing suite was designed and built to analyze the gas sensing response of a series of metal oxide based resistive elements through conductimetric analysis. Stainless steel gas lines and microflow meters allow for a variety of gases to

be directed onto the surface of a silicon based gas sensing chip at a wide range of instantly variable concentrations. Precise chip temperature control with sub $\pm 1^{\circ}\mathrm{C}$ drift is achieved with a back side mounted cartridge heater controlled in a closed loop configuration. The use of computer controlled gas line switching and voltage monitoring via LabVIEW allows for precise environmental control in the chamber during data acquisition. The functionality and ease of use of the entire gas detection testing system has been proved through the testing of metal oxide sensors in a low concentration H_2S environment.

4

Thin Film Sensor Fabrication and Testing

Fabricating devices requires in depth knowledge of each process step. Individual process steps may seem straightforward but each one must be compatible with previous and successive processing. This chapter gives a detailed account of tungsten trioxide growth, characterization, and micromachining related to thin film sensors and the supporting circuitry required for successful electrical monitoring. Successes and setbacks at each major fabrication point will be discussed.

4.1 Synthesis and Characterization of WO_3

Electrodeposition has traditionally offered an inexpensive and easily scalable thin film deposition method. Tungsten trioxide (WO_3) has been shown to detect gases such as hydrogen sulphide (H_2S), nitrogen oxide (NO_x) and carbon monoxide (CO). Several facile methods for tungsten trioxide electrodeposition have been developed [51–55]. Electrodeposited WO_3 is conventionally produced for its electrochromic properties. The following detailed process parameters outline investigation of a viable method for the creation of a tungsten trioxide resistive element from an electrodeposited thin film.

4.2 Electrodeposited WO_3

Meulenkamp *et al.* gives a detailed explanation of how to oxidize metallic tungsten powder, effectively forming a peroxytungstate complex [51]. Hydrogen peroxide in the presence of metallic tungsten powder oxidized the metal and acted as a complexing agent. The solution was then titrated to a pH of about 1.3 using either sulphuric or perchloric acid. Excess hydrogen peroxide was decomposed by solution agitation with a platinum or platinum-black electrode present. The equation governing peroxytungstate formation in an acidic solution is as follows:

$$2W + 10H_2O_2 \rightarrow W_2O_{11}^{2-} + 2H^+ + 9H_2O. \tag{4.1}$$

A major drawback of this solution preparation was decomposition time. WO_3 has been shown to precipitate spontaneously from the solution according to the following reaction:

$$W_2O_{11}^{2-} + 2H^+ \rightarrow 2WO_3 + 2O_2 + H_2O. \tag{4.2}$$

Pauporte *et al.* report an alternative solution preparation method that results in a solution which shows no signs of turbidity after being stored at room temperature for up to one week [52]. Post deposition inspection of the film appeared to show an intact continuous thin film of stoichiometric WO_3. To prepare this solution sodium tungstate powder (Na_2WO_4) was dissolved in ultra pure water. The use of sodium tungstate rather than the peroxytungstate complex increased the shelf life of the deposition solution. Hydrogen peroxide was added

to ensure complete oxidation of the tungsten ion and the pH of the solution was adjusted to around 1.2 with perchloric acid. Hydrogen peroxide served again to form the same deposition precursor. The interaction between WO_4^{2-} and H_2O_2 is described as follows:

$$WO_4^{2-} + 4H_2O_2 \rightarrow W_2O_{11}^{2-} + 2OH^- + 3H_2O. \tag{4.3}$$

Each preparation method will result in $W_2O_{11}^{2-}$ being present in the solution. In this form tungsten is shown to have a +VI oxidation state. WO_3 is deposited on the surface when a reducing potential is applied.

$$W_2O_{11}^{2-} + (2+x)H^+ + xe^- \rightarrow 2WO_3 + \frac{(2+x)}{2}H_2O + \frac{(8-x)}{4}O_2 \tag{4.4}$$

Pauporte *et al.* go on to show the chemical reaction behind the electrochromic effect of tungsten trioxide [52]. Tungsten trioxide has long been studied for its electrochromic properties. A dark blue color is achieved due to a cation intercalation/deintercalation shown here:

$$WO_3(bleach) + yX^+ + ye^- \rightleftharpoons XyWO_3(blue), \tag{4.5}$$

where X^+ is the $[H^+]$ in the sulphuric acid solution.

Pauporte *et al.* conclude that there is a pH and voltage range point which results in efficient WO_3 deposition and that the deposition is purely kinetically limited. They also state that there are several parasitic reactions that occur. These reactions include hydrogen evolution, polytungstate, free H_2O_2 and residual O_2 reduction, as well as WO_3 formation and all contribute to reduce deposition efficiency [52].

4.2.1 Deposition Solution

The long shelf life and smooth film achieved by Pauporte *et al.* appeared to be best suited to produce continuous WO_3 thin films. The suggested preparation method is as follows [52]:

12.5 mM to 25 mM sodium tungstate (Na_2WO_4) was dissolved in ultra pure water. Hydrogen peroxide was added to Na_2WO_4 at a molar ratio ranging from 1 to 4. Perchloric

acid was subsequently used to reduce the pH of the solution to approximately 1.2.

The deposition solution used for this project was based on data provided by Pauporte *et al.* as well as safety factors in place in the lab. Their experimental data showed high deposition efficiency and growth rate when the molar ratio of Na_2WO_4 to H_2O_2 was approximately 1. For safety reasons it was determined that sulphuric acid could be used as an alternative to perchloric acid to lower the pH.

A number of simultaneous reactions occurred in the solution. Controlling the WO_3 deposition rate and film thickness proved difficult. Solution degradation often occurred within 20 to 30 minutes This left a very small window during which deposition could be reliably controlled. Film thickness was also a major concern. Although continuous films were created with thicknesses as low as 50 nm, these films could not support themselves when fabricated into suspended resistive elements. The following sections provide insight into specific experiments that were performed to determine suitable deposition parameters.

Solution Stability Dependance on pH

Initial deposition tests made it clear that the solution lifetime was much shorter than previously expected. Turbidity was observed after approximately 30 minutes, with WO_3 precipitation occurring within an hour. It was experimentally observed that pH played a significant role in the rate of solution degradation. Quick tests were performed to determine a rough link between pH and solution stability. A 100 mM Na_2WO_4 solution was prepared by mixing the salt with MilliQ water. 40 mL H_2O_2 was added to the solution and stirred for 10 minutes to allow the previously discussed reaction between the tungstate ion and hydrogen peroxide to occur.

In two separate tests, H_2SO_4 and HCl were both gradually added to the previously prepared solution. A pH meter measured the acidity of the solution. Samples of the solution were removed and stored in clear glass bottles at various pH levels. These samples were obtained between pH of 2.4 and 1.2 with each sample decreasing in pH by a decrement of 0.2.

Turbidity was noticed in the solution almost immediately after reaching a pH of approximately 1.2. Photographs of the bottles were taken every 5 minutes. It was noticed

that solutions with a pH of at least 1.8 remained without precipitate indefinitely, while solutions with a lower pH showed signs of aging after anywhere between 10 minutes to an hour.

Electroplating Dependance on pH

As seen described in Equation 4.4, WO_3 deposition is dependant on the $[H^+]$ in the solution. Tests were performed to determine the upper limit at which WO_3 deposition could occur. A gold cathode was produced by sputtering a chromium adhesion layer and a 200 nm gold capping layer over a silicon wafer with thermally grown oxide. The anode used was the traditionally prepared thermal oxide covered silicon piece with 200 nm platinum sputtered on its surface over a titanium adhesion layer.

A Na_2WO_4/H_2O_2 solution was prepared in high purity MilliQ water. A pH meter was used to measure the acidity of the solution as H_2SO_4 was titrated in to reduce the pH. Electrodeposition was attempted at pH intervals of 0.5, ranging from a pH of 4 down to 1.5. It was noticed that the pale initially yellow sodium tungstate solution would turn a dark blue at the cathode at pH values greater than 2.0. This was indicative of the electrochromic properties of the material outlined by equation 4.5. This suggested that although a reduction reaction was taking place, the reaction did not have sufficient deposition efficiency to produce a film. Turbidity was not initially visible in the solution prior to deposition at these higher pH levels. Dark blue color would spread to the whole solution over time. When the system was turned off the color of the solution would slowly revert to a pale yellow but would contain significant amounts of WO_3 precipitate.

The deposition solution would quickly show signs of aging when the pH was reduced below 1.8. It was found that a WO_3 film could be produced at a pH of about 1.8. The film would be dark blue in color when initially deposited. This indicates that hydrogen intercalation had taken place. This is a reversible reaction and the film coloration would revert to its optically transparent nature if an external voltage was not applied for approximately one minute.

4.2.2 Characterization

Thorough process characterization constitutes a crucial step during fabrication. Topographical information produced by Scanning Electron Microscopy (SEM) provides a detailed account of device structure while X-Ray Photoelectron Spectroscopy (XPS) enables analysis of the material bonding structure and oxidation state. SEM is commonly used to analyze approximate physical attributes of materials and structures including film continuity, device shape, and device size. XPS was used to verify both the presence of WO_3 as well as its oxidation state.

Film Stress

WO_3 annealing has been studied via X-ray diffraction spectroscopy (XRD) and tunneling electron microscopy (TEM) to analyze changes in material morphology [53, 82]. Major changes in microstructure, from hexagonal at room temperature, tetragonal at $250\,^{\circ}\mathrm{C}$, and orthorhombic at $500\,^{\circ}\mathrm{C}$ have been found to occur. Interestingly, this was accompanied by structural changes ranging from nanoparticle to nanoplatelet and nanowire formation.

Tungsten trioxide film deposition initially generated white flaky thin films. It was observed through SEM that film continuity was dependant on film thickness. As seen in Figure 4.1, films with a thickness $>\sim$350 nm tend to exhibit cracking. It was also noticed that cracking nucleates at large clumps that form in the thicker films.

Tests were subsequently performed to determine a range of thickness within which films remained smooth and continuous.

Unreleased films less than approximately 300 nm thick tend to remain intact without cracking. It was determined that the films became destructively tensile when past a thickness of approximately 350 nm. It can be seen in Figure 4.2 that the film contracts resulting in broken film resembling puzzle pieces that fit together. When a literature search was performed to determine causes of the tensile film stress it was found that stress within electrodeposited WO_3 has generally been found to be compressive. Tests were performed to measure the stress in intact WO_3 films. Thin film stress was found to support literature and fall into the low single digit megapascal compressive range.

The effects of H^+ and Na^+ intercalation on thin film stress during WO_3

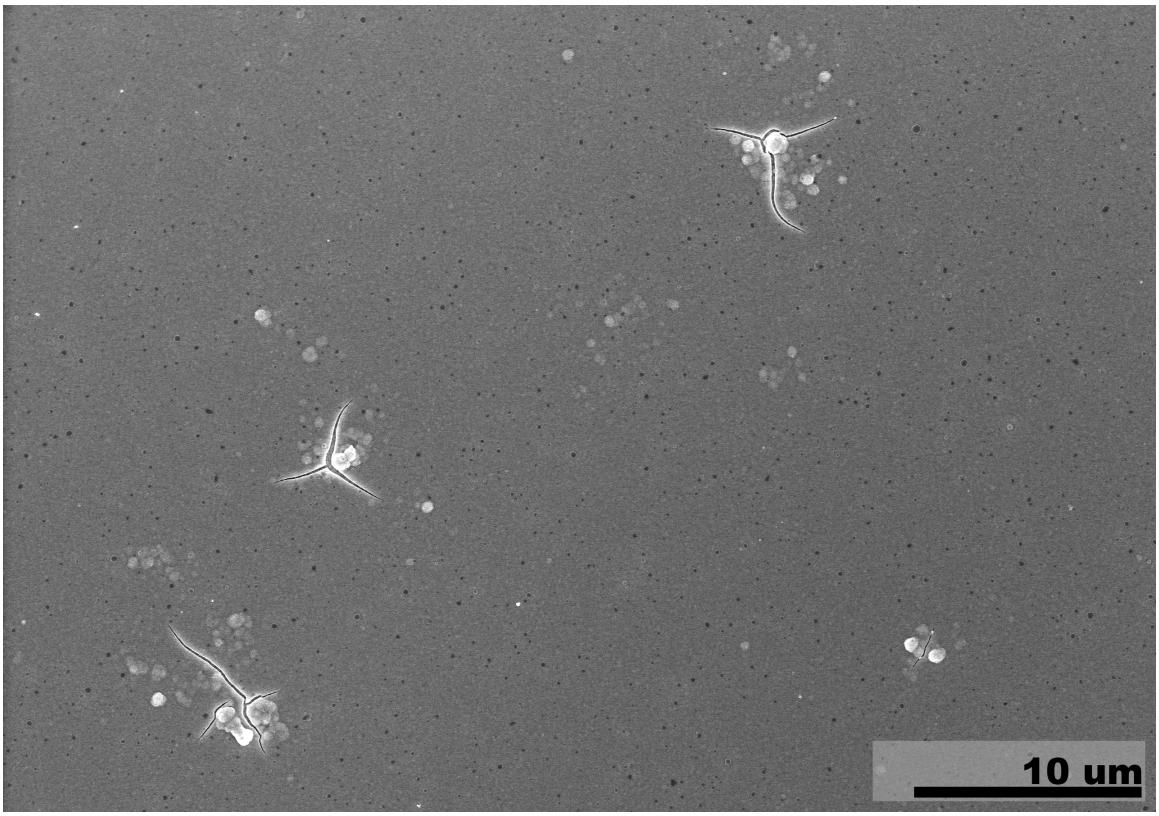

Figure 4.1: Scanning electron micrograph showing visible stress effects on a WO_3 thin film.

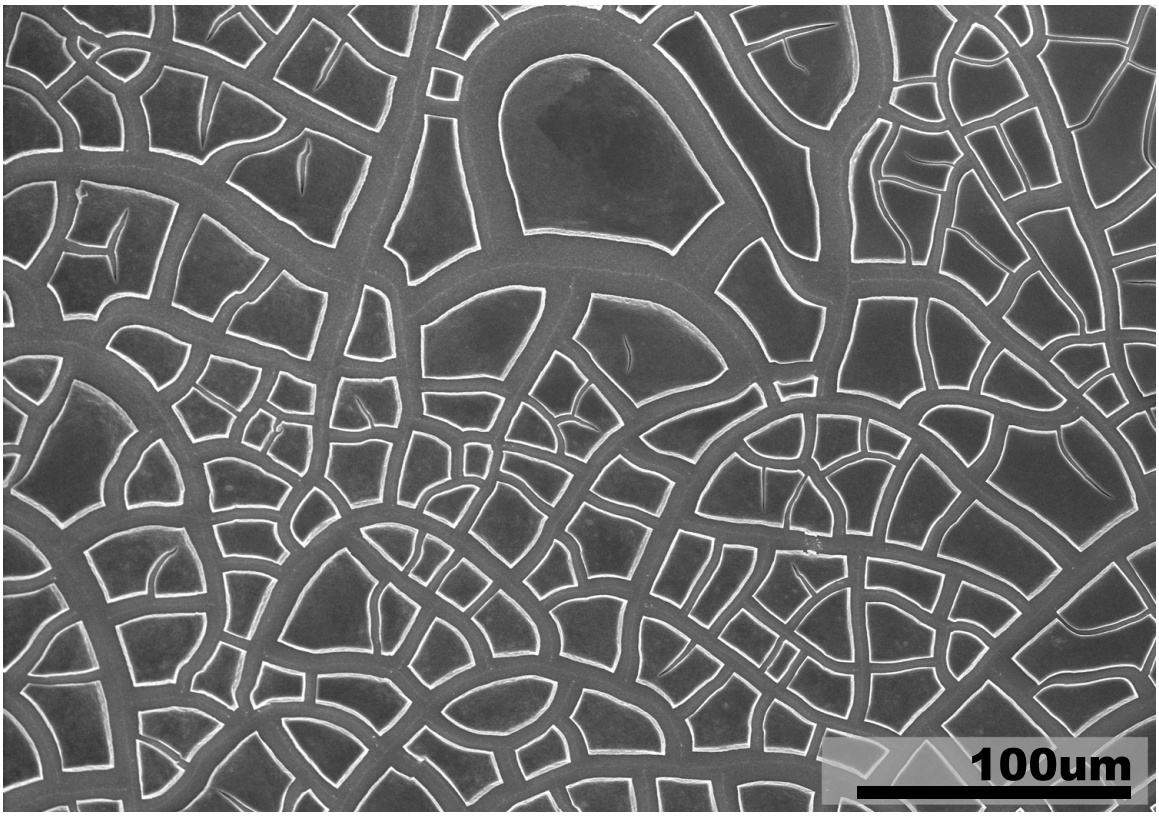

Figure 4.2: Scanning electron micrograph showing destructive cracking of a electrodeposited WO_3 film.

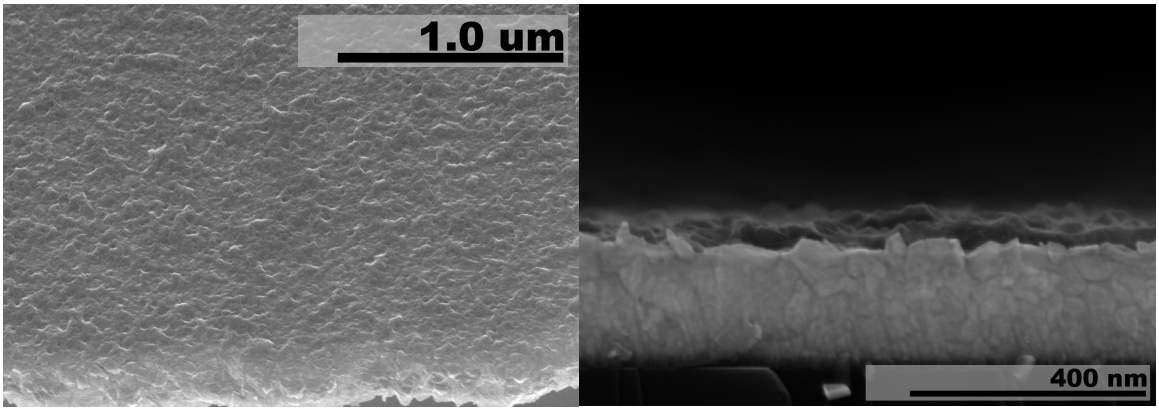

Figure 4.3: SEM image of a thin WO_3 film which has not formed a continuous film.

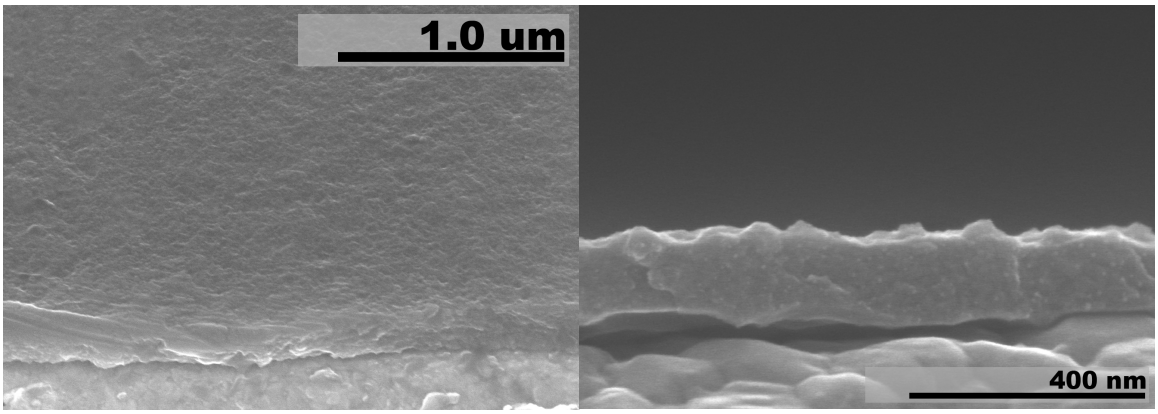

Figure 4.4: SEM image representative of films with a thickness between 100 nm and 300nm.

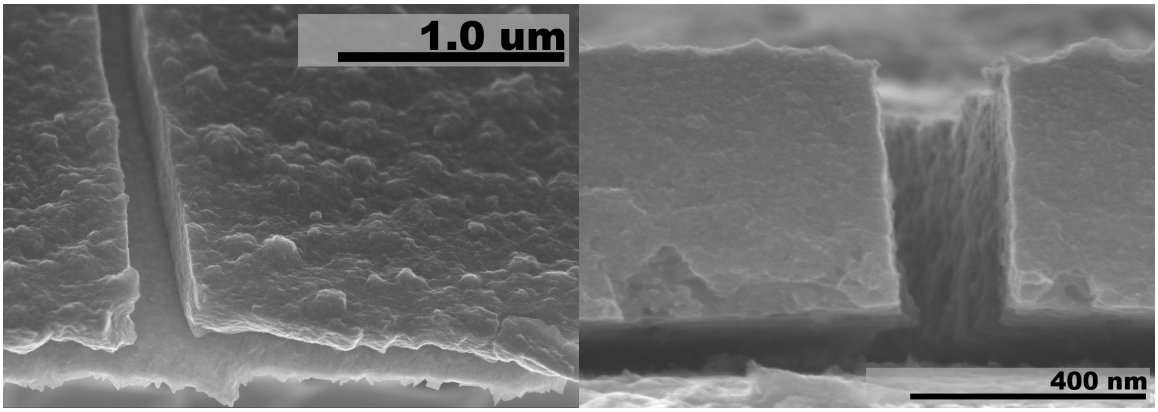

Figure 4.5: SEM image of a thick film where excessive tensile stress cause fracturing of the film.

electrodeposition has been studied [83, 84]. Stress due to ion intercalation was found to be compressive, while the intercalation/deintercalation reaction was found to be fully reversible, with minimal residual stress effects.

In contrast, similarly deposited films have been found to have a density which is 50% less than that of crystalline WO_3 and which contains up to 15% weight water molecules [85].

X-Ray Photoelectron Spectroscopy

X-Ray Photoelectron Spectroscopy is a method of analyzing the upper layer of a material. The XPS process is initiated by incident electrons with sufficient kinetic energy to ionize K(1s) shell electrons in the target material. The energy of the emitted core shell electron is measured. It is a function of the X-Ray beam energy ($h\nu$) and the binding of the electron in the K (1s) state [86]. The emitted photoelectrons have an energy that is a function of the difference between that of the incident X-Ray photons and that of the binding energy level of the ionized electrons [87]. The electron binding energy levels are characteristic of each element and the emitted photoelectron energy spectrum is also characteristic of each specific element. It is possible to deconvolute the often overlapping peaks to determine the oxidation states and their relative concentration in the film from the resulting XPS spectrum [88].

WO_3 thin films were analyzed to confirm deposition of tungsten trioxide. Films were analyzed as-is after deposition as well as after a one hour long open air anneal at temperatures ranging up to $500\,^{\circ}\mathrm{C}$. Temperature was limited to prevent any permanent changes in the WO_3 microstructure. It has been shown that as long as the temperature remains below $500\,^{\circ}\mathrm{C}$, the surface structure can be restored by heating in an oxygen environment [89]. Resulting XPS spectra were compared to the NIST X-ray Photoelectron Spectroscopy Database [90].

Figure 4.6 shows the WO_3 surface XPS spectra for tungsten binding energies. This data matches that found in literature [91] and the NIST database [90] for WO_3 and verifies that the surface of the oxide does not contain significant amounts of metallic tungsten. An argon plasma was used to sputter away the surface of the electrodeposited oxide in order to investigate the subsurface oxidation. Figures 4.7 and 4.8 show that the subsurface oxide

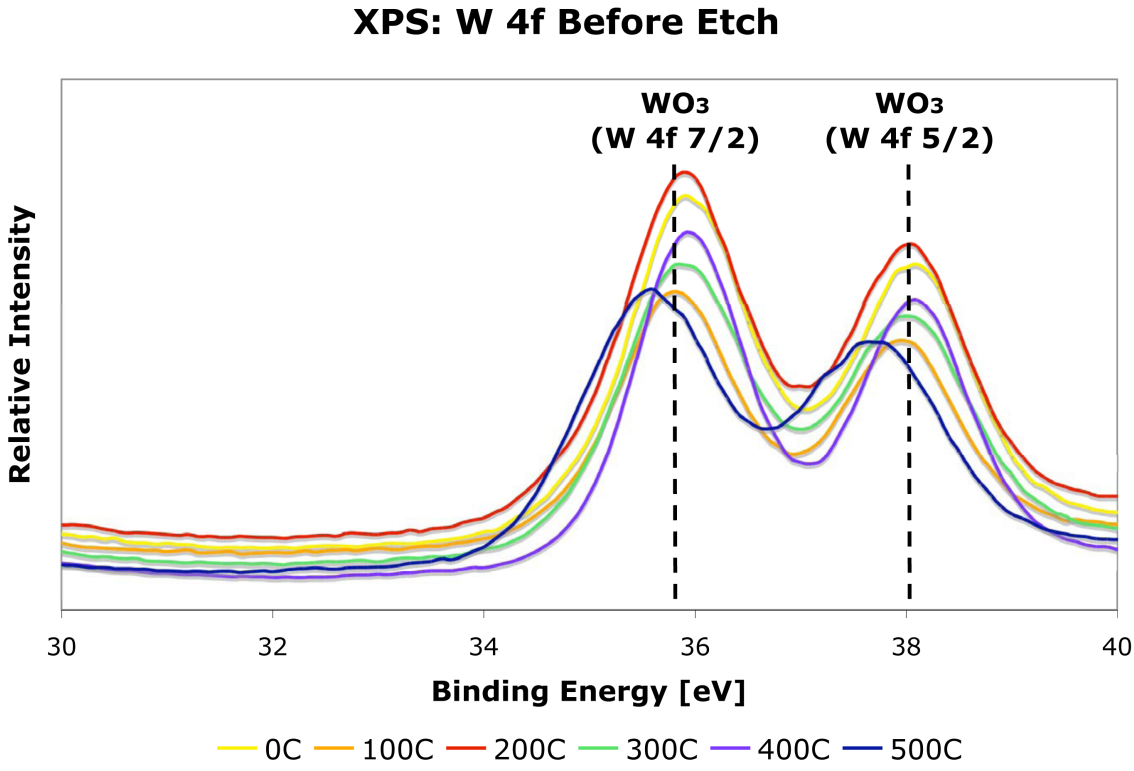

Figure 4.6: XPS measurement of WO_3 surface tungsten binding energy.

is not stoichiometric WO_3 but remains significantly oxidized. An increase in tungsten oxidation can also be seen in films that were annealed at higher temperatures.

4.3 Sensor Layout

Fabrication layout was designed to use the maximum space available on one silicon wafer. Figure 4.9 shows how each die was placed on the 4 inch wafer. Bars visible on the edges of the wafer allowed for pattern alignment to the crystal plane. Patterns with proper alignment and spacing could be easily separated into individual die.

Figure 4.10 is a close up image of one pattern. Two different layers can be seen. The outer traces are the patterns used for gold. Electrical contact through wire bonding could occur on the wide trace pads across the bottom edge of the die. The second layer pattern is visible as beams with large contact pads down the center of the chip. The fragile beams were located in the center of each die to minimize the chance of accidental physical contact with wafer tweezers and gloves during the fabrication process. A vertical series of

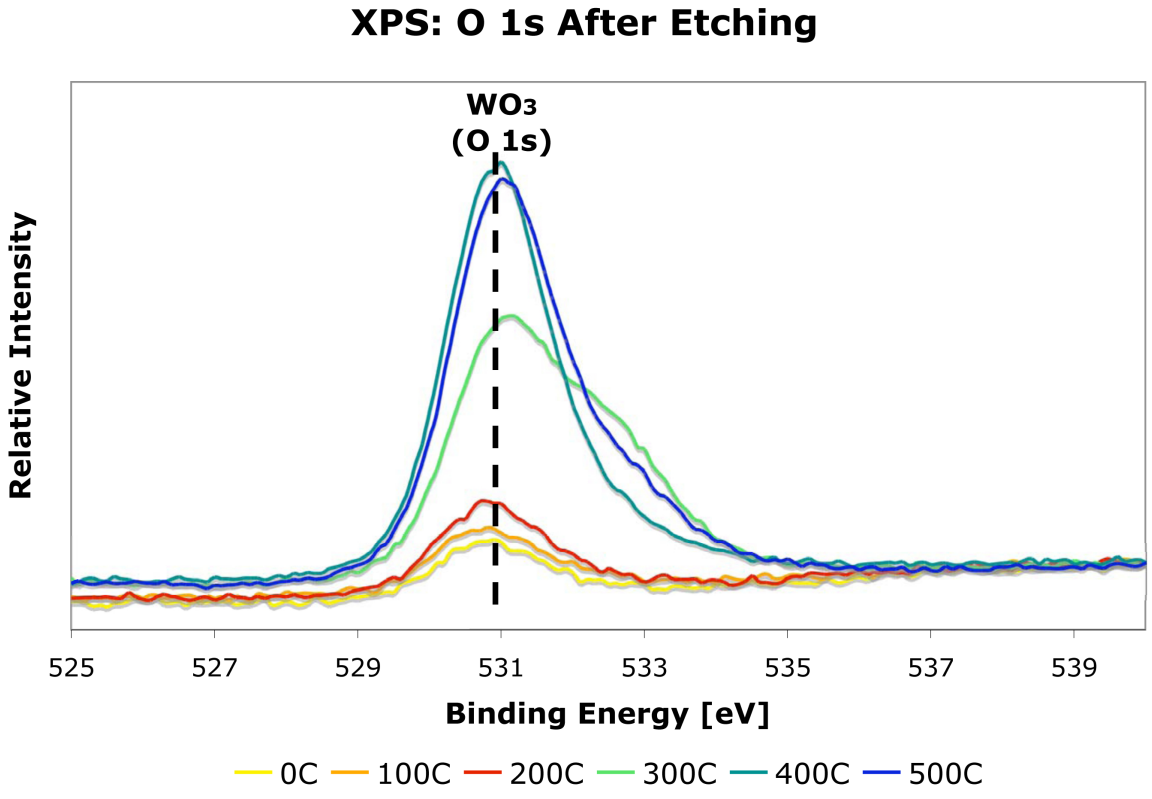

110

Figure 4.7: XPS measurement of O 1s binding energy after surface layer removal via sputtering.

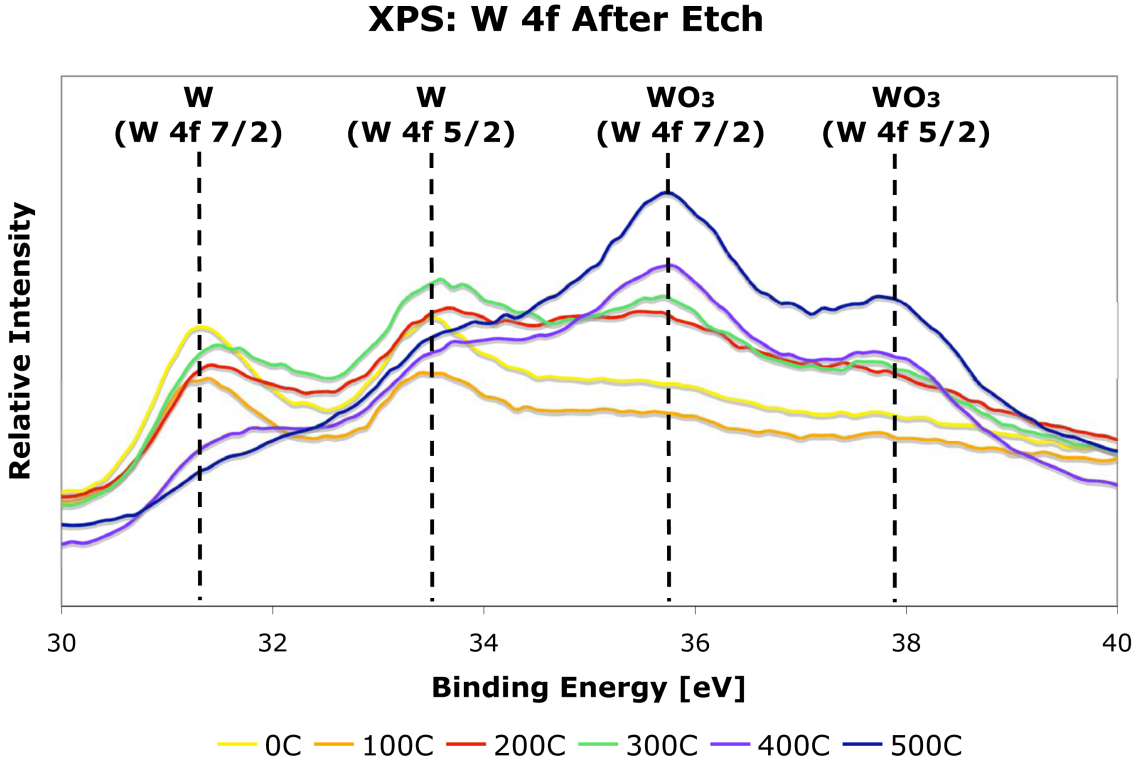

Figure 4.8: XPS measurement of W 4f binding energy after surface layer removal via sputtering.

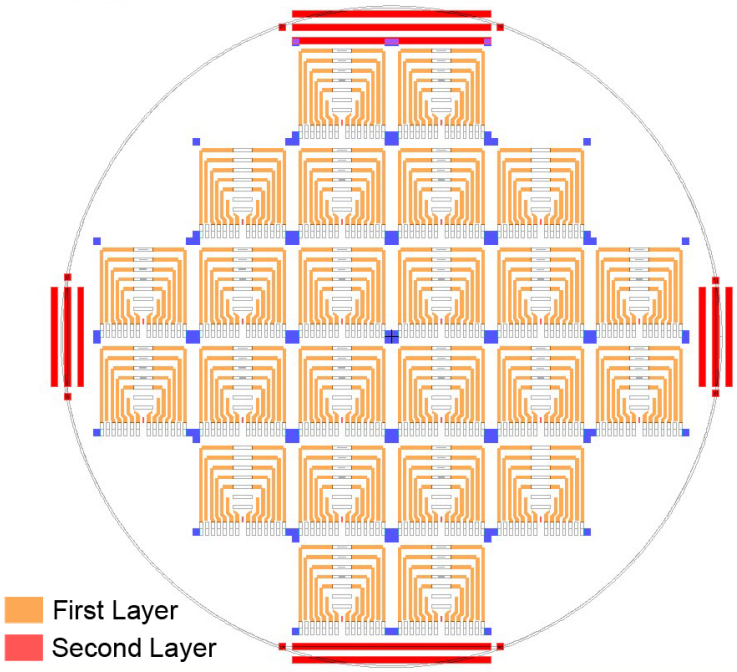

Figure 4.9: Overview of the WO_3 thin film sensor layout.

diminishing crosses can be seen at the lower end of the die. These were used to align the second layer pattern to the metal traces already fabricated on each chip.

4.4 Micro Sensor Fabrication

Process steps were based upon experiments discussed in previous sections, current review papers, and consultations with local microfabrication experts. The simplified process flow shown in Figure 4.11 provides a visual guide to the steps taken. Alternate options for each step will be discussed as well as their respective advantages and disadvantages.

Figure 4.11 shows alternate processing options at two separate stages. Processing has been designed to offer processing options that take into account chemical and material compatibility. This simplified process flow shows only chromium acting as both an adhesion layer for the gold as well as a seed layer for the WO_3 deposition. Additional metal layers may be placed between the Cr and the Au.

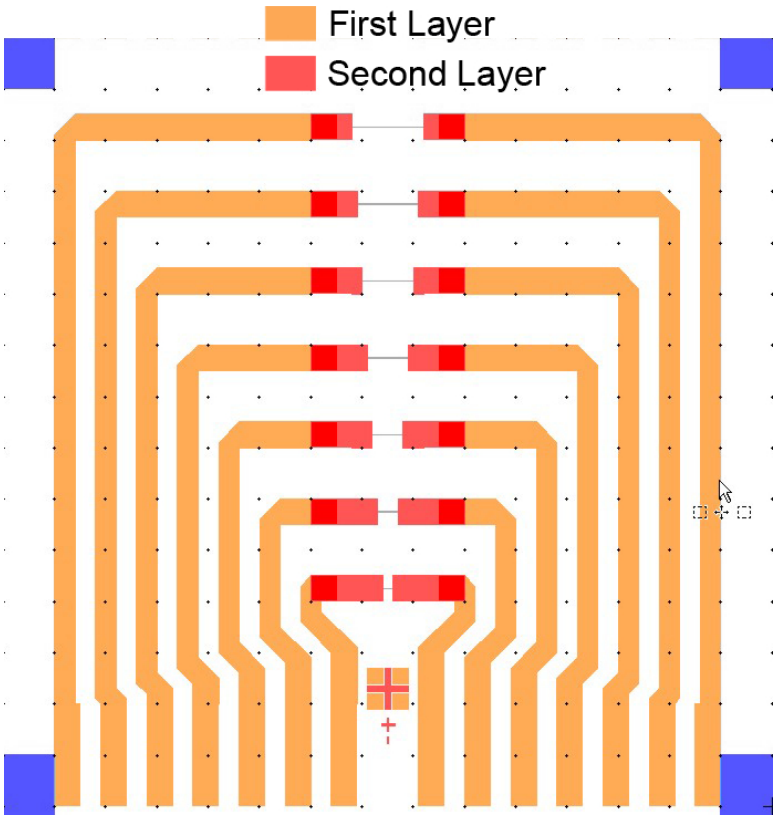

Figure 4.10: Layout of a single WO_3 thin film sensor.

Step 1: Substrate Preparation

Resistive based elements must be fabricated on an insulating substrate to ensure electrical isolation of individual components. Silicon dioxide is a suitable insulating material that is easily prepared through thermal oxidation of a standard silicon wafer. A $< 100 >$ silicon wafer with approximately 500 nm of thermally grown SiO_2 was used as an initial platform for sensor fabrication. The substrate was cleaned to avoid possible substrate contamination from decreasing yield. It is possible to remove organic contaminant that may be present on the surface of the wafer by submerging the substrate in Piranha, a 3:1 mixture of H_2SO_4 to H_2O_2, for at least 20 minutes. The substrate must then be rinsed thoroughly in high purity deionized water and dried with clean nitrogen gas. Both of these steps ensure a particulate free clean substrate on which to commence metallization. Substrates may be stored at this stage. It is recommended to continue with processing until metallization is complete before storing substrates to avoid surface particulate buildup.

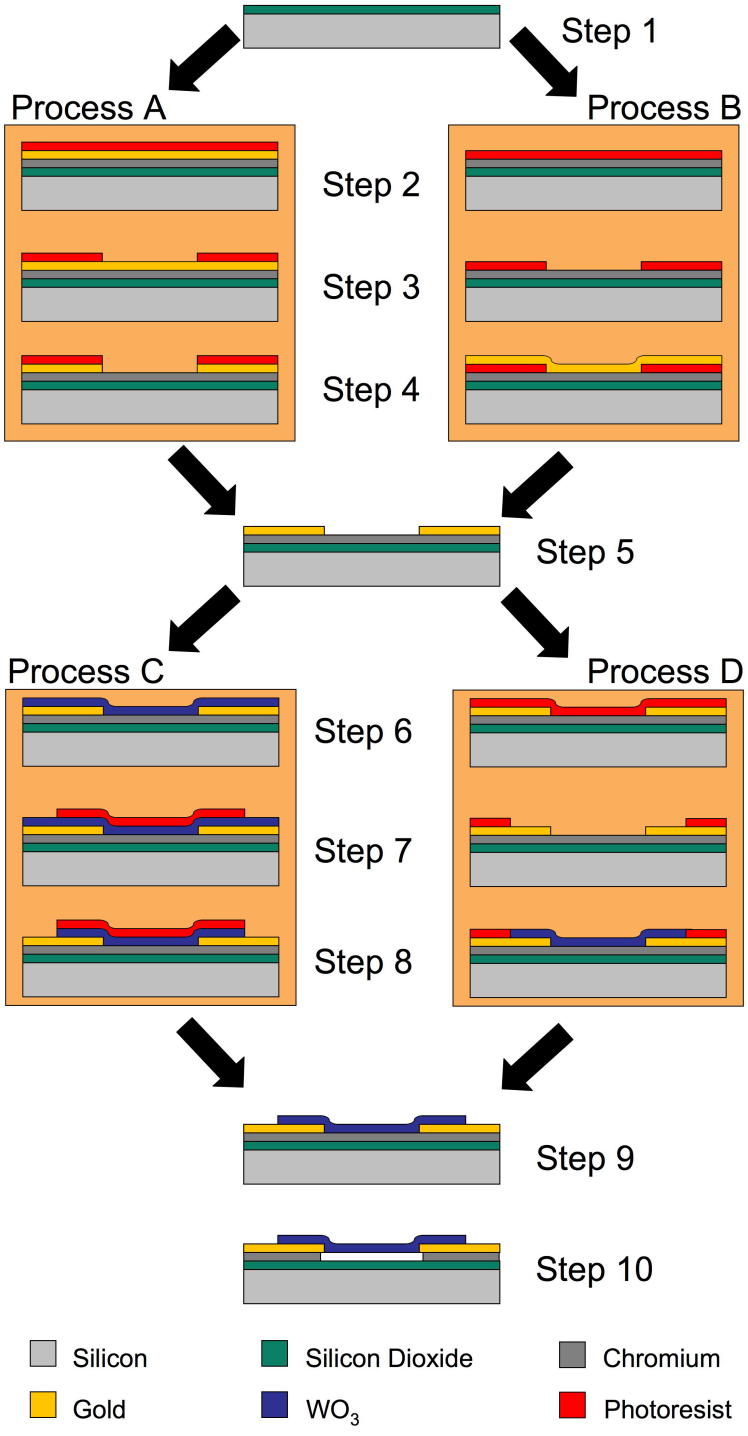

Figure 4.11: Schematic providing an overview of the WO_3 thin film sensor fabrication process flow.

Process A

Gold was used as a chemically inert metal layer from which to fabricate electrical traces. A low z metal layer is required between the substrate and subsequent metallization layers to ensure that it remains adhered to the substrate regardless of subsequent processing temperatures. Either chromium or titanium is generally used as an adhesion layer. In this case chromium is used due to the incompatibility between titanium etch and WO_3 during step 10 in the process.

- **Step 2A: Metallization and Lithography Preparation**

  Metallic layers were deposited sequentially using a 3 gun RF planar magnetron sputtering system.

  Step 2 of Figure 4.11 shows that chromium was sputtered on top of the cleaned Si/SiO_2 wafer. Gold was sputtered on top to protect certain areas from the chromium etch that occurs in step 10. Cr sputtering was conducted at 7 mTorr and 300 watts. Au does not oxidize as readily as most metals and is therefore only burned in for 1 minute. After this time the shutter was opened for 20 minutes to achieve a film thickness of about 200 nm. The power supply was then turned off and the substrate was cooled for 5 minutes before being exposed to atmosphere to avoid any film stress due to rapid temperature shifts.

- **Step 3A: Photolithography**

  HPR 504 photoresist patterning is accomplished through the standard parameters described in Chapter 2. A mask aligner is used to align the substrate to the mask pattern. HPR 504 exposure time was found to be approximately 1.9 seconds. The exposed resist was then removed by submerging the substrate in 354 developer for 17 seconds and rinsed in DI H_2O. At this point the resulting wafer contained a patterned resist layer on top of the electroplating seed layer.

- **Step 4A: Metal Etching**

  Pattern transfer usually relies on a patterned masking layer having a significantly slower etch rate for a given etchant than the material it covers. A patterned

photoresist etch mask will cover defined areas of the layers below it. This prevents the select areas from being affected while the rest of the surface is etched away. Two comprehensive resources were used to investigate etch compatibility. The CRC Handbook of Metal Etchant [65] was a valuable resource to determine etchant compatibility between a specific layer and the film underneath that would ultimately be exposed to the etchant as well. The second by Williams *et al.* is a resource aimed specifically at common materials and etchants used in the microfabrication industry [66]. It provides an in depth analysis of material etch rates relative to common processing parameters.

After photolithography gold etchant was used to remove the capping gold layer and define the conductive traces that would eventually be used to connect the chemical sensing metal oxide resistor to external circuitry. By removing the gold, the layer underneath is exposed to gold etch. It was critical that this layer was not affected by the gold etch as it would later serve as a conductive seed layer on which WO_3 was to be grown.

Gold etch typically consists of an aqueous mixture of iodine (I_2) and potassium iodide (KI). This etchant is dark in color which makes the etch endpoint difficult to analyze. Gold etch is an isotropic etchant. If the time it takes to etch through the gold layer is increased, significant over etching of the gold which would ultimately result in the complete removal of crucial features. Chromium was typically used as both an adhesion layer for the gold as well as a seed layer for subsequent WO_3 deposition. It is unaffected by gold etch and its etch does not affect the deposited and patterned WO_3.

The 200 nm sputtered gold layer was found to etch away in 1 minute and 30 seconds. Features were found to remain intact with minimal undercut. Upon removal from the etchant, the substrates were rinsed with DI H_2O and then placed in an acetone bath for 5 minutes. The DI H_2O rinse served to clean off the etchant from the wafer while the acetone bath removed the resist covering the remaining gold pattern. After the resist was removed, the substrate was rinsed in IPA and finally DI H_2O, then dried with clean N_2. The substrates were then stored in a contained environment which

protected them from contamination.

Process B

While Process A was developed as a straightforward method to pattern gold on metal layers compatible with gold etch, Process B enables the use of any metal layer under the gold. A "lift off" method was initially used to pattern the gold. This method eliminated the need for gold etch and is widely used to pattern layers whose etch is not compatible with specific structures or materials already present on the substrate.

The described metallization method allowed the deposition of a thick sacrificial seed layer of copper or silver. These materials were deposited on top of a thin chromium adhesion layer. The films were deposited to a thickness greater than 1 μm to avoid stiction.

- **Step 2B: Metallization**

  A cleaned substrate was loaded into a 3 gun magnetron sputtering system. An adhesion layer of chromium was first sputtered to prevent delamination of subsequent layers. This was followed by the deposition of a relatively thick sacrificial seed layer, usually consisting of either copper or silver. The sacrificial seed layer materials were chosen simply by material availability and according to which materials the fabrication facility would allow one to sputter to a thickness of 1 to 2 μm.

  Base pressure was reduced to the low 10^{-6} range before sputtering to reduce film contamination. Background argon flow was introduced and chamber pressure was raised to 7 mTorr. This allowed a plasma to be established and sputtering to occur. After a 3 minute burn in period to clean the target surface, a 6 nm layer of Cr was deposited onto the wafer for 1 minute at 7 mTorr pressure and 300 W power. Silver or copper was then burned in for 3 minutes, after which about 1 μm of the material was sputtered at the standard parameters of 7 mTorr and 300 watts. After deposition, the power supply was turned off and the wafers were removed from the chamber and placed in a clean storage container.

- **Step 3B: Photolithography**

Lift off is a technique by which a material is deposited onto a patterned layer of photoresist. The photoresist is subsequently dissolved with acetone which releases the portions of metal that have been deposited on it. The deposited material in contact with the clean surface should adhere while the metal that was on the resist should wash away. This leaves a pattern that is the negative of the original mask used to pattern the photoresist. In contrast to Process A, the patterned gold layer is never exposed to gold etchant. This allows the use of a seed layer such as silver or copper that may not be compatible with gold etch. HPR 504 photoresist patterning is accomplished through the standard parameters described in Process A.

- **Step 4B: Lift Off**

  The gold layer which ultimately defines the electrical traces that run from the sensing element to the edge of the chip was sputtered at the established Au sputtering parameters. Argon gas is supplied to the magnetron sputtering system after reaching a base pressure in at least the low 10^{-6} Torr range. A plasma is initiated at 7 mTorr and 75 W. The target gold is conditioned for 1 minute to remove adsorbed O_2 and H_2O before the substrate is directly exposed to sputter flux. At these parameters, 200 nm of gold is deposited in 20 minutes.

  Lift off is accomplished by submerging the substrate in acetone. As long as the acetone has a point of access, it will dissolve any photoresist it comes into contact with. Sputtering into a trench often creates a region of the film that is substantially thinner than mean. These points may serve as access points for acetone and are also the weakest points of the film. When the supporting resist is dissolved, the film not attached to the substrate will dislodge leaving the desired gold tracks. Ultrasonication in acetone will aid lift off.

Step 5: Substrate Cleaning

The final process step in both processes A and B involved cleaning the substrate with acetone. Acetone dissolves remaining HPR 504 on the substrate, preparing it for further processing. Substrates were often stored for up to a month. Despite being in a clean

environment, such long storage allowed much of the surface to oxidize as well as accumulate particulate. Increasing product yield relies on substrate cleanliness. To this end, substrates were usually cleaned whenever they were stored for more than a few days in a row. Cleaning off adhered particulate was accomplished with a 5 minute acetone ultrasonication bath followed by a rinse with IPA and DI H_2O. In cases where significant storage time had passed, substrates were immersed in an etchant corresponding to the seed layer for enough time to remove any accumulated surface oxide.

Process C

WO_3 thin film growth was accomplished through electrochemical means. Previous substrate processing resulted in a continuous metal film conducive to electroplating. A process to fabricate two point resistors from a continuous oxide film was developed so that initial deposition techniques used to study thin film growth required no additional modification. It was found that although WO_3 is stable in acidic environments it is readily etched in basic solutions. Upon further investigation it was determined that the $NaOH$ concentration in 354 photoresist developer used during patterning would also etch away any exposed WO_3. Development time had to be precisely controlled to avoid overetching of the WO_3 features. The combination of photoresist pattern realization and WO_3 etching reduced process flow complexity.

- **Step 6C: WO_3 Deposition**

  In the interest of conserving chemicals, silicon substrates were cleaved into 6 large pieces. Each piece contained 3 or 4 copies of the die pattern. Limited solution lifetime often only allowed for one or two consecutive depositions. The deposition setup was such that only 100 mL of solution had to be prepared for each electrodeposition run.

  The deposition solution was prepared as follows: A 0.1 M WO_3 solution was prepared by dissolving 3.2986 g Na_2WO_4 into ultra pure MilliQ (18.5 $M\Omega$) DI H_2O. A magnetic stir bar was used to agitate the solution while 60 μL H_2O_2 was slowly added to increase the oxidation state of the tungstate ion. The pH of the solution was

decreased to between 1.8 and 2.2 to ensure enough $[H^+]$ was present for deposition to occur but not so much $[H^+]$ that it would initiate spontaneous decomposition of the solution.

Both the patterned working electrode and a platinized counter electrode were submerged in the solution. The electrodes were positioned approximately 5 cm apart, while a reference electrode was submerged within 1 cm of the working electrode. It had been previously experimentally determined that a -0.5 V vs ref voltage provided sufficient drive for a continuous WO_3 thin film to be deposited within 18 minutes. After deposition, films were washed with DI H_2O and dried with clean $N_{2(g)}$, then stored in a clean environment.

- **Step 7C: Photoresist Application**

  Preparation for photolithographic exposure and development is very similar to the description provided in processes A and B. Attention had to be paid to the size and shape of the wafer sections. During previous lithography, substrates had been circular wafers on which resist spreads evenly and uniformly. Rather than pouring resist on a wafer while it is spinning at a spread speed of 500 rpm, the piece was covered with resist while stationary on the spinner. This ensures that every portion of the piece is covered with resist before spinning starts. A spread spin of 500 rpm for 10 seconds was used to clear the majority of excess resist off the wafer surface. This was followed by the standard 4000 rpm spin for 40 seconds. Baking the substrate at $115\,^{\circ}\mathrm{C}$ for 90 seconds served to harden the resist and drive out solvents. A cooling and rehydration period of 15 minutes readied the substrate for lithography.

- **Step 8C: Photolithography**

  The substrate was loaded into a mask aligner which was used to align the second layer lithographic pattern with that of the first layer. This was accomplished by raising the substrate holder until it was about one millimeter below the mask, then using the x, y and θ stage controls in conjunction with the alignment ccd system to match 2nd layer patterns with specific gold structures patterned on the first layer. When alignment was completed, contact vacuum was engaged, pressing the substrate against the mask. As

with the first lithography step, the resist was exposed to 405 nm and 365 nm light of 1.9 seconds.

HPR 504 development was again accomplished by submerging the substrate in 354 developer solution for 17 seconds and immediately rinsing with DI H_2O. Determining a sufficient development time to etch through the WO_3, while not undercutting the resist by over etching the oxide was critical. The extent of WO_3 etching varied slightly and it was found that no increase in development time was needed to accomplish both resist pattering as well as WO_3 etching. The pattern could then be inspected with an optical microscope to ensure sufficient etching had been accomplished.

A thin layer of organic residue known as photoresist scum, was observed covering the patterned WO_3. This layer could drastically affect the chemical sensor's surface so an alternate fabrication method as well as an organic stripping method was developed.

Process D

An alternative to Process C was developed in an attempt to avoid photoresist scum forming on top of the sensing elements. Rather than the top down WO_3 etching technique used in Process C, photoresist was aligned and patterned on the seed layer. The electrically insulating nature of the resist restricted electroplating to metallized regions exposed during lithography. Film stress was found to remain the dominant obstruction to realizing a gas sensor but this technique provided promising results.

Processing techniques are identical to those described above, but have been applied in a different order.

- **Step 6D: Lithography Preparation**

  A full unseparated wafer can be used for processing, as the wafer must only be separated into six segments for electroplating. HPR 504 was applied to a wafer spinning at 500 rpm during a 10 second spread cycle. This spread speed is conducive to the wafer being uniformly and completely coated with resist before the speed

ramps up to 4000 rpm. After the spin cycle is complete, the uniform 1.2 μm thick resist is baked at $115\,^{\circ}\mathrm{C}$ then rehydrated for 15 minutes before exposure.

- **Step 7D: Photolithography**

  Second layer alignment was accomplished by lining up specially designed features on the second layer mask with existing alignment marks patterned on the first layer. Vacuum contact was established and the pattern was exposed for 1.9 seconds. The developed wafer was submerged in 354 developer for approximately 17 seconds before being rinsed off with DI H_2O.

- **Step 8D: WO_3 Deposition**

  A three electrode deposition system relies on the voltage difference between the reference electrode and the cathode to drive the reaction. As such, the deposition parameters are generally independent of cathode surface area. The WO_3 deposition parameters, therefore, remained similar to those detailed in the above section. A 100 mL Na_2WO_4 [0.1 M] solution was prepared. 60 μL H_2O_2 was then added, followed by a H_2SO_4 titration to a pH of approximately 2.

  Only smaller segments of the entire substrate were used for electrodeposition. The substrate was cleaved into 6 pieces. The resist patterned substrates were subject to the standard electrodeposition parameters for deposition of a continuous WO_3 thin film of -0.5 V vs. ref. for 20 minutes. Upon removal from the solution, the substrates were immediately rinsed in ultra pure MilliQ DI H_2O.

  Photoresist restricted WO_3 deposition on the substrate surface to specific defined areas. Increased resistance of the baked resist prevented deposition from occurring on top of the resist. As seen in Figures 4.12 and 4.13 it was noticed that oxide growth occurred on the resist sidewalls. From a purely chemical detection based standpoint sidewall growth should not drastically affect gas detection sensitivity. Sidewall growth, however, often leads to increased thickness on portions of the beam. This could cause increased stress in the film. In some cases it was observed that the sidewall growth broke free from the beam when the resist was dissolved in acetone.

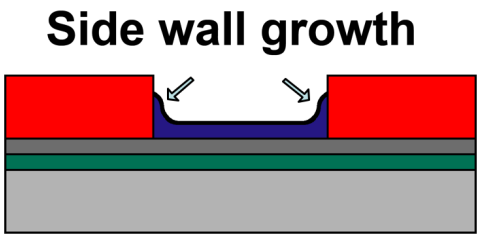

Figure 4.12: Schematic showing sidewall growth during elecroplating.

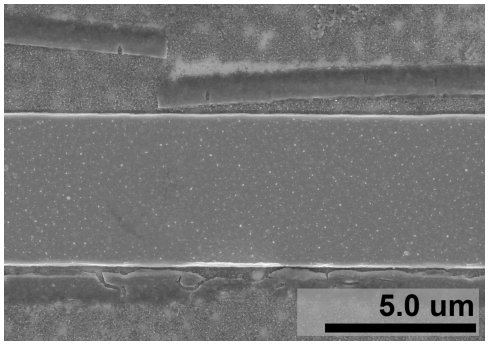

Figure 4.13: SEM showing sidewall growth breaking off after removing supporting resist.

Step 9: Substrate Cleaning

Beams proved to be fragile after release. These structures could not withstand much further processing. In select cases it was possible to remove organic materials such as photoresist scum and particulate that had built up during processing before the release step.

When WO_3 was grown in predefined locations the photoresist had to be removed in order to etch away the metal below the beams to successfully release them. Photoresist scum was not observed on top of the sensing elements but it was observed surrounding them. A gentle oxygen plasma clean could be used to remove these organic films. A bench top PLASMALAB MicroEtch Reactive Ion Etch (RIE) system was used. A standard organic stripping oxygen plasma recipe was run for 30 seconds. During this process chamber pressure was regulated at 150 mTorr, with 80 sccm $O_{2(g)}$ flow and a forward power of 120 Watts.

Step 10: WO_3 Release

Process parameters during release were dependant on which materials were used for the seed layer. Other minor differences included whether or not photoresist remaind on top of the WO_3. This depended on whether process C or D were used and affected how the final product was cleaned. The release process can be broken down into 2 main categories: metal etching and a multi step rinse process.

Metal Etch: Silver and Copper: Both silver and copper metals were used to increase

the thickness of the sacrificial seed layer. This allowed for increased metal thickness below the WO_3 beams in order to facilitate etching reactant and product transport underneath the beams. A review of processing literature [66] revealed that chromium etchant (Cr-7) removed not only chromium but could also be used to etch copper and silver. Relative etch rates for electron beam evaporated chromium, copper, and silver was found to be 170 nm/min, 280 nm/min, and 450 nm/min, respectively.

It was experimentally determined that a 5 nm Cr adhesion layer could be etched in 5 seconds while a 2 μm Ag etch managed to undercut a 40 μm mean in approximately 45 seconds. The etch rates for these sputtered films proved significantly faster than the provided rate for evaporated films. Such fast etch rates made it difficult to control WO_3 undercut during release.

Chromium: The process was simplified to growing a 100 nm Cr adhesion layer. This was due to lack of reliable repeatability with silver and copper seed layer etching. This chromium thin film would be used both as an adhesion layer for the gold traces as well as a seed layer for electrodeposition. Feature undercut could be limited to approximately 1/2 beam width.

Multi Step Rinse: Maintaining a clean surface is crucial for chemical sensor functionality. The multi-step rinse process was designed to remove all possible organic material, solution salts and particulate from the surface.

After chemically etching the seed layer supporting any WO_3 beams, the substrates were rinsed several times in a DI H_2O bath. Acetone was slowly added to the H_2O bath over the course of several minutes until the chip was submerged in a 9:1 acetone to DI H_2O bath. The chip was then transferred to a pure acetone bath and soaked for 5 minutes to ensure complete substitution of acetone for H_20 between the beams and the substrate. IPA was then added to the acetone bath and a similar solvent substitution was carried out. Finally, n-Pentane was used to replace the IPA. After a 5 minute soak in pure Pentane the chip was dried under atmosphere.

A substantial amount of photoresist scum was observed on sensors processed through top down WO_3 etching (Process C). Again the PLASMALAB MicroEtch RIE was used to clean the samples with a 30 second O_2 plasma at 150 mTorr and 80 sccm O_2 flow.

4.4.1 Materials Chosen

Gold was chosen as a suitable inert conductive material from which electrical traces could be fabricated. A successful gas analysis system has to ensure that unwanted and unexpected chemical reactions within the detection chamber do not affect the measured signal. Chromium is a commonly used adhesion layer used to prevent gold delamination from the substrate surface. If the chip temperature reaches $400\,^{\circ}\mathrm{C}$ or above Cr diffusion may cause loss of adhesion or a variation in the conductivity of the supporting circuitry. This could lead to gas reactions occurring on sections of the sensing chip that should not otherwise be affected and cause unintended parallel reactions. High temperature microelectronics have encountered problems concerning metal diffusion. Certain metal alloys such as TiW have been developed to combat diffusion.

TiW was investigated as a possible replacement for the tensile stressed Cr adhesion layer. TiW was also investigated due to its use as a diffusion barrier. In addition to inhibiting diffusion, the overall thin film stress of a TiW thin film can be altered by carefully controlling the sputter pressure during deposition.

4.4.2 Residual Stress Control in Sputtering

Controlling stress across the substrate became a key focus of this project. Stress from successive layer depositions is cumulative and will result in bowing of the substrate. For example a high stress seed layer can be removed through wet etch undercut in order to release suspended beams. The stress from the seed layer will transfer and concentrate into the beams. Often beams on a substrate are very small while the sacrificial seed layer can be very large. The overall stress in the seed layer may be minor but the cumulative concentrated stress resulting from beam release would be very large. Investigations were undertaken to develop a low stress seed layer for thin film double clamped WO_3 beams.

Stress contribution from the seed layer needed to be minimized. Chromium is a common seed layer material that was initially investigated. It was noticed that sputter deposition provided minimal control over film stress and that an approximately stress free film was very difficult to produce. A series of tests were performed to analyze the potential use of TiW as a conductive seed layer. Figure 4.14 shows a reliable stress trend when sputter

pressure was decreased from 7 mTorr to 2 mTorr.

TiW is a binary alloy that can be deposited by magnetron sputtering at low temperatures. Targets generally consist of 90% W: 10% Ti, where the Ti is added to act both as an adhesion layer for the film as well as improve oxidation resistance [92, 93]. Relative Ti concentration in the film is shown to be much lower than the target. Dirks *et al.* [92] shows that effects such as differential gas phase scattering and Ti resputtering due to neutral Ar atoms backscattered from the target cause this effect.

Further testing was carried out to determine whether the anneal temperatures during photoresist baking and lithography would eventually alter these stress levels. Two separate annealing steps were preformed at $120\,^{\circ}\mathrm{C}$ to approximate the temperatures that would be encountered during lithography. As shown in figure 4.15, these temperatures did not affect the deposited TiW.

4.4.3 Final Product

Figure 4.16 shows a successfully released beam of tungsten trioxide over a SiO_2 surface. These beams were designed to be the sensing elements of the chip, while the gold traces seen in Figure 4.17 provided a method to connect to each end of the metal oxide sensing element. Figure 4.17 shows patterned tungsten trioxide thin films on a substrate along with supporting electrical traces.

4.5 Conclusion

Several project milestones were achieved. Tungsten trioxide was electrodeposited to form a continuous thin film from a peroxytungstate solution. A continuity dependance on film thickness was observed and relatively long term solution stability was achieved. WO_3 was characterized with XPS. Patterning was achieved through both photoresist masked wet etching as well as masked electrodeposition. A process to fabricate supporting conductive traces to provide electrical contact to the sensors was integrated into sensor production. Wire bonding to these traces for off chip connection was also achieved. Finally, intact WO_3 beams were released over an insulating substrate.

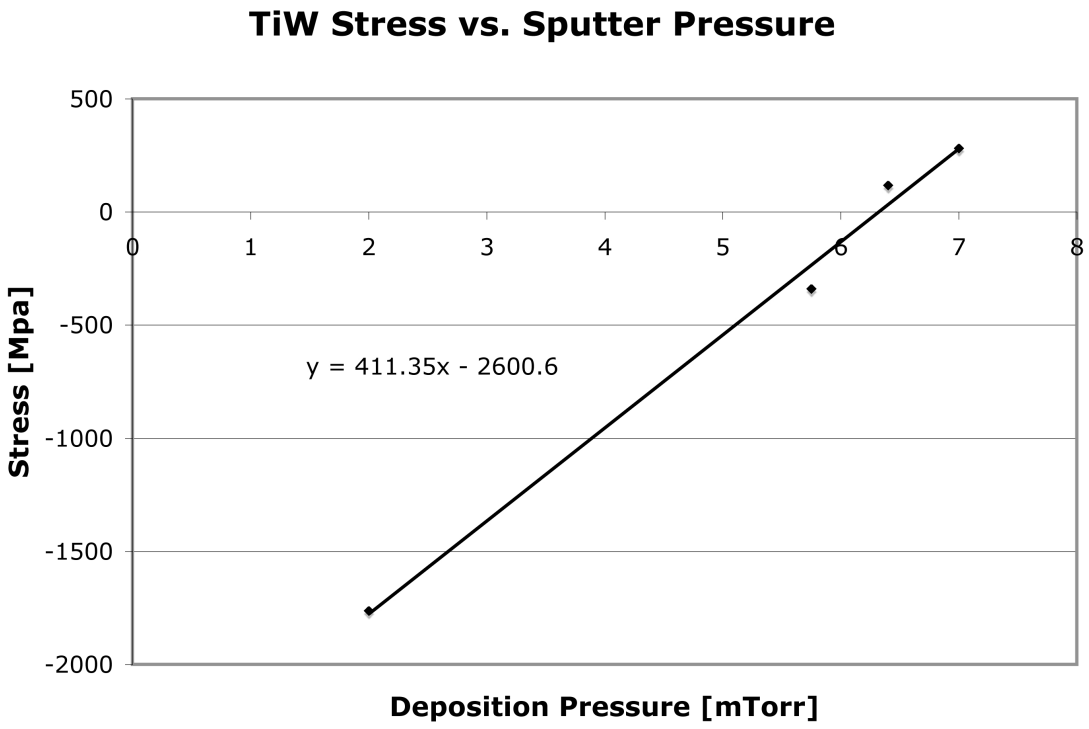

110

Figure 4.14: Graph of seed layer sputter stress as a function of pressure.

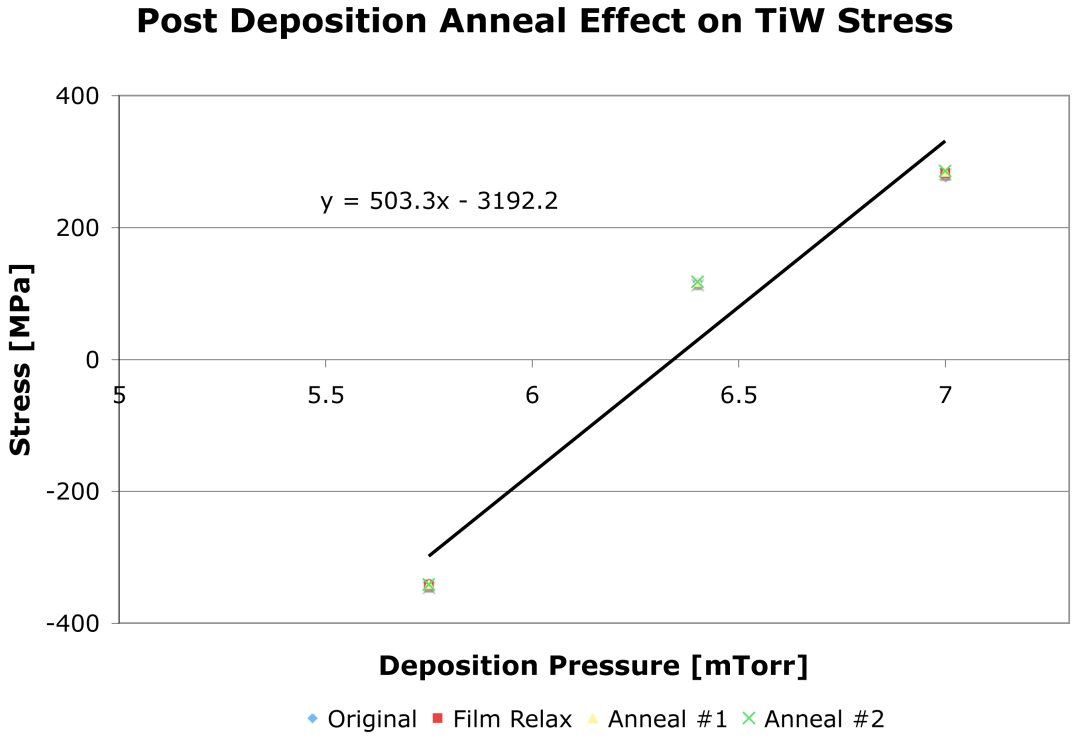

Figure 4.15: Graph of seed layer stress after low temperature annealing.

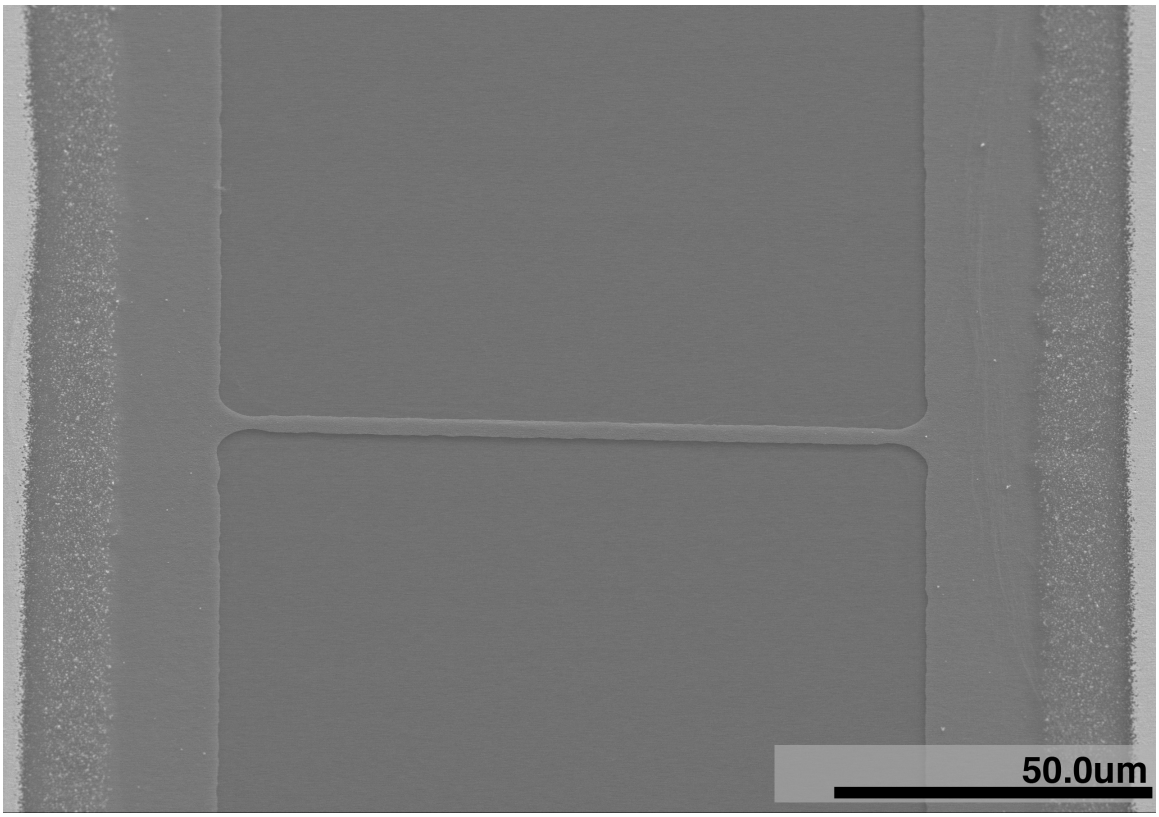

Figure 4.16: SEM of a successfully released WO_3 beam.

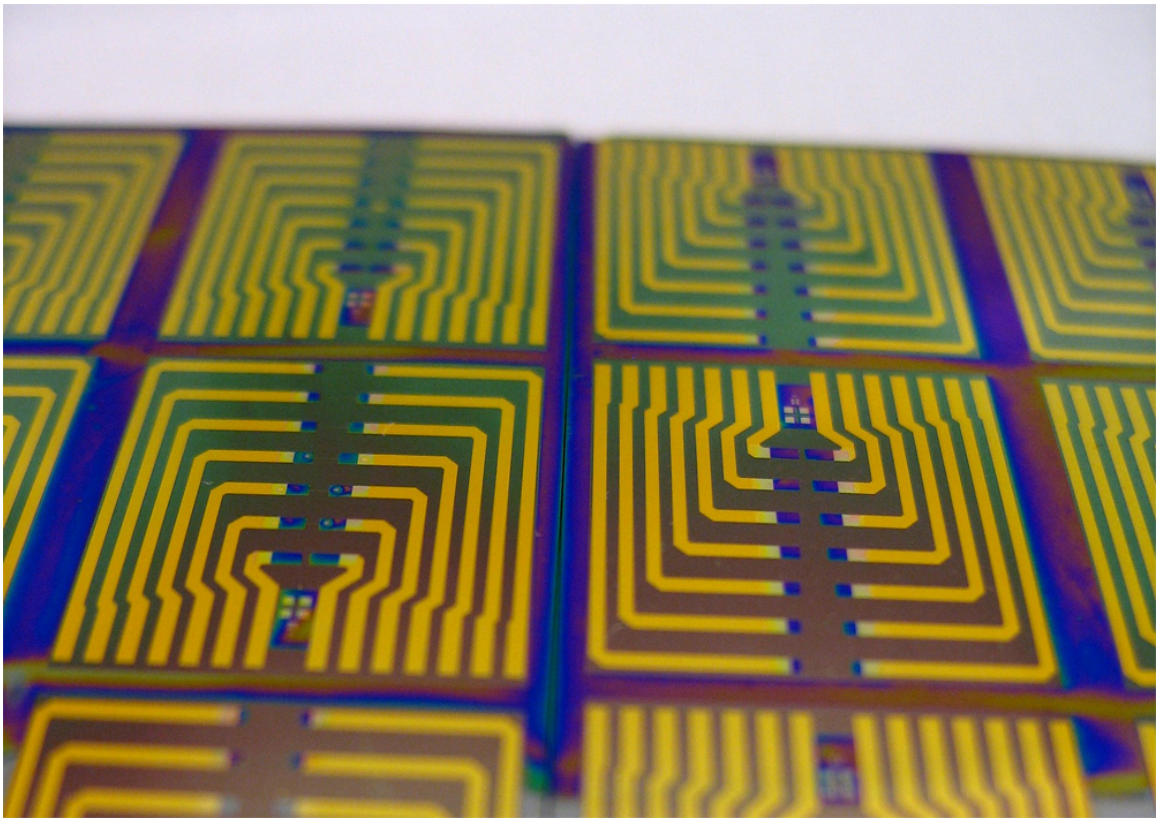

Figure 4.17: SEM of WO_3 thin film resistors microfabricated onto supporting gold traces.

4.5.1 Future Work Required

Electrodeposited WO_3 films are most often fabricated for their electrochromic properties. As such, little attention was paid to the stress and nanoscale continuity of the films. They were generally found to be nanocrystalline and visually continuous upon darkening (blue).

Significant amount of compressive stress developed in the WO_3 film during electrodeposition. Subsequent analysis of the films attributed the inherent film stress to intercalated H^+ and Na^+ ions into the film. Other sources of stress have been shown to include H_2O incorporated into the film [84], as seen in the following chemical reaction equation:

$$H_2WO_5 \cdot H_2O + (2+2x+y)H^+ + (2+2x+y)e^- = H_yWO_(3-x) \cdot pH_2O + (3+x-p)H_2O \tag{4.6}$$

Hepel *et al.* also suggests that a predominant mass increase results from the formation of $WO_3 \cdot \frac{1}{3}H_2O$ [84]. Several sources for thin film compressive stress that have been established, including ion intercalation and stress transfer from the seed layer. Stress present in both the seed layer as well as the tungsten oxide sensing layer caused great difficulty in realizing a reliable process for the fabrication of suspended WO_3 beams for gas sensing. Thin film stress in the suspended bridges needs to be eliminated in order to successfully realize a reliable fabrication process.

5

Segmented Nanowire Fabrication

Semiconducting materials have attracted considerable attention in electrochemical sensing. Recent research has shifted from thin film sensing to fabrication of integrated nanowire arrays. Templated electrodeposition of metals, and semiconducting materials, with porous aluminum oxide (PAO) has proven to be a simple and reliable method for nanowire fabrication [5, 94, 95]. Electrodeposition leverages the ability to electrostatically attract ions in a solution and deposit them onto an electrode. It has been shown that metallic and semiconducting nanowires have been reliably formed through electroplating into the vacant pores of a porous alumina membrane. Combining the previously mentioned electrodeposition technique with PAO enables the realization of highly uniform nanowires through templated electrodeposition. Segmented nanowires for chemical sensing, where a short metal oxide segment is intercalated between gold nanowire ends, have been grown. Segmented nanowire fabrication and characterization techniques will be presented in this chapter.

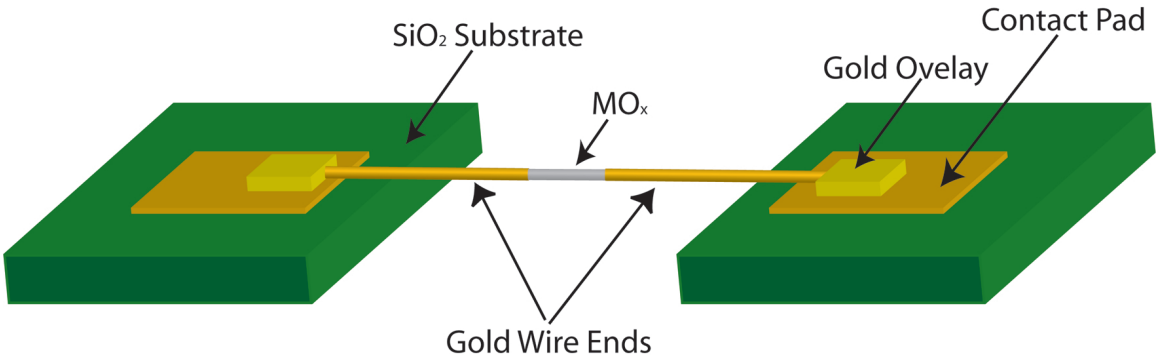

Figure 5.1: $Au/MO_x/Au$ nanowire sensor layout.

5.1 Sensor Layout: $Au/MO_x/Au$ Nanowire

A metallic layer is sputtered onto the back of the porous anodic alumina and provides the means for the template to act as an electrode. This conductive layer acts as a seeding layer for wire growth at the deepest point within each nanopore. The resistive nature of aluminum oxide prevents charge build up on its surface during electroplating. This restricts deposition to the conductive contact within the pores. It forces wire growth to initiate at the seeding layer and continue towards the surface of the membrane. The resulting wires are then released by selective etching of the seed layer and alumina template.

Variations on the previously mentioned fabrication method are currently being researched. WO_3 is a material system researched predominantly for its electrochromic effects. Electrodeposition of WO_3 has therefore been thoroughly explored and has become relatively common [96,97]. Application of WO_3 to gas sensing was first explored by Reyes *et al.* [4]. These films were fabricated through reactive gas deposition and material viability for gas sensing was demonstrated. It has also been demonstrated that the addition of certain dopants, such as Al and Au, can cause an increase in sensitivity [4]. Finally, structural characterization methods such as TEM and XPS have enabled increased understanding of the mechanisms surrounding electrodeposition as well as film morphology. The recent integration of porous anodic alumina as a deposition template has resulted in the realization of highly uniform metallic and semiconducting nanowires. These straightforward and well documented steps to nanowire realization have created an easily expandable process that

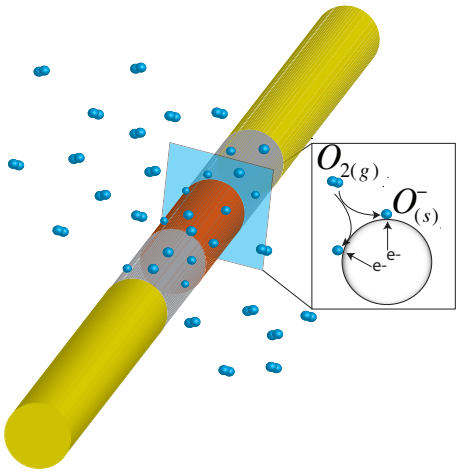

Figure 5.2: Surface oxidation occurring on a segmented wire.

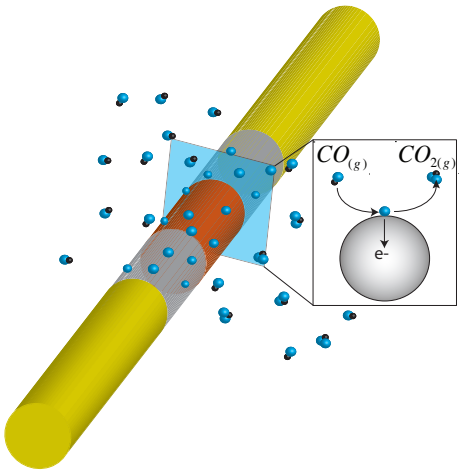

Figure 5.3: Reduction reaction occurring on a segmented wire.

can satisfy any potential industrial demand.

5.2 Deposition Setup

The porous membrane was supported by a metallized silicon substrate, and pressed against an o-ring connecting to one end of the glass electrodeposition cell. When held in a vertical position the membrane was located at the bottom end of the cell while a platinized substrate was inserted in the top end to act as the anode.

Anode

A platinum anode was prepared by sputter coating a thermally oxidized silicon wafer with a 100 nm Pt layer. The metallized wafer was diced into long thin strips that would fit in the top opening of the cell.

Process Parameters: A clean SiO_2 coated silicon wafer was loaded into the magnetron sputtering system. Once a suitable base pressure was reached, a 6 nm titanium adhesion layer was deposited at 7 mTorr and 300 W. The 100 nm platinum layer was subsequently deposited at 7 mTorr and 75 Watts. The wafer was diced into 1 cm wide strips. The pieces were then cleaned in an acetone ultrasonication bath to remove silicon particulate remaining after dicing.

Cathode

The cathode was prepared by sputtering a thin seed layer of silver on the back of a porous template. Silver was selected due to its conductivity and because it can easily be sputtered. HNO_3 is an Ag etchant that does not react with any of the other exposed material nor with the template materials themselves [65, 66].

Process Parameters: Backside membrane metallization was accomplished via sputter deposition of silver. Membrane pore diameter varied between 20 nm and 200 nm. A constant thickness of approximately 300 nm Ag layer was thick enough to close the pores which could then be used to create a seal for the one end of the electrochemical cell. No adhesion layer was used to avoid complex etching deposition. The Ag layer was sputtered directly on the back of the membrane at 300 W under a 7 mTorr Argon plasma.

5.2.1 Potentiostat

A Princeton Applied Research 363 potentiostat provided constant current while the corresponding voltage output could be monitored on an analog display. Electrodeposition has been discussed at length in previous chapters. It is, however, necessary to distinguish between the three electrode potentiostatic deposition setups used for thin films versus the two electrode galvanostatic systems used to grow nanowires. A two electrode approach to deposition was taken due to the ability to regulate wire growth rate by varying the current passed through the solution.

Tuneable Properties

Galvanostatic deposition occurs when a current level is held at a precise point during electroplating. The voltage level is allowed to rise and fall as dictated by the reaction kinetics and solution resistance. Ready-to-use electroplating solutions, such as the gold, silver and tin solutions obtained from Technic Inc., have been engineered to provide pure films with high etch uniformity. These solutions have been tested to ensure that parasitic reactions do not occur within a wide margin of the optimal deposition potential. As such, they are excellent candidates for constant current deposition.

Solution agitation provided a means to alter deposition parameters which reduced

variation between successive depositions. The electrodeposition cell was large enough that a stir bar could be placed on top of the PAO membrane while a magnetic stir plate was placed underneath the cell. This enabled solution agitation. The friction between the stir bar and the PAO caused some alumina pores break, resulting in fragments contaminating the membrane surface. The deep and narrow nature of the pores also negates the effects of any external agitation. Although chemical transport would increase near the top of the membrane, the electroplating reaction would still depend on the reaction kinetics at the growth interface.

Ultrasonic vibration was attempted, but proved difficult due to the need to submerge the electrodeposition cell in water. A piezoelectric disk was placed between the metallized substrate and the membrane. The membranes fractured often due to their brittle nature. The entire electrochemical cell was placed within an ultrasonic bath of DI H_2O. The procedure of continuously having to remove the cell to change the solutions contained in it caused great difficulty.

Raising solution temperature is possible with this setup. A hot plate can be placed against the bottom of the cell where thermal conduction through the metallized Si substrate and the membrane can occur. Reaction kinetics are temperature dependant and it was found that an increase in temperature accelerated spontaneous decomposition of the WO_3 electroplating solution. The solution stability time was reduced below 20 minutes.

5.3 Process Flow

Membrane Preparation

Two major types of porous membranes are typically used for nanowire growth. Porous Anodic Alumina (PAA), otherwise referred to as Porous Aluminum Oxide (PAO), and Track etched polycarbonate membranes. Both types are commercially available from companies such as Millipore and Whatmann. Each of these two membranes are suited for specific deposition and release conditions.

Three factors are desirable in a seed layer for nanowire growth. The layer must be deposited through sputter deposition. Its etchant has to be compatible with both the template and any material to which it would be exposed. It also has to be conductive.

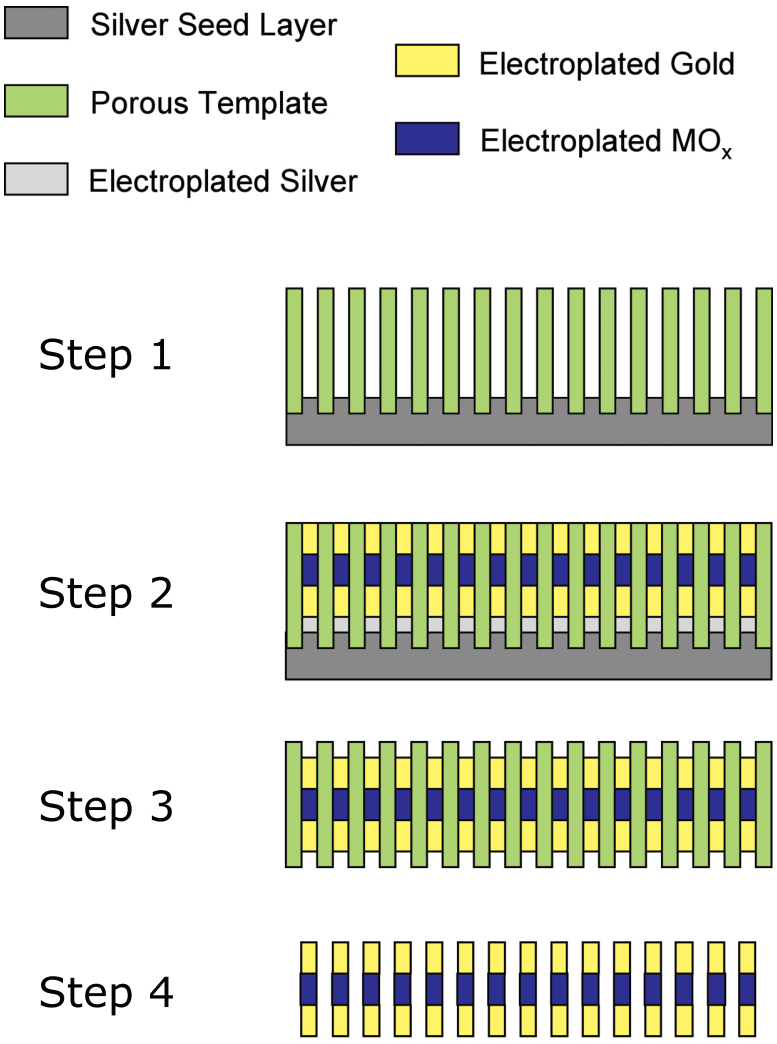

Figure 5.4: Schematic providing an overview of the $Au/MO_x/Au$ fabrication process flow.

Silver was chosen due to its compliance with the above requirements as well as its high etch rate and commonly available etchant.

Electrodeposition

Electrodeposition was achieved with a two electrode constant current method which was adopted to maintain control over wire growth rate within the porous templates. The chemical cell was designed so that the seed layer at the bottom of the porous membrane functioned as the cathode. The anode was a platinum covered silicon substrate which was inserted into the plating solution through the opening at the top end of the cell.

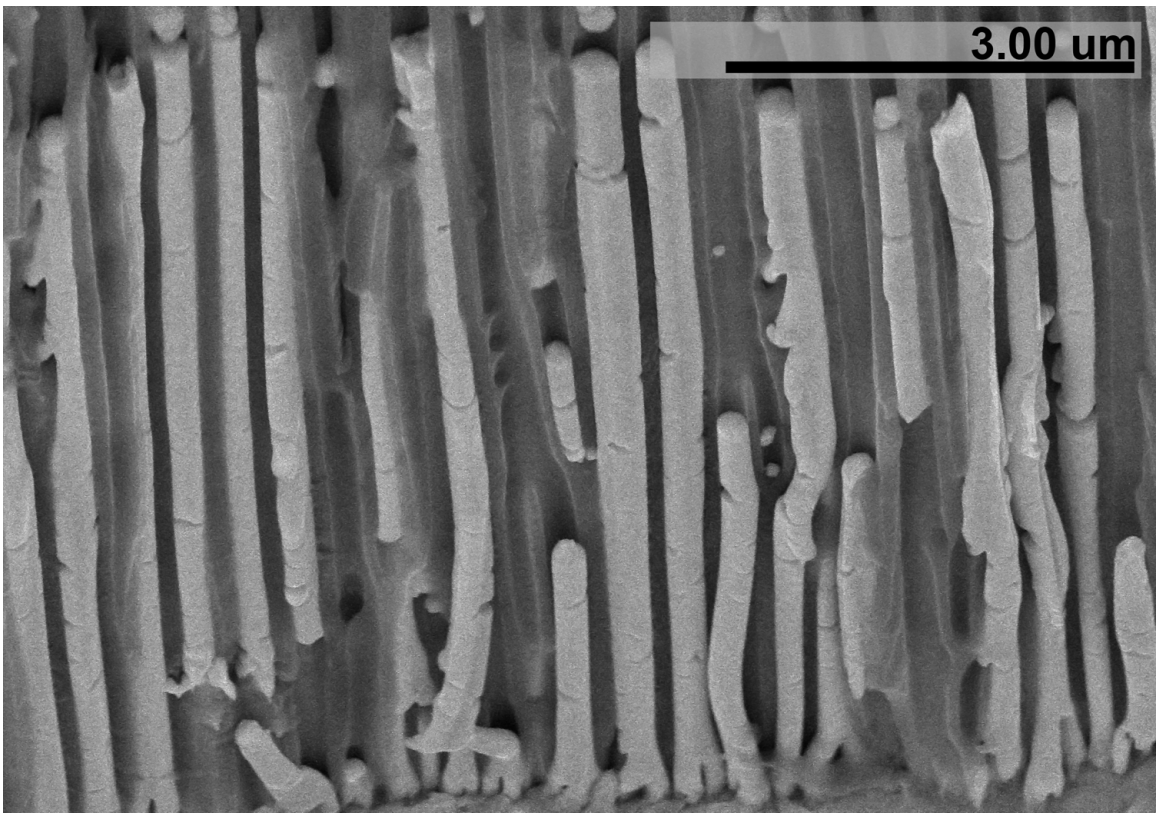

Figure 5.5: SEM image shows significant branching near the end of gold wires in an Al_2O3 membrane with a 200 nm average pore diameter.

Originally gold was electrodeposited directly onto the seed layer. During the sequential etch stage it was noticed that gold diffuses into the thin film. This formed largely continuous film of gold across the bottom of the template which prevented template etching. The lower ends of the Al_2O_3 pores branched greatly. Silver was plated into the lower

micrometer of the template to counteract Au diffusion and wire branching.

Metal deposition starts at the seed layer and grows towards the upper surface of the membrane. Segmented wires need to be grown in a serial fashion. If a gold/MO_x/gold nanowire is desired, Au must be deposited first, followed by the MO_x segment. Gold must then again be deposited to grow the distal wire segment.

Seed Layer Etch

In order to properly release the nanowires the silver seed layer needed to be removed before template etching. Nitric acid is an excellent etch for Ag [65]. It is able to etch the seed layer as well as any silver deposited in the pores. This etch will not affect the templates or the gold deposited within the pores.

Typical silver etch parameters: HNO_3 was diluted with 4 parts nitric acid to 1 parts DI H_2O. The etch rate at room temperature was approximately 50 nm/sec. Samples were generally etched for 5 minutes to ensure HNO_3 penetration into the membranes pores. The membrane was then removed from the etchant and rinsed in 2 separate DI H_2O rinse cycles.

Wire Release

Two types of membranes were used. Each had a specific etch chemistry.

Three methods to etch PAO filters were found. Potassium hydroxide (KOH) is a commonly used alumina etchant [65]. This etchant, however, is not compatible with many metals [66]. Gold was the only sufficiently unreactive material that could withstand KOH etching. $NaOH$ was the second method [5]. Tin and copper segments could both withstand this etch. As WO_3 is etched by basic solutions, a third method had to be developed. HCl at $80\,^{\circ}\mathrm{C}$ had been shown to etch Al_2O_3. Tests were performed to assess the potential for this acidic etch and it was found to be compatible with WO_3 thin films.

Track etched polycarbonate filters were shown to etch in dichloromethane (CH_2Cl_2). This etchant dissolved the membrane in approximately 20 seconds.

Filtration

Gold wires fabricated in a TEPC template can be easily filtered from dichloromethane with a Al_2O_3 filter. A stainless filter holder (Millipore: Product# XX3002500) with a male luer lock syringe connection proved to be a versatile filtering device. This stainless steel filter chamber contained a filter support mesh, 2 o-rings and used virtually any 25mm diameter filter. A syringe could be attached directly to the filter, which relied on syringe pressure to drive fluid through the device.

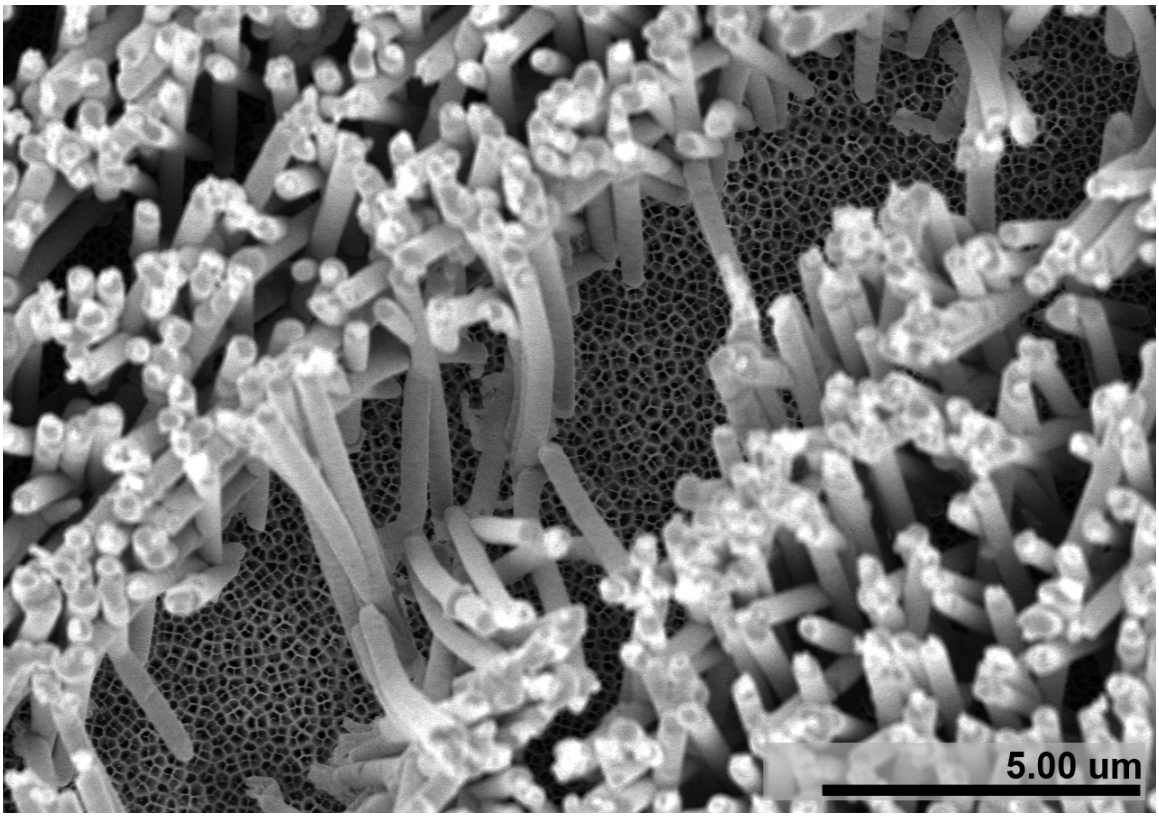

Figure 5.6: SEM micrograph of gold wires which were filtered using a Al_2O_3 membrane.

5.4 Gold Nanowires

Gold nanowires were first fabricated as a stepping stone to more complex wire configurations. TG25E Au electrodeposition solution is a cyanide free plating solution that was obtained from Technic Inc. This ready-to-use solution provides a high purity 99.99% gold film and was found to be suitable for Au growth deep within a porous membrane.

5.4.1 Experimental Parameters

Gold wires were used as a test platform for the growth and release of nanowires. Templated gold nanowire growth was achieved in both PAO templates as well as TEPC templates. Process parameters for wire fabrication followed the established process flow.

A backside metallized porous membrane was held firmly between a silver coated Si wafer and the glass cell. Silver electroplating solution was poured into the cell and a platinum anode was inserted into the solution. Electrical connections to the potentiostat were made and the potentiostat was set to 700 μA for 30 minutes. The cell, membrane, and anode were well rinsed with ultra pure MilliQ DI H_2O before setting up the Au deposition. The cell was filled with TG25E Au electroplating solution and set to 87.5 μA for 6 minutes, then ramped up to 350 μ for 2 hours and 45 minutes. After deposition, the cell, anode and membrane were once again rinsed with ultra pure DI H_2O. The membrane was then stored in a clean environment until release could be performed.

Nitric acid was employed to remove the silver backing layer as well as the silver initially grown in the template. After a thorough rinse in DI water the templates were etched, thereby releasing the wires. Wires were filtered from the solution and then transferred to a glass bottle. The bottle was subsequently filled with DI H_2O in which the wires were redispersed.

5.4.2 Results and Discussion

Initial growth in Al_2O_3 produced positive results. Deposition with TG25E Au electroplating solution was straightforward and consistent. Initial SEM characterization was performed on wires grown in Al_2O_3 before release as well as after release and filtration. Wires grown in TEPC membranes could only be characterized post release.

PAO Template

Wires grown in PAO membranes were shown to exhibit a high degree of branching and non-uniform diameter. A typical example of branching and surface non-uniformities can be seen in Figure 5.7. Although gold plating occurred in each pore for the same amount of time, lengths of the wires vary considerably. This suggests that for a given wire length

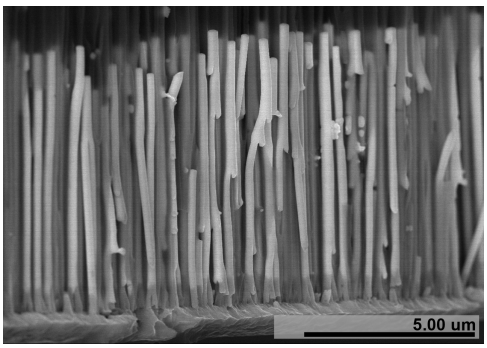

Figure 5.7: SEM of the branching and non-uniform nature of Al_2O_3 template grown gold wires.

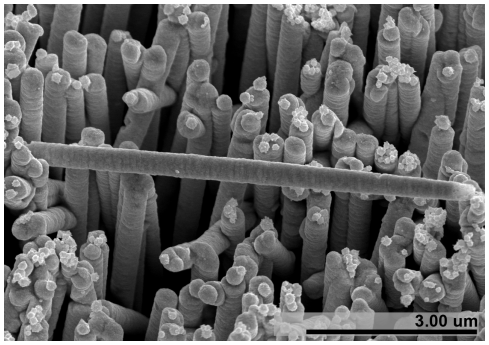

Figure 5.8: SEM of a released gold wire grown via electrodeposition in a track etched polycarbonate template.

there is a significant variation in volume.

PAO templates with thinner pores but the same pore density were ordered in an effort to reduce contact between adjacent pores. Whatman Inc. offers PAO membranes with 200 nm pores that thin down to 20 nm for the lower 2 μm. Figure 5.9 shows that the 20 nm pores are highly branched and unsuitable for nanowire growth.

TEPC Template

TEPC templates produced consistently straight and defect free wires. Wires tended to be slightly conical in shape but the overall smooth features and lack of protrusions generated very consistent wire dimensions across each batch.

After releasing several Au wires it was noted that one end of the wires consistently had a very rough end. This can be seen in figure 5.10. The electrical current running through the system is not extremely high but it may play a role in increased diffusion between gold and silver. It is possible to counter diffusion with diffusion barriers or lower electroplating current and alternate seed layer materials. An effective solution to the rough wire ends was to dip the substrates into gold etch for approximately 2 minutes between the silver seed layer etch and the release etch steps. This leaves them with smooth ends by allowing the gold etch to penetrate the pores and perform a partial etch back of the wires.

Gold wire release proved problematic when etching both Al_2O_3 and track etched polycarbonate membranes. Section 5.3 outlines three separate methods to etch alumina.

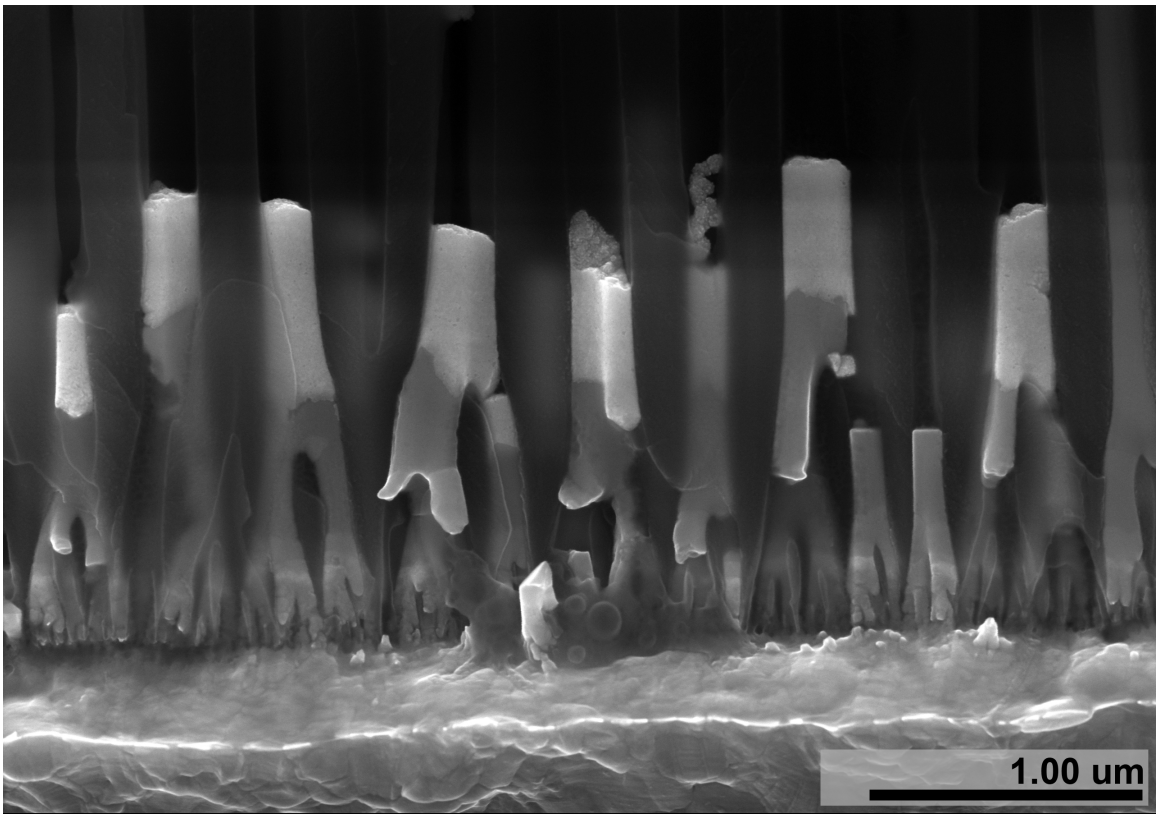

Figure 5.9: SEM showing Al_2O_3 membranes with a 20 nm pore rating. 200 nm - 300 nm pores were observed throughout the membrane up to the lower 1 μm, when branching restricted pore diameter to 20 nm.

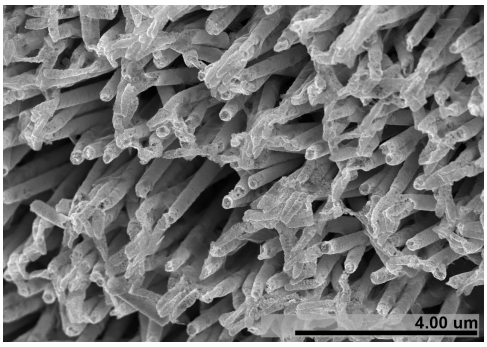

Figure 5.10: SEM image showing rough gold wire ends after release.

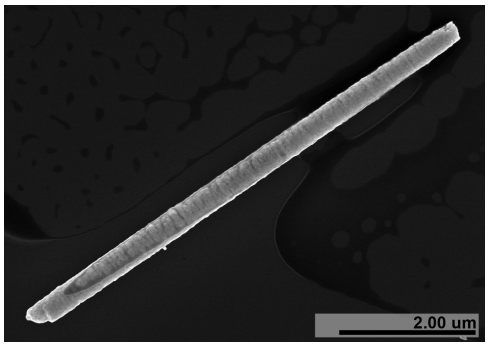

Figure 5.11: SEM showing a gold wire after 2 minute pre release gold etch.

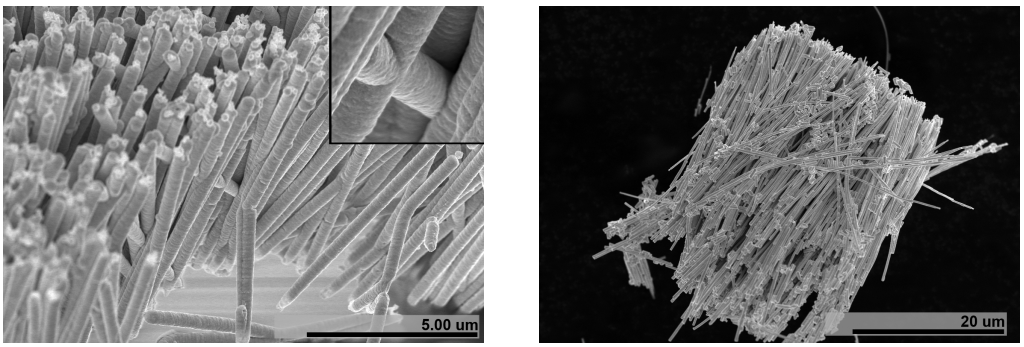

Figure 5.12: SEM images showing high levels of interconnection wires grown in both porous anodic alumina and track etched polycarbonate templates.

Several etch tests were performed and it was determined that KOH significantly increased wire yield relative to both $NaOH$ and HCl.

Backside metallization of TEPC membranes imparted stress on the flexible membrane and caused it to curl into a tube upon removal from the sputtering system. Slight rippling in the membrane occurred even though the electrochemical cell held the edges of the membrane firmly against the metallized silicon support. A continuous and uniform silver layer had been deposited across the entire back of the membrane. It was, however, noted that the deposition rate decreased when ripples in the membrane caused a periodic break in direct contact with the supporting silver coated substrate. This resulted in variations in deposition rate across the template and negated the control over growth rate provided by galvanostatic deposition.

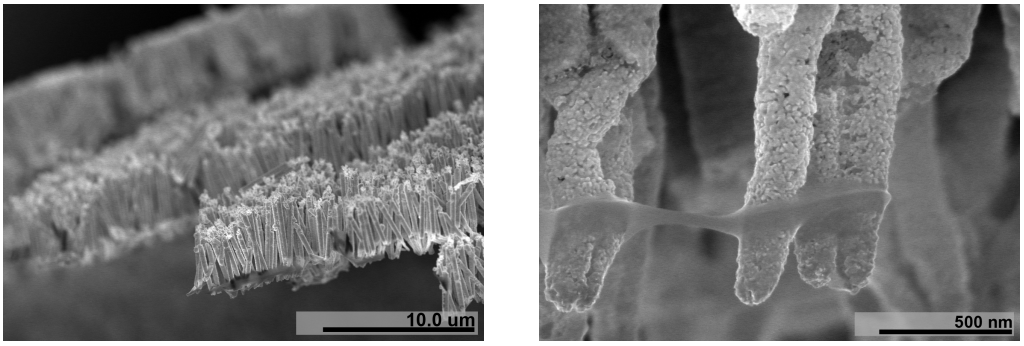

Figure 5.13: SEM showing a thin layer of residue that remained after etching a polycarbonate membrane in dichloromethane.

Relative to Al_2O_3 etching, wire release from TEPC membranes using dichloromethane is fast and uncomplicated. Filtration using Al_2O_3 membranes is very compatible with the solvent. A reoccurring problem was the inability to remove a residue that remained on the wires after release. This can be observed in Figure 5.13. The residue was only seen on one end of the wire. It could conceivably contaminate the sensor surface and interfere with subsequent processing. Although alternate etches were not available, Whatman representatives reported that m-Cresol or Chloroform would also etch the membrane and would perhaps remove the remaining contaminant.

5.5 Segmented Nanowires - Sn and Cu

SnO_2 based chemical sensors have been studied in great detail [5, 47]. Tin electrodeposition using a commercially developed electroplating solution enabled the fabrication of segmented wires. These wires were several micrometers long with a few hundred nanometer tin segment intercalated halfway through. Weakness in the wires was apparent where material transition took place. A few experiments were completed to assess the viability of a post deposition anneal to promote diffusion between tin and gold. The experiments were aimed at mechanically strengthening these interfaces. The experimental details surrounding the chemical release and characterization of these wires is presented below.

5.5.1 Experimental Parameters

Sn Deposition: Techni Brite Acid Tin ready-to-use solution was purchased from Technic Inc. This solution provided an efficient high purity Sn film and was found to work well deep within the porous membrane. The tin deposition current was maintained at 700 μA for approximately 15 minutes. At these parameters the tin deposition rate was about 15 nm/min. Techni Brite Acid Tin solution proved difficult to rinse from the electrochemical cell and would form a dark black precipitate if mixed with TG25E Gold plating solution. The cell was rinsed with pure DI H_2O at least 3 times before and after tin plating solution entered the cell.

Cu Deposition: Cu electroplating solution was mixed from a combination of copper

sulfate pentahydrate and sulfuric acid. 245 g $CuSO_4 \bullet 5H_2O$ was dissolved in 50 mL Di H_2O, followed by the addition of 3 g H_2SO_4. Typical deposition was performed at 700 μA current for 15 minutes. These deposition parameters generally produced a 100 nm thick film.

Tin intercalated wire release occurred in 25% $NaOH$, rather than KOH, due to its compatibility with tin. Strong $NaOH$ was chemically incompatible with the filters previously used. A solution to this problem was to heavily dilute the $NaOH$ after template etching had occurred, then to filter the dilute solution with a second unprocessed Al_2O_3 membrane.

5.5.2 Results and Discussion

Sn

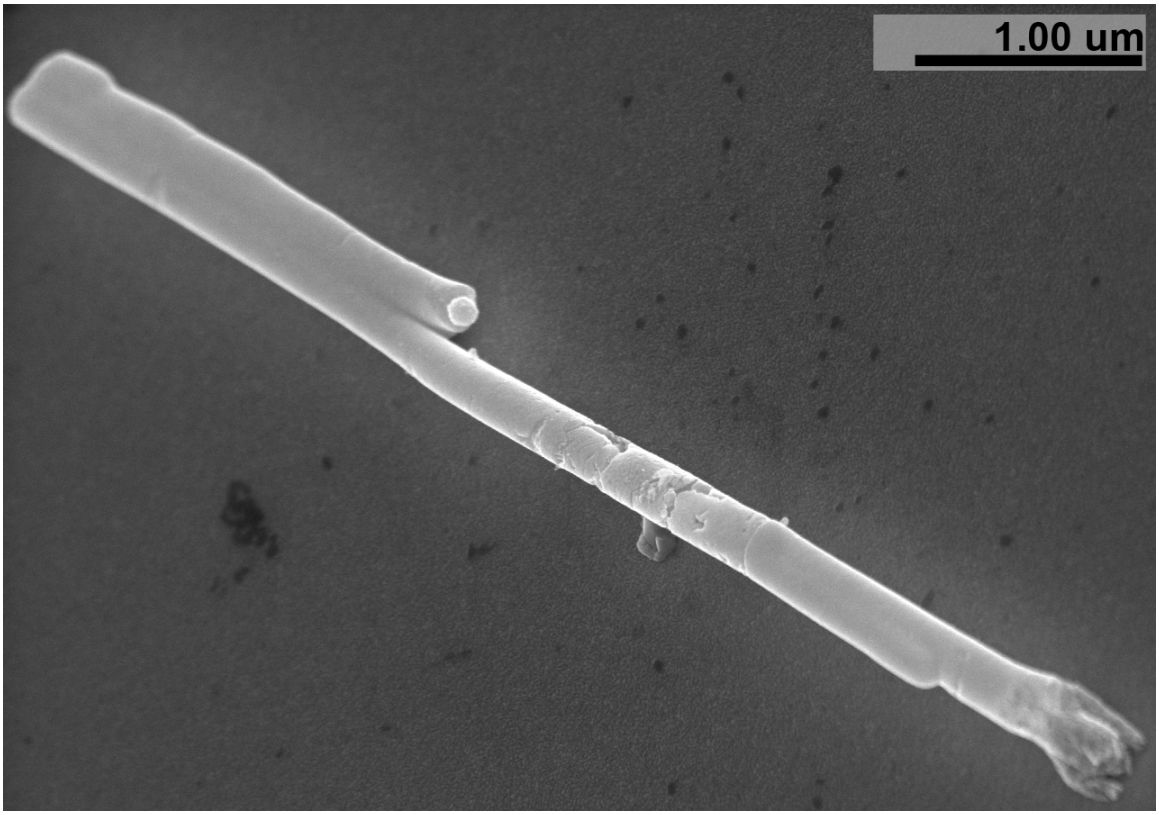

Figure 5.14: SEM image of gold wires with intercalated tin segments.

Tin segment synthesis proved to be a straightforward procedure. Figure 5.15 shows thin

tin segments in the middle of long gold wires. Segmented wires were found to be noticeably weaker than pure Au wires. A common wire fracture location is seen to be at the $Sn - Au$ interface, as shown in Figure 5.15. Upon closer inspection, poor growth continuity can be observed surrounding the tin segment. A small fraction of these wires were able to withstand release and filtration, as seen in Figure 5.14.

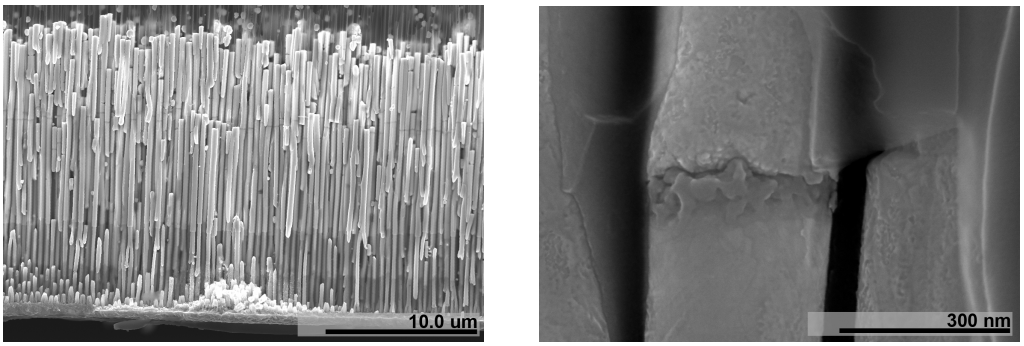

Figure 5.15: SEM images of Sn intercalated gold wires grown in porous anodic alumina.

Cu/Sn

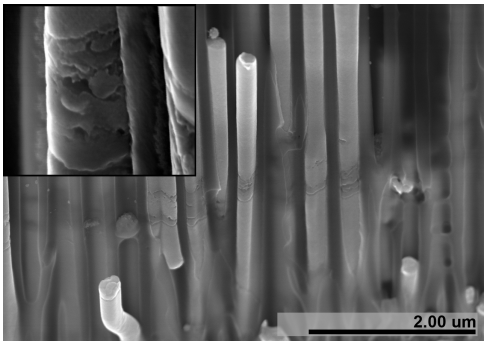

Figure 5.16: SEM of Copper/Tin segments deposited between two gold wires in a porous anodic alumina template.

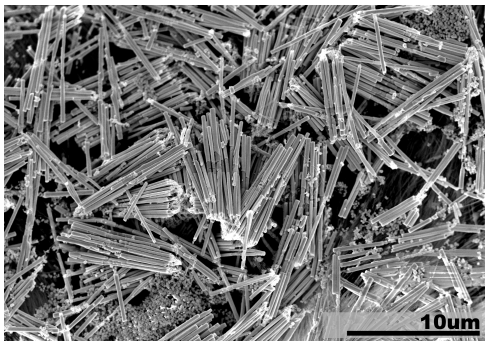

Figure 5.17: SEM image of wires fabricated with sequential Cu and Sn segments that were successfully released.

Copper and tin segments were electroplated into a PAO template, as seen in figure 5.16. As opposed to purely tin wires, these segments were deposited at a lower current to avoid unnecessary intermetallic diffusion. These wires were released from the template using 25% NaOH etch. A significant increase in post filtration yield was observed. Mechanical

weakness observed in the tin intercalated segments surfaced again with these complex wires.

Effects of Pre-release Annealing

Wires were observed to frequently fracture at the material interfaces. The interfaces had to be strengthened in order to increase the mechanical stability of segmented wires. A possible solution was found in the diffusion properties of tin and gold. Figure 5.18a shows wires produced with a much larger intercalated tin segment than in prior experiments. This was done so that the Sn segments would remain visible despite significant $Sn - Au$ diffusion. One can clearly see a narrow connection where tin has been electrodeposited on gold. SEM inspection showed that the wires had a tendency to break at these locations. Similar samples were annealed at $240\,^{\circ}\mathrm{C}$ for 15 minutes to promote diffusion. Using the HA detector at a high accelerating voltage to analyze backscattered electrons allowed the wires to be viewed behind a layer of Al_2O_3. Figure 5.18b shows that a significant amount of diffusion occurred during annealing and that many of the wires have discontinuous segments. Broken wires can be attributed to differences in the coefficient of thermal expansion of each material. For the linear case this can be described by:

$$\frac{\Delta L}{L_o} = \alpha_L \Delta T \tag{5.1}$$

Where L_o is the original length, α_L is the coefficient of thermal expansion and ΔT is the change in temperature.

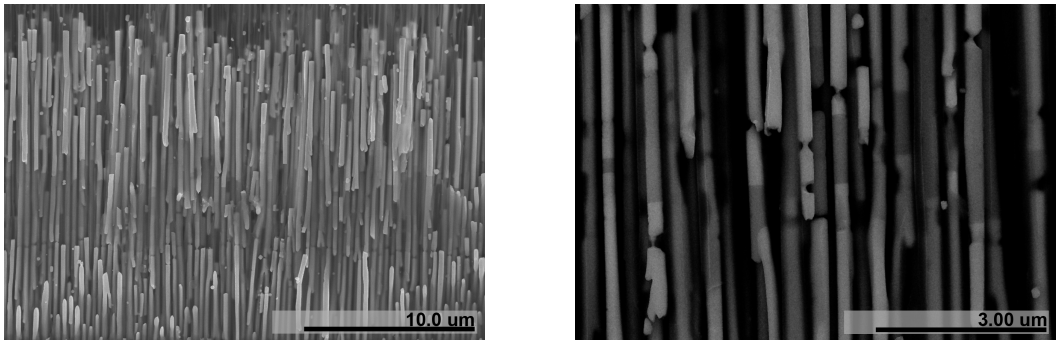

(a) Post deposition. (b) After 15 minute anneal at $240\,^{\circ}\mathrm{C}$

Figure 5.18: SEM images of Sn segmented wires.

5.6 Segmented Nanowires - WO_3

It was shown that WO_3 deposition relies greatly on the deposition voltage. The electrodeposition cell used for templated wire growth is not compatible with a reference electrode as the cell is too narrow to support one. Wires had to be grown via amperometric deposition.

5.6.1 Experimental Parameters

Sample preparation had to occur before depositing WO_3 into the porous templates. Initial template preparation can be found in section 5.3. Gold electroplating with a silver pre-fill is explained in section 5.4.

Electrodeposition solution was prepared in a similar manner to Chapter 4: A 0.1 M WO_3 solution was prepared by dissolving 3.2986 g Na_2WO_4 into ultra pure MilliQ (18.5 $M\Omega$) DI H_2O. A magnetic stir bar was used to agitate the solution while 60 μL H_2O_2 was slowly added to the ionic solution to increase the oxidation state of the tungstate ion. The pH of the solution was decreased to between 1.8 and 2.2 to ensure that enough $[H^+]$ was present for deposition to occur, but at the same time limit its concentration to prevent spontaneous decomposition of the solution.

Deposition parameters, such as deposition current and time, were initially established through trial and error. The solution recipe remained constant and allowed the development of relatively consistent deposition parameters.

5.6.2 Results and Discussion

Solution high in tungstate ion concentration fills every pore when current is initially applied to the system. Current will drive WO_3 deposition at the point on the cathode that offers the least resistance. Initially, WO_3 deposition will occur on the electroplated gold wires that directly contact the cathode due to their low resistance. Limited chemical diffusion into the long and narrow pores will eventually result in an environment adjacent to the gold wire ends that is depleted of tungstate ions. This will cause the solution resistance to increase. As the solution resistance climbs, the insulating substrate could provide a path of

least resistance to the gold wires. WO_3 deposition will eventually occur on the sidewalls of the template. Figure 5.19(a) clearly shows WO_3 deposition along the walls of the alumina pore. The level of chemically depleted solution in the pore climbs to the upper surface of the membrane. A point will be reach where solution diffusion is sufficient to support continuous WO_3 deposition. At this point the pores will fill with electroplated WO_3,as seen in Figure 5.19(b).

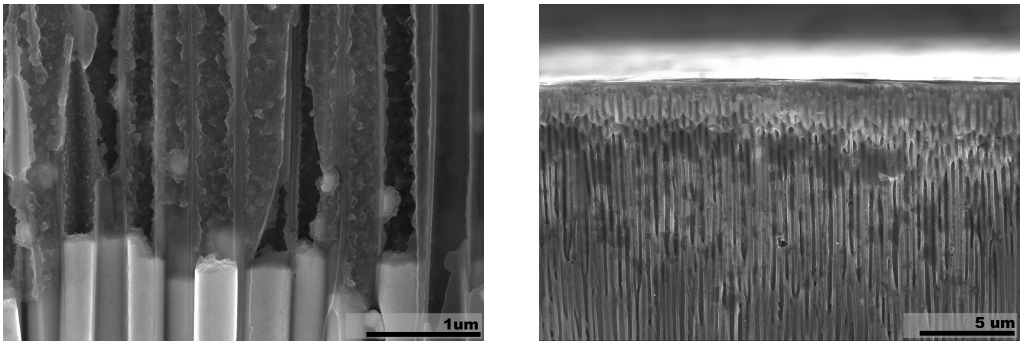

Figure 5.19: SEM of Au wire growth followed by WO_3 deposition in a PAO template.

5.7 Conclusion

Gold wires were easy to produce and release in both porous anodic alumina templates and track etched polycarbonate templates. A marked difference in wire uniformity was found to exist between wires formed in a PAO template and those formed in a TEPC template. The relatively unpredictable radius and large protrusions on the PAO wires could conceivably be transferred to metal oxide sensing segments. The resulting chemical detection response would be unpredictable from sensor to sensor. The porous template vendors stated that the canals were uniform and did not branch. It was found that the canals were branching, often funnel shaped and of varying diameter.

Segmented nanowires were deposited through templated electrodeposition. Problems with wire filtration and rinsing proved to be the greatest contributor to low process yield. Fibrous filters, although able to withstand the harsh chemicals used during wire release, tended to trap the wires within the network of filaments. Non-fibrous filters were either slowly etched by the wire release chemicals, or entirely chemically incompatible. Trying

to get the wires off a filter surface with ultrasound caused them to break.

WO_3 was successfully deposited in an insulating PAO template. A galvanostatic wire growth method limited the ability to properly control tungsten trioxide growth within the pores.

6
Conclusion

The development of a metal oxide based gas sensor is addressed. It attempts to move past the development of a basic sensing element to the construction of a working sensor. The two overarching project components are:

- To develop a sensor testing suite which can precisely deliver the desired gas mixture to a sensor. Component gasses need to be to be controlled in a precise manner while variations in sensor response need to be closely monitored and documented.
- The development of a metal oxide gas sensor that can accurately detect the presence and concentration of the analyte gas and is able to measure ongoing changes in concentration in real-time.

This project successfully achieved:

- The design and realization of a full sensor test suite capable of precisely controlling temperature, gas flow rate and analyte concentration.
- The testing of pre-fabricated metal oxide sensors in a trace H_2S environment. Sensor response was monitored and recorded.

- The electrodeposition of a continuous WO_3 thin film.
- Verification that the electrodeposited material is indeed WO_3 via XPS analysis.
- The patterning and release of WO_3 doubly clamped beams.
- Realization of supporting on-chip electrical traces. Conductive inert material was used and wire bonding to off chip circuitry was achieved.
- The electrodeposition of metal nanowires in both porous anodic alumina and track etched polycarbonate templates.
- The release and characterization of metal nanowires.

This project successfully explored a range of potential solutions with regard to the construction of a basic sensor element including nanowire and patterned thin film resistive elements. Metal and metal oxide deposition methods including electrodeposition and sputtering were analyzed. Comprehensive experiments with various physical and chemical based patterning methods were explored.

Future directions

I believe that electrodeposition holds promise in its potential for the creation of gas sensors. The advancement of complementary technologies such as increasingly uniform porous templates could enable the reliable realization of mechanically robust metal oxide structures.

1. Segmented wires for gas sensing will require:
    - The creation of insulating nanowire templates without branching or intersecting pores. The template material would need to be etched by a mild chemical solution which would not affect the metal contact points or metal oxide sensing segments.
    - Analysis of solution surfactants to prevent wire clumping. Surfactant used to enhance wire dispersion should not affect the sensing properties of the wire.

- The development of a process by which segmented wires in solution can be harvested without their destruction.
- The development of a process by which segmented wires can be manipulated in a way that will incorporate them in an electrical circuit.

2. A low stress and mechanically robust tungsten oxide film sensor will require:
   - The development of a uniform layer of metal oxide on the surface of the wafer.
   - The development of a low stress substrate so that released beams do not crack.
3. Both wire and doubly clamped beam technologies will require the development of solutions which exhibit long term stability. This will allow the deposition of metal oxides in a known and predictable manner.

While many of the above points have been thoroughly explored in this thesis, the simultaneous control of all of these necessary components is needed to successfully and reliably produce the investigated sensing structures.

Bibliography

[1] "Honeywell inc.: Gas alert micro 5." Website, 2009. http://www.canarysense.com/p3788/bw_gas_alert_micro_5.php.

[2] G. Eranna, B. C. Joshi, D. P. Runthala, and R. P. Gupta, "Oxide materials for development of integrated gas sensorsa comprehensive review," *Crit. Rev. Solid State*, vol. 29, pp. 111–188, 2004.

[3] E. Comini, G. Faglia, and G. Sberveglieri, *Solid State Gas Sensing*. Springer, 2009.

[4] L. F. Reyes, A. Hoel, S. Saukko, P. Heszler, V. Lantto, and C. Granqvist, "Gas sensors of pure and activated WO_3 nanoparticle films made by advanced reactive gas deposition," *Science*, vol. 117, pp. 128–134, 2006.

[5] A. Kolmakov, Y. Zhang, G. Cheng, and M. Moskovits, "Detection of CO and O_2 using tin oxide nanowire sensors," *Adv. Mater.*, vol. 15, no. 12, pp. 997–1000, 2003.

[6] R. S. Niranjan, K. Vijayamohanan, and S. Mulla, "Effect of copper on the hydrogen sulfide gas sensing properties of the tin oxide thin film," *Proceedings of IEEE Sensors*, vol. 1, pp. 412–417, 2003.

[7] D. C. Meier, C. J. Taylor, R. E. Cavicchi, E. W. V, M. W. Ellzy, K. B. Sumpter, and S. Semancik, "Chemical warfare agent detection using MEMS-compatible microsensor arrays," *IEEE Sensors Journal*, vol. 5, no. 4, pp. 712–725, 2005.

[8] C. Xu, J. Tamaki, N. Miura, and N. Yamazoe, "Grain size effects on gas sensitivity of porous $Sn0_2$-based elements," *Sensors and Actuators B*, vol. 3, pp. 147–155, 1991.

[9] A. Tomchenko, V. Khatko, and I. Emelianov, "WO_3 thick-film gas sensors," *Sensors and Actuators B*, vol. 46, pp. 209 – 215, 1998.

[10] J. Yoo, S. Chatterjee, and E. D. Wachsman, "Sensing properties and selectivities of a $WO_3/YSZ/Pt$ potentiometric NO_x sensor," *Sensors and Actuators B*, vol. 122, p. 644 652, 2007.

[11] B. Frtihberger, M. Grunze, and D. Dwyer, "Surface chemistry of H_2S sensitive tungsten oxide films," *Sensors and Actuator; B*, vol. 31, pp. 167 – 174, 1996.

[12] Y. Zhao, Z.-C. Feng, and Y. Liang, "Pulsed laser deposition of WO_3 base film for NO gas sensor application," *Sensors and Actuators B*, vol. 66, p. 171173, 2000.

[13] T. S. Kim, Y. B. Kim, K. S. Yoo, G. S. Sung, and H. J. Jung, "Sensing characteristics of dc reactive sputtered WO_3 thin films as an NO_x gas sensor," *Sensors and Actuators B*, vol. 62, pp. 102 – 108, 2000.

[14] B. Panchapakesan, D. L. DeVoe, M. R. Widmaier, R. Cavicchi, and S. Semancik, "Nanoparticle engineering and control of tin oxide microstructures for chemical microsensor applications," *Nanotechnology*, vol. 12, p. 336349, 2001.

[15] F. D. Jr., R. E. Cavicchi, S. Semancik, J. S. Suehle, N. H. Tea, J. Small, J. T. Armstrong, and J. T. Kelliher, "In situ conductivity characterization of oxide thin film growth phenomena on microhotplates," *J. Vac. Sci. Technol. A*, vol. 16, no. 1, pp. 131 – 138, 1998.

[16] C. J. Taylor and S. Semancik, "In situ conductivity characterization of oxide thin film growth phenomena on microhotplates," *Chem. Mater.*, vol. 14, pp. 1671 – 1677, 2002.

[17] S. Banerjee, A. Dan, and D. Chakravorty, "Review synthesis of conducting nanowires," *J. Mat. Sci.*, vol. 37, pp. 4261 – 4271, 2002.

[18] B. Deb, S. Desai, G. U. Sumanasekera, and M. K. Sunkara, "Gas sensing behaviour of mat-like networked tungsten oxide nanowire thin films," *Nanotechnology*, vol. 18, p. 285501 (7pp), 2007.

[19] J. Liu, X. Wang, Q. Peng, and Y. Li, "Preparation and gas sensing properties of vanadium oxide nanobelts coated with semiconductor oxides," *Sensors and Actuators B*, vol. 115, pp. 481–487, 2006.

[20] S. Evoy, N. DiLello, V. Deshpande, A. Narayanan, H. Liu, M. Riegelman, B. Martin, B. Hailer, J.-C. Bradley, W. Weiss, T. Mayer, Y. Gogotsi, H. Bau, T. Mallouk, and S. Raman, "Dielectrophoretic assembly and integration of nanowire devices with functional CMOS operating circuitry," *Microelectronic Engineering*, vol. 75, pp. 31 – 42, 2004.

[21] S. Evoy, M. A. Riegelman, N. Naguib, H. Ye, P. Jaroenapibal, D. E. Luzzi, and Y. Gogotsi, "Dielectrophoretic assembly of carbon nanofiber nanoelectromechanical devices," *IEEE Transactions on Nanotechnology*, vol. 4, no. 5, p. 570 575, 2005.

[22] A. Narayanan, Y. Dan, V. Deshpande, N. D. Lello, S. Evoy, and S. Raman, "Dielectrophoretic integration of nanodevices with CMOS VLSI circuitry," *IEEE TRANSACTIONS ON NANOTECHNOLOGY*, vol. 5, no. 2, pp. 101 – 109, 2006.

[23] D.-S. Lee, J.-W. Lim, S.-M. Lee, J.-S. Huh, and D.-D. Lee, "Fabrication and characterization of micro-gas sensor for nitrogen oxides gas detection," *Sensors and Actuators B*, vol. 64, pp. 31–36, 2000.

[24] T. Pauporte, Y. Soldo-Olivier, and R. Faure, "XAS study of amporphous WO_3 formation from a peroxo-tungstate solution," *J. Phys. Chem.*, vol. 149, no. 11, pp. C539–C545, 2003.

[25] P. Obreja, D. Cristea, M. Kusko, and A. Dinescu, "Polymer-based chips for surface plasmon resonance sensors," *J. Opt. A: Pure Appl. Opt.*, vol. 10, p. 064010, 2008.

[26] J. Homola, S. S. Yee, and G. Gauglitz, "Surface plasmon resonance sensors: review," *Sensors and Actuators B*, vol. 54, pp. 3–15, 1999.

[27] A. Kabashin and P. Nikitin, "Surface plasmon resonance interferometer for bio- and chemical-sensors," *Optics Communications*, vol. 150, pp. 5–8, 1998.

[28] A. B. El-Basaty, T. A. El-Brolossy, S. Abdalla, S. Negm, R. A. Abdella, and H. Talaat, "Surface plasmon sensor for NO_2 gas," *Surf. Interface Anal.*, vol. 40, p. 16231626, 2008.

[29] T. Pearce, S. Schiffman, H. Nagle, and J. Gardner, *Handbook of Machine Olfaction - Electronic Nose Technology*. John Wiley and Sons, Inc., third ed., 2003.

[30] M. Manera, J. Spadavecchia, D. Busoc, C. de Julián Fernández, G. Mattei, A. Martucci, P. Mulvaney, J. Pérez-Juste, R. Rella, L. Vasanelli, and P. Mazzoldi, "Optical gas sensing of TiO_2 and TiO_2/Au nanocomposite thin films," *Sensors and Actuators B*, vol. 132, p. 107115, 2008.

[31] M. R. McCurdy, Y. Bakhirkin, G. Wysocki, and F. K. Tittel, "Performance of an exhaled nitric oxide and carbon dioxide sensor using quantum cascade laserbased integrated cavity output spectroscopy," *Journal of Biomedical Optics*, vol. 12, no. 3, pp. 034034 (1–9), 2007.

[32] M. Gharavi and S. G. Buckley, "Single diode laser sensor for wide-range H_2O temperature measurements," *Applied Spectroscopy*, vol. 58, no. 4, pp. 468–473, 2004.

[33] B. Mizaikoff, "Mid-IR fiber-optic sensors," *Analytical Chemistry*, pp. 258A – 267A, 2003.

[34] C.-L. Yao, S.-L. Lee, Y.-J. Hung, Y.-T. Pan, J.-L. Jeng, and H.-C. Wang, "Novel tunable laser sources with 1.5 um and 1.57 um cascaded DFB reflectors for in situ gas monitoring applications," *Sensors and Actuators B*, vol. 140, p. 371377, 2009.

[35] L. S. Rothman, A. Barbe, and D. C. B. et al., "The HITRAN molecular spectroscopic database: edition of 2000 including updates through 2001," *Journal of Quantitative Spectroscopy and Radiative Transfer*, vol. 82, pp. 5–44, 2003.

[36] J. Manne, W. Jger, and J. Tulip, "A quantum cascade laser based room temperature spectrometer for sensitive detection of ammonia and ethylene," *Proc. of SPIE Vol.*, vol. 6900, pp. 690014 (1–8), 2008.

[37] C. Charlton, B. Temelkuran, G. Dellemann, and B. Mizaikoff, "Midinfrared sensors meet nanotechnology: Trace gas sensing with quantum cascade lasers inside photonic band-gap hollow waveguides," *Applied Physics Letters*, vol. 86, p. 194102, 2005.

[38] C. Young, S.-S. Kim, Y. Luzinova, M.Weida, D. Arnone, E. Takeuchi, T. Day, and B. Mizaikoff, "Midinfrared sensors meet nanotechnology: Trace gas sensing with quantum cascade lasers inside photonic band-gap hollow waveguides," *Sensors and Actuators B*, vol. 140, pp. 24–28, 2009.

[39] G. Sauerbrey, "Verwendung von schwingquarzen zur wagung dunner scichten und zur mikrowagung," *Z, Phys.*, vol. 155, pp. 206–222, 1959.

[40] S. Kurosawa, D.-S. Han, J.-W. Park, H. Aizawa, M. Yoshimoto, C. Nakamura, I. J. Miyake, and S.-M. Chang, "Gas sensor using high-frequency quartz crstal microbalance," *IEEE International Frequency Control Symposium and PDA Exhibition*, pp. 462–464, 2001.

[41] H.-H. Tsai, D. H. Wu, T.-L. Chiang, and H. H. Chen, "Robust design of SAW gas sensors by taguchi dynamic method," *Sensors*, vol. 9, pp. 1394–1408, 2009.

[42] A. Sadek, W. Wlodarski, K. Shin, R. Kaner, and K. Kalantar-zadeh, "A polyaniline/WO_3 nanofiber composite-based $ZnO/64^o\ YXLiNbO_3$ SAW hydrogen gas sensor," *Synthetic Metals*, vol. 158, p. 2932, 2008.

[43] R. C. Dorf, *Introduction To Electronic Circuits*. John Wiley and Sons, Inc., second ed., 1993.

[44] P. Oikonomou, K. Manoli, D. Goustouridis, I. Raptis, and M. Sanopoulou, "Polymer/$BaTiO_3$ nanocomposites based chemocapacitive sensors," *Microelectronic Engineering*, vol. 86, p. 12861288, 2009.

[45] S. Shukla and S. Seal, "A novel theoretical model for semiconductor oxide gas sensor," *Mater. Res. Soc. Symp. Proc.*, vol. 828, pp. A4.2.1–A4.2.6, 2005.

[46] J.-W. Gong, Q.-F. Chen, M.-R. Lian, N.-C. Liu, and C. Daoust, "Temperature feedback control for improving the stability of a semiconductormetaloxide (SMO) gas sensor," *IEEE Sensors Journal*, vol. 6, no. 1, 2006.

[47] A. Kolmakov and M. Moskovits, "Chemical sensing and catalysts by one-dimensional metal-oxide nanostructures," *Annu. Rev. Mater. Res.*, vol. 34, pp. 151–180, 2002.

[48] C. Lambert-Mauriat and V. Oison, "Density-functional study of oxygen vacancies in monoclinic tungsten oxide," *J. Phys.: Condens. Matter*, vol. 18, p. 73617371, 2006.

[49] A. R. Hirsch, "Hydrogen sulfide exposure without loss of consciousness: chronic effects in four cases," *Toxicology and Industrial Health*, vol. 18, pp. 51–61, 2002.

[50] W. Morales, M. Cason, O. Aina, N. R. de Tacconi, and K. Rajeshwar, "Combustion synthesis and characterization of nanocrystalline WO_3," *J. Am. Chem. Soc.*, vol. 130, p. 63186319, 2008.

[51] E. A. Meulenkamp, "Mechanism of WO_3 electrodeposition from peroxy-tungstate solution," *J. Electrochem. Soc.*, vol. 144, no. 5, pp. 1664–1671, 1997.

[52] T. Pauporte, "A simplified method for WO_3 electrodeposition," *J. Electrochem. Soc.*, vol. 149, no. 11, pp. C539–C545, 2002.

[53] M. Deepa, A. Srivastava, S. Sharma, Govind, and S. Shivaprasad, "Microstructural and electrochromic properties of tungsten oxide thin films produced by surfactant mediated electrodeposition," *Applied Surface Science*, vol. 254, p. 23422352, 2008.

[54] Z. Yu, X. Jia, J. Du, and J. Zhang, "Electrochromic WO_3 films prepared by a new electrodeposition method," *Solar Energy Materials & Solar Cells*, vol. 64, pp. 55–63, 2000.

[55] W.-C. Hsu, C.-C. Chan, C.-H. Peng, and C.-C. Chang, "Hydrogen sensing characteristics of an electrodeposited WO_3 thin film gasochromic sensor activated by Pt catalyst," *Thin Solid Films*, vol. 516, p. 407411, 2007.

[56] H. Asoh, K. Nishio, M. Nakao, T. Tamamura, and H. Masudaa, "Conditions for fabrication of ideally ordered anodic porous alumina using pretextured al," *Journal of The Electrochemical Society*, vol. 148, no. 4, pp. B152 – B156, 2001.

[57] G. Patermarakis, "Aluminium anodising in low acidity sulphate baths: growth mechanism and nanostructure of porous anodic films," *J Solid State Electrochem*, vol. 10, p. 211222, 2006.

[58] S. Matthias, J. Schilling, K. Nielsch, F. Muller, R. B. Wehrspohn, and U. Gosele, "Monodisperse diameter-modulated gold microwires," *Adv. Mater.*, vol. 14, no. 22, pp. 1618 – 1621, 2002.

[59] F. Muller, A. Birner, J. Schilling, A. P. Li, K. Nielsch, U. Gosele, and V. Lehmann, "High aspect ratio microstructures based on anisotropic porous materials," *Microsystem Technologies*, vol. 8, pp. 7–9, 2002.

[60] S.-H. Baeck, K.-S. Choi, T. F. Jaramillo, G. D. Stucky, and E. W. McFarland, "Enhancement of photocatalytic and electrochromic properties of electrochemically fabricated mesoporous WO_3 thin films," *Adv. Mater.*, vol. 15, pp. 1269–1273, 2003.

[61] S.-H. Baeck, T. F. Jaramillo, G. D. Stucky, and E. W. McFarland, "Synthesis of tungsten oxide on copper surfaces by electroless deposition," *Chem. Mater.*, vol. 15, pp. 3411–3413, 2003.

[62] M. Penza and L. Vasanelli, "SAW NO, gas sensor using $W0_3$ thin-film sensitive coating," *Sensors and Aciuators B*, vol. 41, pp. 31 – 36, 1997.

[63] J. Chen, D. Lu, W. Zhang, F. Xie, J. Zhou, L. Gong, X. Liu, S. Deng, and N. Xu, "Synthesis and raman spectroscopic study of $W_{20}O_{58}$ nanowires," *J. Phys. D: Appl. Phys.*, vol. 41, p. 115305 (6pp), 2008.

[64] S. A. Campbell, *The Science and Engineering of Micromechanical Fabrication*. Oxford University Press, second ed., 2001.

[65] P. Walker and W. H. Tarn, *CRC Handbook of Metal Etchants*. CRC Press, 1990.

[66] K. R. Williams, K. Gupta, and M. Wasilik, "Etch rates for micromachining processing - part II," *JMEMS*, vol. 12, no. 6, pp. 761–778, 2003.

[67] R. Legtenber, H. A. Tilmans, J. Elders, and M. Elwenspoek, "Stiction of surface micromachined structures after rinsing and drying: model and investigation of adhesion mechanisms," *Sensors and Actuators A*, vol. 43, pp. 230 – 238, 1994.

[68] D. T. Haluzan, D. M. Klymyshyn, M. Borner, S. Achenbach, G. Wells, T. Mappes, and J. Mohr, "Stiction issues and actuation of RF LIGA-MEMS variable capacitors," *Microsyst Technol*, vol. 14, p. 17091714, 2008.

[69] S. Enders, H. Kahl, and J. Winkelmann, "Surface tension of the ternary system water + acetone + toluene," *J. Chem. Eng. Data*, vol. 52, pp. 1072–1079, 2007.

[70] G. Vhquez, E. Alvarez, and J. M. Navaza, "Surface tension of alcohol + water from 20 to 50 C," *J. Chem. Eng. Data*, vol. 40, pp. 611 – 614, 1995.

[71] B. A. Grigoryev, B. V. Nemzer, D. S. Kurumov, and J. V. Sengers, "Surface tension of normal pentane, hexane, heptane, and octane," *International Journal of Thermophysics*, vol. 13, no. 3, pp. 453 – 464, 1992.

[72] C. H. Mastrangelo, "Suppression of stiction in MEMS," *Mat. Res. Soc. Symp. Proc.*, vol. 605, pp. 105–116, 2000.

[73] M. G. el Hak, *The MEMS Handbook: MEMS, design and fabrication*. CRC Press, third ed., 2006.

[74] M. Ohring, *Materials science of Thin Films: Deposition and Structure*. Academic Press, second ed., 2002.

[75] D. Hoffman, "Perspectives on stress in magnetron-sputtered thin films," *J. Vac. Sci. Technol.*, vol. 12, no. 4, pp. 953–961, 1994.

[76] C. Rout, K. Ganesh, A. Govindaraj, and C. N. R. Rao, "Sensors for the nitrogen oxides, NO_2, NO and N_2O, based on In_2O_3 and WO_3 nanowires," *Appl. Phys. A*, vol. 85, pp. 241–246, 2006.

[77] *Canadian Centre for Occupational Health and Safety Act*. Canadian Centre for Occupational Health and Safety Act. 1977-78, c. 29, s. 1.

[78] *Material Safety Data Sheet: Hydrogen Suphide*. Sigma-Aldrich.

[79] T. Kurvits and T. Marta, "Agricultural NH_3 and NO_x emissions in canada," *Environmental Pollution*, vol. 102, pp. 187–194, 1998.

[80] E. Nordling, N. Berglind, and E. M. et al., "Traffic-related air pollution and childhood respiratory symptoms, function and allergies," *Epidemiology*, vol. 19, no. 3, pp. 401 – 408, 2008.

[81] A. Lindgren, E. Stroh, P. Montnmery, U. Nihln, K. Jakobsson, and A. Axmon, "Traffic-related air pollution associated with prevalence of asthma and COPD/chronic bronchitis. a cross-sectional study in southern sweden," *International Journal of Health Geographics*, vol. 8, no. 2, 2009.

[82] M. Deepa, A. Srivastava, and S. Agnihotry, "Influence of annealing on electrochromic performance of template assisted, electrochemically grown, nanostructured assembly of tungsten oxide," *Acta Materialia*, vol. 54, p. 45834595, 2006.

[83] D. Dini and F. Decker, "Stress in thin films of metal oxide electrodes for intercalation reactions," *Electrochimica Acta*, vol. 43, no. 19-20, pp. 2919–1923, 1998.

[84] M. Hepel, H. Redmonda, and I. Dela, "Electrochromic WO_3-x films with reduced lattice deformation stress and fast response time," *Electrochimica Acta*, vol. 52, p. 35413549, 2007.

[85] Y. Krasnov, S. Volkov, and G. Kolbasov, "Optical and kinetic properties of cathodically deposited amorphous tungsten oxide films," *Journal of Non-Crystalline Solids*, vol. 352, pp. 3995 – 4002, 2006.

[86] J. F. Watts and J. Wolstenholme, *An Introduction to Surface Analysis By XPS and AES*. Wiley, 2003.

[87] M. Prutton and M. m. El Gomati, *Scanning Auger Electron Spectroscopy*. Wiley, 2006.

[88] D. M. Hercules, "Quantitative surface characterization using X-ray photoelectron spectroscopy," *Fresenius J Anal Chem*, vol. 355, pp. 209 – 215, 1996.

[89] E. Gillet, K. Masek, D. Lollman, and M. Gillet, "Evolution of the oxidation states at the WO_3 thin film surface during annealing in gases," *Vacuum*, vol. 82, pp. 261–265, 2008.

[90] *NIST X-ray Photoelectron Spectroscopy Database*.

[91] M. Penza, M. Tagliente, L. Mirenghi, C. Gerardi, C. Martucci, and G. Cassano, "Tungsten trioxide (WO3) sputtered thin films for a NOx gas sensor," *Sens. and Act. B*, vol. 50, pp. 9 – 18, 1998.

[92] A. G. Dirks, R. A. M. Wolters, and A. E. M. D. Veirman, "Columnar microstructures in magnetron-sputtered refractory metal thin films of tungsten, molybdenum and $W - Ti - (N)$," *Thin Solid Films*, vol. 208, pp. 181–188, 1995.

[93] D. B. Bergstrom, F. Tian, I. Petrov, J. M. J. E., and Greene, "Origin of compositional variations in sputter-deposited Ti_xW_{12x} diffusion barrier layers," *Appl. Phys. Lett.*, vol. 67, no. 21, pp. 3102–3104, 1995.

[94] D. Al-Mawlawi, C. Z. Liu, and M. Moskovits, "Nanowires formed in anodic oxide nanotemplates," *J. Mater. Res.*, vol. 9, no. 4, pp. 1014–1018, 1993.

[95] K. Nielsch, F. Muller, A.-P. Li, , and U. Gsele, "Uniform nickel deposition into ordered alumina pores by pulsed electrodeposition," *Adv. Mater.*, vol. 12, no. 8, pp. 582–586, 2000.

[96] L. Su, L. Zhang, J. Fang, M. Xu, and Z. Lu, "Electrochromic and photoelectrochemical behav-iour of electrodeposited tungsten trioxide films," *Sol. Energ. Mater. & Sol. Cells.*, vol. 58, pp. 133–140, 1999.

[97] S. Wang, X. Feng, J. Yao, and L. Jiang, "Controlling wettability and photochromism in a dual-responsive tungsten trioxide film," *Angew. Chem.*, vol. 118, pp. 1286–1289, 2006.